The Development of Ultra-High Temperature Experimental Capabilities for the Electrolytic Extraction of Titanium from New Zealand Steel's Iron Slag

Thomas George Hughes

A thesis presented for the degree of

Master of Engineering

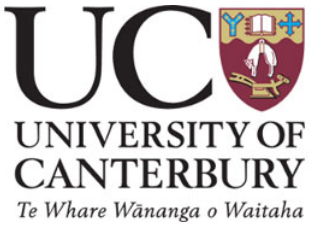

Department of Chemical and Process Engineering

University of Canterbury

New Zealand

10th December 2018

The Development of Ultra-High Temperature Experimental Capabilities for the Electrolytic Extraction of Titanium from New Zealand Steel's Iron Slag

Thomas George Hughes

Abstract

While titanium exhibits excellent mechanical and corrosion resistant properties, its high price severely limits its applications. The inefficiency of the Kroll process, the predominant production method for titanium, has contributed to titanium's high price. There is ongoing research dedicated to the development of a more efficient/cost effective method of titanium production. The most significant development is the Fray, Farthing, Chen (FFC) Cambridge process which demonstrated that high-purity titanium can be extracted directly from its oxide through an electrolytic process, without the need of a metallothermic reduction step. For this research, it was hypothesised that titanium could be electrolytically extracted from New Zealand Steel iron slag as it is rich in TiO_2 (34 wt.%), and the composition of the slag indicates it could form a viable electrolyte. This would transform a low value secondary product, currently used as roadfill aggregate, to a prized material.

This research forms the basis of a larger project as it focuses on the development of ultra-high temperature experimental capabilities for electrolysis experiments and in the performance of preliminary electrolysis experiments to guide future research.

Overall, a support structure was designed and produced for a MTI GSL-1700X-100VT-UL vertical tube furnace to allow for ultra-high temperature electrolysis experiments. The thermal profile of the furnace was examined through direct experiments and software modelling to ensure the long-term usage of the furnace. Preliminary electrolysis experiments showed a layered structure of partially reduced Ti/Si directly on the cathode and pockets of partially reduced Ti/Si in the surrounding electrolyte. The electrolytic process had a low current efficiency of 1.1% which was theorised to be due to the electrolytes high electrical conductivity.

Dedication

This thesis is dedicated to my grandfather, Philip Eric Cross

1929-2018

Acknowledgements

I would like to thank the following people for their help and support.

- The Ministry of Business, Employment, and Innovation (MBIE) for providing the funding for this research (grant # UOCX1605).
- My supervisory team: Dr. Matthew Watson, Dr. Aaron Marshall, and Dr. Catherine Bishop for their advice, guidance, and patience throughout this research.
- Dr. Ian Brown and Dr. Yaodong Jia, from Callaghan Innovation, for their technical support and guidance.
- Fellow postgraduate students Samuel Martin Treceño and Nic Weaver for their assistance in the SEM analysis, technical support, and their comradery. I wish you both the best of luck with your studies and with what awaits afterwards.
- The technical staff of the chemical and process engineering (CAPE) department who offered their technical expertise, wisdom, and produced the various parts of the experimental rig. Namely: Leigh Richardson, Frank Weerts, Stephen Buezenburg, Graham Furniss, and Stephen Hood. Special thanks goes to Graham Mitchell who masterfully fabricated the majority of the parts.

- Rob Spiers and Matt Cockcroft for helping cross-section the slag samples and general advice on handling slag samples.
- My extended and immediate family members: Simon, Janice, William, and Rosie Hughes for their support.
- To all of my friends who provided their support and specifically Ben Mitchell, Liam Oldersaw, and Stephen Loyd who provided an outsider perspective during the review process.

Contents

List of Figures

List of Tables

List of Acronyms

NZS New Zealand Steel

FFC Fray, Farthing, and Chen

OS Ono and Suzuki

AC Alternating Current

EIS Electrochemical Impedance Spectroscopy

CAPE Chemical And Process Engineering

YSZ Yittria Stabilised Zerconia

SEM Scanning Electron Microscope

EDS Energy Dispersive x-ray Spectroscopy

BED-C Back-scatter Electron Detection

Chapter 1

Introduction

1.1 Background

Titanium is a highly valued metal, prized for its physical properties, such as its high strength-to-weight ratio. Its name is derived from the titans: Greek mythological beings with super-human strength [1]. Titanium is the ninth most common element [2] found in the Earth's crust and exists naturally in various oxide states. The metallic form of titanium, and its alloys, exhibit excellent mechanical and corrosion resistant properties [3]. Titanium commands a high market price of 56 USD/kg [4] which is 7000% more expensive than carbon steel (0.8 USD/kg [5]). This high cost restricts its use to applications where cost is subservient to performance such as aerospace, military, bio-medical, and high performance sports products [6][7].

Titanium's high market price is due to its expensive production and purification process. The primary industrial production method for titanium is the Kroll process which, as of 1993, accounts for 80% of global titanium production [8]. The Kroll process is a slow, batch process which results in high operating costs. Prior research has been dedicated to alternative methods of production in the hope of reducing the cost of production. For instance, the Armstrong process is a development on existing techniques to make a cheaper, continuous process [9]. The FFC Cambridge process demonstrated the viability of an electrolytic extraction method when they successfully produced titanium from titanium dioxide through electrochemical reduction.

New Zealand Steel (NZS) utilises ironsand as a feedstock to produce iron which is further processed to make steel. Ironsand contains significant quantities of TiO_2, approximately 7wt.% [10], which is not utilised in the process and as such is concentrated in the iron slag to 33wt.%, as shown in Table 1.1. Currently, the iron slag is not processed any further. It is treated as a secondary product and is used as an aggregate to make inexpensive roadfill [11].

Table 1.1: Chemical composition of NZS iron slag and ironsand as determined by x-ray fluorescence (XRF) analysis [10].

Compounds	NZS iron slag (wt.%)	Iron sand (wt.%)
TiO_2	32.52	7.13
Al_2O_3	18.50	3.54
CaO	16.36	0.49
SiO_2	13.79	1.90
MgO	13.56	2.66
Fe_2O_3	4.29	85.21
MnO	0.90	0.51
Na_2O	0.42	0.15
K_2O	0.15	0.04
P_2O_5	0.02	0.08

With the developments made in electrolytic extraction by the FFC Cambridge process, it was hypothesised that the TiO_2 present in the NZS iron slag could be reduced to form high-purity titanium through an electrolysis process. Electrolysis is an attractive alternative to traditional metal production methods because it can in theory reduce material with just electricity and evolves only oxygen, if coupled with an inert anode. Molten oxide systems have the potential to be suitable electrolytes, an important component of an electrolysis process. This is due to their thermal stability, high reduction potentials, and good mass transport properties [12]. Hence, the NZS iron slag, which is composed of various metal oxides as shown in Table 1.1, could act as a suitable electrolyte.

1.1.1 Objectives

Research into this area has potentially significant economic implications for New Zealand businesses and as such, a grant (UOCX1605) was awarded from the Ministry of Business, Innovation, and Employment. The grant established two research aims for the project along with the critical steps needed in order to achieve these aims:

- Understand critical properties to develop the ultra-high-temperature electrolytic process.
  - Measurement of critical slag properties and variability.
  - Selection of thermodynamic modelling software.
  - Prediction of slag and electrolyte critical properties.
- Electrolytic production of titanium from waste slag material.
  - Determine the influence of electrolysis conditions on titanium production.
  - Development of an ultra-high-temperature reference electrode.
  - Characterisation of deposited metal product at the cathode.

The overall goal of this research was to determine if the electrolytic extraction of titanium from NZS iron slag is feasible. A critical aspect of this, and a focus of this thesis, is the development of an ultra-high temperature experimental rig capable of performing electrolytic experiments.

Chapter 2

Literature Review and Theoretical Background

To broaden the understanding of titanium extraction processes and therefore the challenges associated with them, a literature review was performed. This review examined the various industrial and research production methods for titanium along with the research preformed into high temperature electrolysis processes. As an electrolysis process is the focus of this project, fundamental aspects of electrolysis and the role of the electrolyte were studied. Lastly from a practical standpoint, high-temperature furnaces, and the governing phenomena, were examined.

2.1 Titanium Production Methods

2.1.1 Hunter Process

The Hunter process was developed by Mathew A. Hunter in 1910 [13] and it involves the conversion of $TiCl_4$ to Ti with the use of sodium as a reducing agent, as shown in equation 2.1b. Sodium metal is added to a retort and heated to 900°C. $TiCl_4$ is then added which was prepared by the chlorination of TiO_2, as stated by equation 2.1a.

$$TiO_2 + 2C + 2Cl_2 \longrightarrow TiCl_4 + 2CO \tag{2.1a}$$

$$TiCl_4 + 4Na \longrightarrow Ti + 4NaCl \tag{2.1b}$$

Once the reaction has taken place, the mixture is cooled and the NaCl-Ti mixture is removed from its container by chipping the material out. The remaining NaCl is leached out by washing the titanium chips with HCl, leaving titanium. The process is inefficient due to the large requirement of sodium which cannot be reused between batches. Furthermore, it needs large volume containers, is time consuming, and labour intensive. The Hunter process was succeeded by the Kroll process. According to a report written in 2001 [14], there is only one factory still using the Hunter process.

2.1.2 Kroll Process

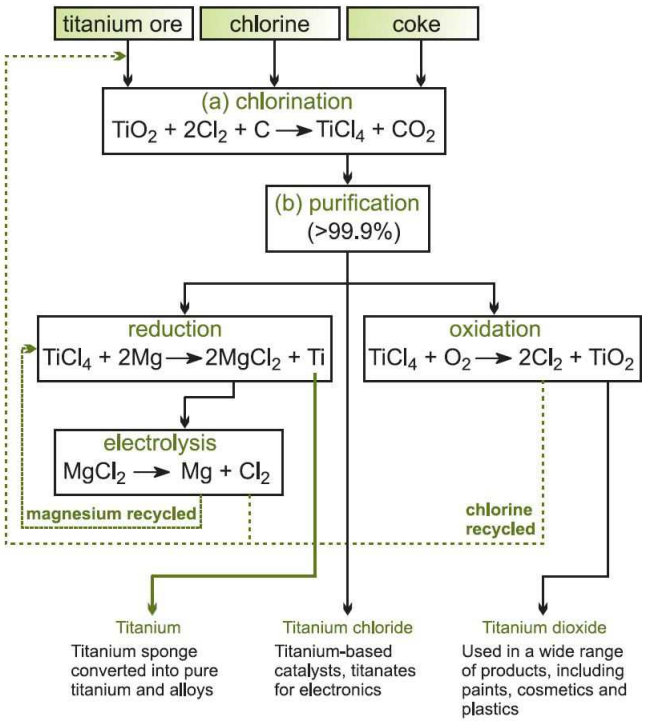

Figure 2.1: Process diagram for the production of titanium via the Kroll process. Obtained from: [15].

The Kroll process was patented in 1940 by William Kroll [16] and is the primary industrial method by which titanium is produced to this day. The process involves the reduction of $TiCl_4$ to Ti with the use of magnesium in a batch-like process. The reaction mechanism is described in equations 2.2a - 2.2c.

$$TiO_2 + C + 2Cl_2 \longrightarrow TiCl_4 + CO_2 \tag{2.2a}$$

$$TiCl_4 + 2Mg \longrightarrow Ti + 2MgCl_2 \tag{2.2b}$$

$$MgCl_2 \longrightarrow Mg + Cl_2 \tag{2.2c}$$

The magnesium is heated to 800-900°C in an argon-rich environment to prevent oxidation. $TiCl_4$ is added to the mixture and heated to 1000°C in order to speed up a relatively slow reaction [17]. On an industrial scale, the process spans over several days. During this process, the $MgCl_2$ is removed several times by tapping it off. After the reaction has ceased the retort is opened and the solid material is chipped out. The titanium is in a sponge-like configuration and has residual $MgCl_2$ and Mg which is removed by vacuum distillation [18].

The Kroll process is a modification of the Hunter process, using magnesium as opposed to sodium as the reducing agent. The reason for the change in material is the recovery of the reactants. The Hunter process produces NaCl which is difficult to process back to sodium metal but the Kroll process produces $MgCl_2$ which can be processed back to a metal form via electrolysis [15].

Another key advantage the Kroll process has over the Hunter process is the size of the containers. In the Hunter process, for every 1 mol of titanium produced, 4 mol of NaCl is also produced. This equates to 10.2cm^3 of NaCl for every 1 cm^3 of titanium. The Kroll process by comparison only needs 2 mol of Mg per mol of titanium, which is 2.65 cm^3 for every 1 cm^3 of titanium. This allows the Kroll process to use smaller retorts which is more energy efficient. While the Kroll process is the dominant form of titanium production, it is not ideal as it is energy intensive, slow, and requires reactants which are toxic to individuals and the environment [17].

2.1.3 Armstrong Process

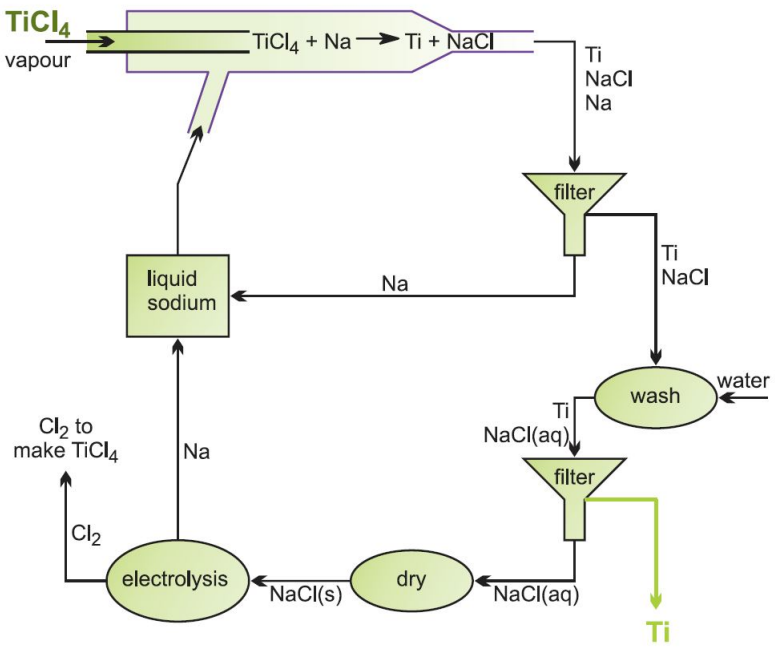

Figure 2.2: Process diagram for the production of titanium via the Armstrong process. Obtained from: [15].

The Armstrong process is a modification of the Hunter process as it follows the same reaction scheme but operates in a continuous manner, as opposed to a batch reaction. By operating in a continuous manner, the setup and shutdown time of the process is minimised thus reducing the amount of labour required. $TiCl_4$ vapour is injected into a stream of molten sodium which has a higher than required stoichiometric ratio to reduce the $TiCl_4$ into Ti [17]. The main issue with this approach is that the oxygen content of the titanium is unacceptable for some titanium applications [19]. The Armstrong process was developed by Cristal US Inc./International Titanium Powder Inc. [20] and a pilot plant was opened in 2006 [21].

2.1.4 FFC Cambridge Process

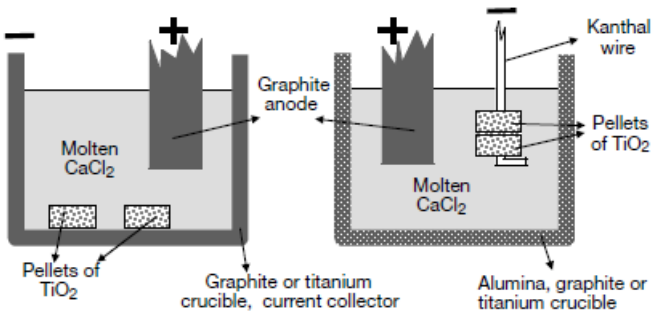

Figure 2.3: A schematic of the FFC Cambridge process. Obtained from: [22].

The FFC Cambridge process was developed in 2000 [22] and represented a breakthrough, proving that high-purity titanium can be produced through electrochemical means. TiO_2 powder is sintered together and acts as a cathode in a $CaCl_2$ electrolyte with a carbon anode. The material is heated to 950°C and a potential of 2.8-3.1 V is applied [22]. The TiO_2 cathode is reduced to Ti and the liberated oxygen travels through the electrolyte and reacts with the anode to produce CO/CO_2 which is shown in equations 2.3a to 2.3c. The operating potential is set below the reduction potential of $CaCl_2$ which allows for the direct reduction of TiO_2 without the consumption of the electrolyte. From an environmental perspective this is an improvement from the Kroll/Hunter processes which require vast amounts of chlorine. The process is currently being developed for commercial production by Metalysis [23]. So far, they have been able to scale up the process to the tonne scale.

$$Cathode : TiO_2 + 4e^- \longrightarrow Ti + {O_2}^{2-} \tag{2.3a}$$

$$Anode : C + {O_2}^{-2} \longrightarrow CO_2 + 4e^- \tag{2.3b}$$

$$Overall : TiO_2 + C \longrightarrow Ti + CO_2 \tag{2.3c}$$

However, this process is not without its issues. The diffusion of the oxygen out of the solid TiO_2/cathode is likely to be rate-limiting [22]. The researchers highlighted several factors which need to be addressed in order to improve its viability for large scale production [24]. The reported current efficiency for the lab-scale process is 50% which is not viable for commercial applications. Commercial electrolysis processes aim for a high current efficiency in order to reduce energy costs. For example, the Hall-Héroult process (aluminium's production method) has a current efficiency between 85 and 95% [25].

While the FFC Cambridge process does not produce as much pollution as the Kroll process, it is still producing CO/CO_2 due to the use of a carbon anode. Inert, commercially viable electrodes need to be developed in order to reduce the pollutants produced. There are also concerns that the produced metal will rapidly oxidise when removed from the reactor due to its porous nature. Lastly the sintering of the TiO_2 powder to form the cathode is a time consuming process, requiring a 1000°C environment which affects the economic viability of the process.

2.1.5 Ono and Suzuki Process

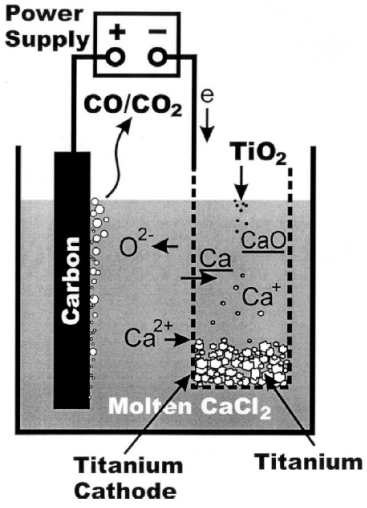

Figure 2.4: Reaction scheme of the OS process. Obtained from: [26].

The Ono and Suzuki (OS) process was developed in 2003 [26] and is a modification of the FFC Cambridge process. Instead of electrolysing TiO_2 directly, the process relies on dissolved calcium in the electrolyte to reduce the TiO_2 to Ti. The applied voltage will then regenerate the oxidised CaO back to Ca and produce CO_2 at the carbon anode as shown in equation 2.4b and 2.4c. As the reduction of TiO_2 does not occur at the titanium cathode, the material can be in powder form which allows for better O_2 transfer properties as it has more diffusion pathways [9]. The applied voltage is set such that it is sufficient to reduce the produced CaO but low enough not to effect the $CaCl_2$ which is acting as the electrolyte.

$$TiO_2 + 2Ca \longrightarrow Ti + 2O^{2-} + 2Ca^{2+} \tag{2.4a}$$

$$Ca^{2+} + 2e^- \longrightarrow Ca \tag{2.4b}$$

$$C + xO^{2-} \longrightarrow CO_x + 2xe^- \tag{2.4c}$$

2.2 Electrolysis

2.2.1 Fundamentals

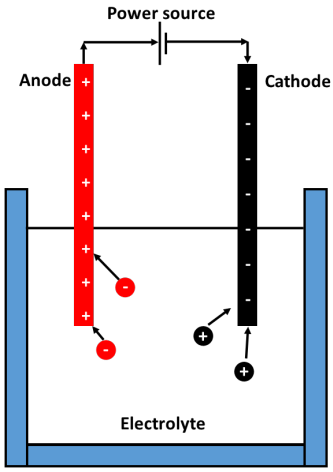

Figure 2.5: Two-electrode configuration for an electrochemical cell.

An electrolytic process is comprised of a reduction/oxidation reaction pair which occurs spontaneously due to the application of an external potential difference. The most basic electrochemical cell is comprised of two electrodes (anode and cathode), an electrolyte, and an applied potential. The oxidation and reduction reactions occur at the positively charged anode and negatively charged cathode, respectively. A typical reaction scheme for a metal oxide (MO_2) is shown in equations 2.5a to 2.5c. The electrodes are partially submerged in a conducting medium which facilitates the transfer of charge and material, known as the electrolyte. Figure 2.5 graphically shows a two-electrode configuration.

$$Overall : MO_2 \longrightarrow M + O_2 \tag{2.5a}$$

$$Cathode : M^{+4} + 4e^- \longrightarrow M \tag{2.5b}$$

$$Anode : {O_2}^{-2} \longrightarrow O_2 + 4e^- \tag{2.5c}$$

The most widely known industrial electrolytic process is the Hall-Héroult process, used in the industrial production of aluminium. Al_2O_3 is dissolved in a Na_3AlF_6 electrolyte and electrolysed to form Al and CO_2, as carbon is used as the electrode material. The adoption of the Hall-Héroult process has made aluminium a widely available, cheap material. Before its use, aluminium was comparable in price to silver [27].

2.2.2 Applied Potential

The potential at which the reaction occurs is determined by the difference between the reduction and oxidation reactions, as stated in equation 2.6.

$$E_{\text{cell}} = E_{\text{red}} - E_{\text{ox}} \tag{2.6}$$

The individual reactions, known as the half cell reactions, are shown in equations 2.7a and 2.7b.

$$Ti^{+4} + 4e^- \rightleftharpoons Ti \qquad E_{\text{red}}(@1626°C) = -1.51V \tag{2.7a}$$

$$C + {O_2}^{-2} \rightleftharpoons CO_2 + 4e^- \qquad E_{\text{ox}}(@1626°C) = -1.03V \tag{2.7b}$$

$$TiO_2 + C \rightleftharpoons Ti + CO_2 \qquad E_{\text{cell}}(@1626°C) = -0.48V \tag{2.7c}$$

The theoretical half cell reaction potentials are governed by the Nernst equation, which is influenced by the temperature and the chemical activities of the constituent compounds. This is shown in equation 2.8.

$$E = E^o - \frac{RT}{nF} ln \frac{a_{\text{Red}}}{a_{\text{Ox}}} \tag{2.8}$$

Where R is the universal gas constant ($JK^{-1}mol^{-1}$), T is the temperature (K), n is the number of electrons transferred in the reaction, F is Faraday's constant ($Cmol^{-1}$), a_{Red} is the activity of the reduced compounds, a_{Ox} is the activity of the oxidised compounds, E is the potential (V), and E^o is the standard potential (V).

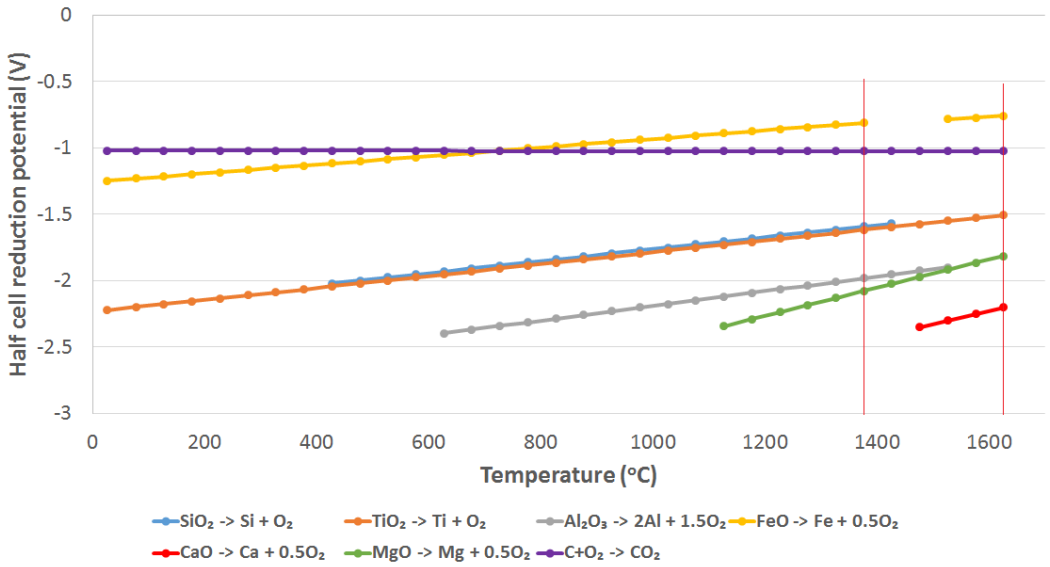

Figure 2.6: The half cell reduction potentials of key, pure metal oxides across a range of temperatures [28]. The red vertical lines highlight the potentials at specific temperatures referenced in the text.

An approximate reduction potential can be determined by calculating the reduction potential of pure oxide systems. Figure 2.6 shows half cell reduction potentials for pure metal oxides over a range of temperatures [28]. These potentials were used in equation 2.7 and the full calculations are shown in Appendices F. The graph shows that the half cell reduction potentials of FeO, SiO_2, and TiO_2 are -0.81V, -1.59V, -1.61V respectively when at 1375°C. This indicates that in order to provide a potential to reduce TiO_2, SiO_2 and FeO will also be reduced. The reduction potentials of the actual system may differ since they are in a solution and not as individual oxide systems.

Often a potential greater than the theoretical value is applied to the system to overcome various impeding factors. The difference between the applied ($E_{applied}$) and theoretical (E_{theory}) potential is referred to as the over-potential. The three main types of over-potentials are activation, concentration, and resistance, as summarised in equation 2.9. Activation over-potential ($\eta_{\text{activation}}$) is due to the activation energy of the reaction which must be overcome in order for a reasonable reaction rate. Concentration over-potential ($\eta_{\text{concentration}}$) is due to the concentration changes around the electrode. As the process continues, electrical migration of ions is relatively reduced and the surrounding material is depleted. This over-potential can be mitigated by mixing the electrolyte during electrolysis [29]. Resistance over-potential (IR) is due to the resistive energy losses across the electrode configuration.

$$E_{\text{applied}} = E_{\text{theory}} + \eta_{\text{activation}} + \eta_{\text{concentration}} + IR \tag{2.9}$$

Experimentally the reduction potentials of faradaic reactions can be determined through linear sweep or cyclic voltammetry. In both methods, the voltage is varied between two potentials at a fixed rate and the current response is recorded, as shown in Figure 2.7. A current peak or trough is indicative of a faradaic reaction as electrons are diverted to, or generated from, that reaction [30]. The magnitude of the current peak/trough is influenced by the potential scan rate, as explained below. As the potential is increased, the faradaic reaction rate increases until the transport of reactants to the electrode becomes the limiting factor. Higher scan rates result in a greater current peak/trough as higher reaction rates are reached before the reactants in the immediate area are depleted [30]. This identification method is best used in conjunction with theoretical deposition voltages and ideally should be used for simple systems. Systems that have materials which deposit at a similar potential may be difficult to detect if the peaks overlap.

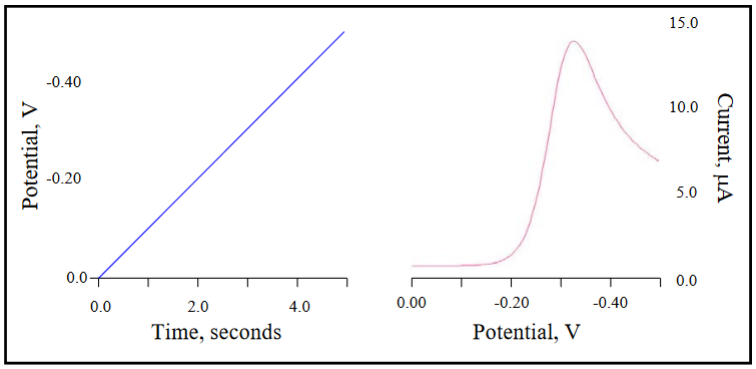

Figure 2.7: An example of linear sweep voltammetry and the current response showing a faradaic reaction. Obtained from: [31].

Cyclic voltammetry is similar to linear sweep voltammetry and involves sweeping the voltage multiple times in a cyclic pattern. The scan rate can be used to identify if the process is reversible, irreversible or quazi-reversible. If the process is reversible, varying the scan rate should not alter the reduction potential.

2.2.3 Reference Electrodes

Reference electrodes are used in most setups to allow for the monitoring of the potentials between the reference and the cathode/anode. An electrochemical cell with a cathode, anode, and reference electrode is referred to as a three-electrode system. Reference electrodes act as a neutral comparison point. As it is being used as a comparison point its potential needs to be known, should be stable, and reproducible across multiple experiments. Standard reference electrodes produce a stable potential by having a chemical equilibrium between the solid electrode and the solution. The chemical equilibrium, and therefore the potential, varies with temperature which requires the temperature of the system to be known.

The most common reference electrode is the Ag/AgCl electrode which is a silver wire covered in silver chloride [32]. When standard reference electrodes cannot be used due to temperature constraints, pseudo-reference electrodes are used. Pseudo-reference electrodes are generally pure metals with high melting points. Pure materials lack a chemical equilibrium and therefore do not have a known potential [33]. This means that the potential will drift over the course of an experiment. However, Inzelt [33] has commented that the potentials measured by pseudo-reference electrodes can be constant depending on the specific system. Graphite [34], titanium [22] and platinum [35] are examples of pseudo-reference electrodes used in high temperature processes.

2.2.4 Research in High Temperature Electrolytic Processes

In the interest of clean production methods, there has been a significant amount of research into applying an electrolytic process for the production of iron [36][37][38]. The current production method for iron relies on the carbothermic reduction of iron oxide and it is estimated that this produces 2.1 billion tonnes of CO_2 on an annual basis [39]. A significant issue in the electrolysis of iron oxide, which is being addressed, is the selection of an inert anode suitable for evolving only oxygen [37][38].

An oxygen-evolving anode must be able to withstand high operating temperatures; be chemically stable when in a corrosive molten oxide electrolyte; and not be consumed during the process by acting as a reducing compound. In order to be usable for industrial applications, the anode must be able to maintain high current densities ($>1 Acm^{-2}$) [37]. Iridium was shown to be a viable oxygen-evolving anode material but only in electrolytes with a low optical basicity (<0.6). A basic electrolyte resulted in the corrosion of the electrode [37]. The concept of optical basicity is explored in Appendices G, but it can be summarised as the Lewis acid-base theory for molten

oxide system where a low optical basicity represents an acidic system. While an important discovery, it has limited applications due to the high cost of iridium. The reduction of iron oxide from lunar regolith to produce breathable oxygen for extra-terrestrial exploration is one of the studied applications [40]. The research into this application showed that a $Ir_{50}W_{50}$ alloy was viable as an inert oxygen-evolving anode material but pure iridium performed better in terms of durability and current efficiency.

A significant development occurred when chromium alloys ($Cr_{90}Fe_{10}$) were shown to be a viable oxygen evolving anode material for the electrolysis of iron oxide. The anode exhibited limited consumption during electrolysis which was due to the anodes interaction with the electrolyte (wt.%: 42.3% CaO, 42.3% Al_2O_3, 5.4% MgO, 10% Fe_3O_4)[38]. The anode reacted to form chromium and aluminium oxides in its internal structure which prevented erosion. This research has wide spread implications as the low cost of chromium alloys allows for a greater number of viable applications.

Molten sulfides have been investigated as an alternative to molten oxide systems. The electrolytic extraction of copper from a BaS-Cu_2S system was attempted and it showed the successful deposition of Cu at an operating temperature of 1105°C [34]. According to Sokhanvaran et al. [34], the 57 wt.% BaS, 43 wt.% Cu_2S electrolyte showed partial ionic conductivity with a minimum of 28% of the total charge being transported by ions. It was concluded that knowledge of conductivity of the electrolyte and its relation to the faradaic efficiency would be needed to optimise the process. The general principle was investigated further and showed that molybdenum, copper, and rhenium could be extracted from a $(BaS)_{54}$-$(Cu_2S)_{31}(La_2S_3)_{15}$ electrolyte at 1226°C [41].

Recent research by Yan [42] was carried out to determine if it was possible to reduce titanium oxide to titanium with the use of a Na_3AlF_6 electrolyte. This is the same electrolyte used in the Hall-Héroult process. The system operated at a temperature of 1050°C. The conclusions to this research was that an electrolyte containing 92-96 wt.% Na_3AlF_6 and 4-8 wt.% TiO_2 only allowed for the partial reduction of titanium due to back-oxidation reactions with oxygen. Aluminium was added to the electrolyte so that the aluminium would bind with the titanium, preventing it from re-oxidising. This was successful as titanium-aluminium alloys were found.

2.3 Electrolyte

An electrolyte is defined as a solution which dissociates into charged ions used to support an electrolysis process. Traditional applications are based in aqueous solutions but for this study the use of molten oxides is explored. An ideal electrolyte should have the following properties [12].

- The reduction potential of the electrolyte material must be higher than the target compound to prevent electrolyte reduction during electrolysis.
- Support the movement of charged particles (i.e. be ionically conductive).
- Allow for the reactants to dissolve into the electrolyte to promote mass transfer.
- Form a eutectic with the reactant to reduce the operating temperature as much as possible.
- Be chemically neutral with respect to the container and electrodes.

The structure of molten oxide systems and the conductivity of the electrolyte are discussed in greater detail in following sections.

2.3.1 Network Structure

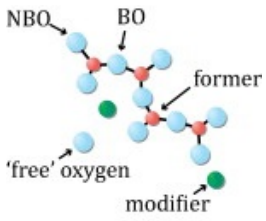

Figure 2.8: A simplified representation of the atomic structure of a silicon network and the various component parts of the structure. Obtained from: [43].

NZS iron slag contains large quantities of metal oxides such as TiO_2 (32%), Al_2O_3 (20%), SiO_2 (17%), MgO (17%), and CaO (9%). Compounds such as SiO_2 exist in a large network configuration which contributes to its stability and high melting point. In a pure SiO_2 system each individual monomer associates with another three SiO_2 compounds, and the pattern continues indefinitely. The oxygen atoms which associate with the other monomer are referred to as bridging oxygen (BO), as illustrated in Figure 2.8. The outer-most oxygen atoms which have not yet bonded with another monomer are called non-bridging oxygen (NBO). This structure can be disturbed by the introduction of compounds which break the network. Network breaking cations, such as Ca^{2+}, Mg^{2+}, bond with the non-bridging oxygen preventing the network from continuing [43]. Amphoteric cations such as Al^{3+} [44] or Ti^{4+} [45][46] can act as network breakers or formers depending on the solution. The structure and physical properties of a molten oxide electrolyte is then dependent on the level of polymerisation. The extent of polymerisation (Q) can be quantified by the ratio of non-bridging oxygen (NBO) to the number of tetragonal ions (T) [44]. This is shown in equation 2.10.

$$Q = \frac{NBO}{T} \tag{2.10}$$

2.3.2 Ionic Conductivity

When discussing the conductivity of an electrolyte, the ionic and electronic conductivity must be considered. Most molten oxides exhibit both forms of conductivity and therefore are referred to as mixed conductors [47]. Electronic conductivity is defined as the ability for the material to allow for the flow of electrons. Ionic conductivity is mostly exhibited in liquid systems where the solution dissociates into positively charged cations and negatively charged anions. The current is due to the movement of these charged particles. The concentration and extent of the solution's dissociation affects the level of ionic conductivity.

For electrolytic processes, ionic conductivity is desired as it affects the system's efficiency. If electrons are flowing through the sample they are not participating in the desired reaction, they are considered wasted. However, certain levels of electronic conductivity are sometimes desired in order to maintain the temperature of the melt through ohmic heating. This has been exploited in the Hall-Héroult process. The method used to quantify the conductivity is dependent on what type of conductor is present. The conductivity of a pure electronic conductor is straightforward as it is directly related to Ohms law. If a potential is applied to the material and the current is recorded, the resistance can be determined by Ohm's law, as stated in equation 2.11. If the geometry of the current pathway is known, the calculated resistance value can be stated as a conductivity value as shown in equation 2.12.

$$R = \frac{V}{I} \tag{2.11}$$

$$\kappa = \frac{l}{AR} \tag{2.12}$$

Where κ is the conductivity (Sm^{-1}), l is the length (m), A is the cross-sectional area (m^2) and R is the resistance (Ω). For high temperature operations, the positioning and shape of the electrodes is an important factor in order to have a well defined current pathway. There are several specific electrode configurations which enable a reproducible, well defined current pathway [48]. A common technique when validating an electrode configuration is to measure a material with a known conductivity and experimentally determine the shape factor, $C = \frac{l}{A}$ (m^{-1}). Using the same configuration, this shape factor is used to calculate the conductivity of the unknown sample from the measured resistance, as shown in equation 2.13.

$$\kappa = \frac{C}{R} \tag{2.13}$$

Quantifying ionic conductivity requires alternating current (AC) analytical methods such as electrochemical impedance spectroscopy (EIS). EIS involves the application of an alternating current across a wide frequency range. The impedance is recorded and is composed of a real and imaginary part. The real impedance is plotted on the x-axis against the imaginary on the y-axis; this is referred to as a Nyquist plot. From this Nyquist plot, Figure 2.9, the electronic and ionic resistance values can be determined.

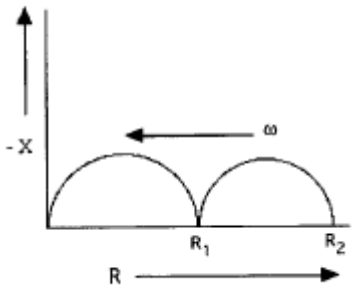

Figure 2.9: A Nyquist plot for a mixed conductor used to determine the ionic and electrical resistance of a sample. Obtained from: [49].

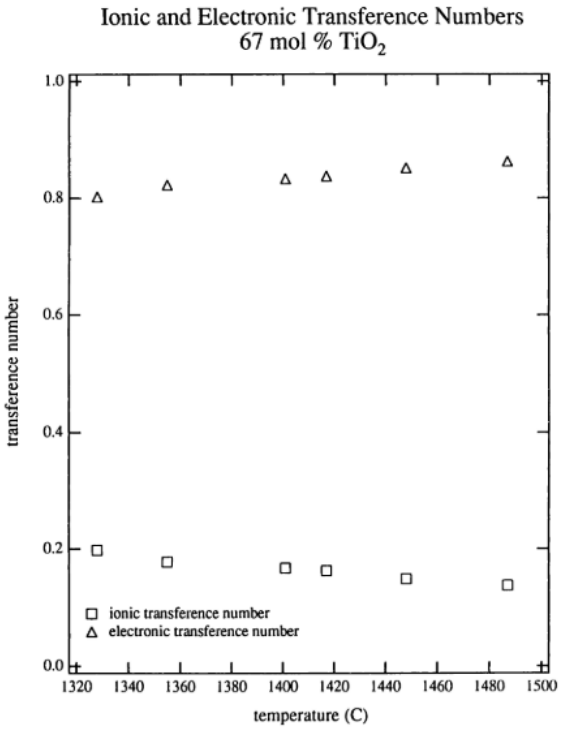

Figure 2.10: Variation in the transference number of a TiO_2 - BaO system with temperature. Obtained from: [50].

The transference number of a material is defined as the proportion of current carried by a specific species [49]. The transference number can be stated in terms of the relative proportions of ionic and electronic conductivity as shown in equation 2.14 and 2.15.

$$t_i = \frac{i_i}{(i_i + i_e)} \tag{2.14}$$

$$t_e = \frac{i_e}{(i_i + i_e)} \tag{2.15}$$

Where t_i and t_e are the ionic and electronic transference numbers respectively; i_e is the current carried by electronic conductivity; and i_i is the current carried by ionic conductivity. As a material's resistance varies with temperature, so does the transference number as shown as shown in Figure 2.10.

2.4 High Temperature Furnaces

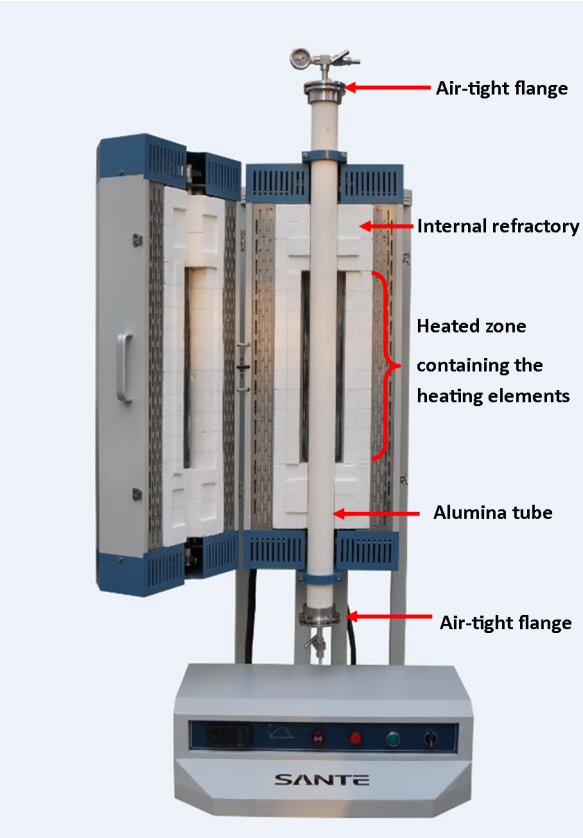

Figure 2.11: An annotated image of a split vertical tube furnace showing the internal structure. Adjusted from: [51].

Tube furnaces are frequently used in high temperature electrolysis experiments [42][41][36] due to their ability to control the atmosphere. A tube furnace is comprised of a central tube which is heated from its exterior surface by resistive heating elements. The tube is partially housed in an insulated box along with the heating elements which helps to maintain the temperature of the heated zone. The tube contains the sample and is orientated in either a horizontal or vertical manner. The vertical configuration simplifies the introduction of electrodes into the system and therefore is the primary orientation for electrolytic applications.

The choice of tube material is dependent on the maximum temperature of the furnace. Quartz, mulite, and alumina are common high temperature tube materials with maximum operating temperatures of 1200, 1500, and 1800°C respectively.

2.4.1 Thermal Stress and Strain

An important design consideration when using tube furnaces is the potential for the tube to fracture due to excessive thermal stresses. As the atmosphere is controlled, often to prevent oxidation, a tube fracture will result in an oxidising environment for the sample and any supporting systems. Thermal strain is defined as the expansion or contraction of a material due to a change in temperature. This is stated in equation 2.16.

$$\frac{\Delta L}{L} = \epsilon_T = \alpha \Delta T \tag{2.16}$$

Where L is the length of the original material (m), ε_T is the thermal strain, α is the linear coefficient of thermal expansion (K^{-1}), ΔT is the temperature change (K), and ΔL is the change in material's length (m).

Thermal stress occurs when this expansion or contraction is impeded by an external or internal constraint [52]. In the context of a vertical tube furnace, an external constraint could take the form of a clamp holding the tube at the correct height or the surrounding refractory preventing the tube from expanding. Internal constraints are primarily caused by sections of the material expanding by different amounts. This is caused by the material not having a uniform temperature which will result in part of the material expanding more than the rest [52]. Impurities or different phases in a material can result in sections of the material with a different thermal expansion

coefficient, so even if there is a homogeneous temperature distribution, there will still be thermally induced stresses [53]. An example of this is with alumina tubes which have been shown to display a higher thermal shock resistance at high purities [54].

Excessive thermal stresses can result in either the development, or the propagation of existing cracks which can cause a fracture [53]. To prevent this, external and internal constraints should be kept to a minimum. The external constraints can be minimised by holding the tube in a manner which allows for its free expansion and contraction, and ensuring the internal refractory is not inhibiting expansion. Internal constraints can be reduced by utilising high purity tube materials, and ensuring that the temperature distribution along the tube is even so that there is no sudden temperature changes. External and internal insulation can be applied to enforce this temperature distribution.

2.4.2 Radiative Heat Transfer

As the furnace temperature increases, radiative heat transfer becomes the primary form of heat transfer, due to the strong relationship between a materials temperature and the quantity of radiative energy emitted. This is described in the Stefan-Boltzmann law, and is shown in equation 2.17.

$$q_{emitted} = \sigma T^4 \tag{2.17}$$

Where $q_{emitted}$ is the emitted heat flux (Wm^{-2}), σ is the Stefan-Boltzmann constant (5.67 x $10^{-8}Wm^{-2}K^{-4}$), and T is temperature of the material (K). The Stefan-Boltzmann equation assumes that the material is a black body. Black bodies absorb all incident radiation (absorptivity = 1) and the quality and intensity of its emitted

radiation are solely dependent on its temperature [55]. Grey bodies are a more realistic description of a material and only absorb a portion of the incident radiation. The ratio between the energy emitted from a material and that of a black body is defined as its emissivity, ϵ. This will range from 1 (a perfect black body) to 0 (a perfect white body). Equation 2.18 states the emitted heat flux for a grey body.

$$q_{emitted} = \epsilon \sigma T^4 \tag{2.18}$$

When an emitted radiation wave impacts a surface it can do one of three things. It can be reflected, absorbed, or transmitted through the material. Graphically this is shown in Figure 2.12. The chance of this happening is based on the materials reflectivity (ρ), absorptivity (α) or transmissivity (t) values respectively.

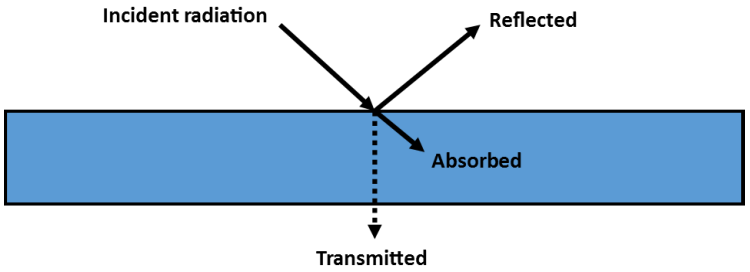

Figure 2.12: A graphical representation of an incident radiation wave and the potential interactions it can have with a material.

Applications involving radiative heat transfer often use thermal modelling software due to the complexity in determining the view factors and the time required to calculate the heat flux equations. In Section 4.3, an ANSYS model is utilised to produce a thermal model of the furnace. The equations below outlines how ANSYS models radiative heat transfer and the assumptions it makes.

The surface-to-surface radiation modelling method assumes that [56]:

- There is no incident radiation transmitting through the material (t=0) [55], i.e. all materials are opaque.
- All surfaces are diffuse, meaning that the reflected radiation is distributed evenly in every direction [55].
- All surfaces are grey, therefore that the emissivity and absorptivity are independent of wavelength [55].
- Kirchhoff's law applies ($\alpha = \epsilon$) [55]

With these assumptions in mind, the energy leaving a surface (referred to as surface k) can be stated as the sum of the energy emitted, based on equation 2.18, and the incident radiation that has been reflected. This is shown in equation 2.19.

$$q_{out,k} = \epsilon_k \sigma {T_4}^4 + \rho_k q_{in,k} \tag{2.19}$$

The relative geometries of the participating surfaces impacts the quantity of incident radiation. Formally this is know as the view factor which is defined as the proportion of radiation leaving surface 1 which impacts surface 2. By notation this is stated as: $F_{1\rightarrow 2}$. As this is a proportion, the sum of the view factors for a single surface will equal one.

Equation 2.20 describes the incoming heat flux for a surface from all other surfaces.

$$q_{in,k} = \sum_{j=1}^{N} q_{out,j} F_{jk} \tag{2.20}$$

Equation 2.19 and 2.20 can be combined to give equation 2.21

$$q_{out,k} = \epsilon_k \sigma {T_4}^4 + \rho_k \sum_{j=1}^{N} q_{out,j} F_{jk} \tag{2.21}$$

2.5 Framework

In summary, this chapter has highlighted the current state of titanium production and the research that has been performed to develop more efficient processes. Additionally, theoretical background to the relevant aspects of electrolysis, important physical properties of electrolytes, and important considerations for high temperature furnaces have been provided. The main body of this thesis is now broken into 4 chapters:

- Chapter 3: The development of an internal support structure for an ultra-high temperature furnace.
- Chapter 4: The thermal profiling of the furnace in order to commission and effectively use it.
- Chapter 5: The preliminary electrolysis experiments conducted on the NZS iron and synthetic slags.
- Chapter 6: The recommendations and conclusions of this research.

Chapter 3

Development of a Support Structure for an Ultra-High Temperature Furnace

This chapter focuses on how the furnace and supporting equipment was sourced and produced. It covers the previous work done to select a suitable furnace, the design, construction, and development of the furnace's support system which was required to melt and electrolyse a slag sample.

3.1 Furnace Acquisition

Figure 3.1: An image of a MTI GSL - 1700x-100VT-UL vertical tube furnace, purchased for this project. Obtained from: [57].

At the commencement of the project it was determined that an ultra-high temperature furnace would be required due to a lack of suitable equipment in the university. As such, work was carried out by former researchers [58] to purchase a suitable furnace, to design the necessary systems needed for an electrolysis experiment, and the subsequent sourcing of the materials. Below is a list of the criteria used to evaluate potential furnaces for purchase [58].

- It must achieve a temperature of 1700°C, which is well above the estimated melting point of the slag (1550°C [59]).

- It has to accept an outer tube diameter of 80 - 100 mm.
- A minimum heating zone length of at least 75 mm.
- An included controller capable of multiple heating/cooling segments.
- Ideally as compact as possible with a combined furnace controller assembly.
- A robust construction.
- Easy to operate and dismantle the tube.
- Potential or ability to interface with a computer.
- Compatible with existing labware and furnace accessories.
- The best value in terms of cost and performance.
- A reputable and reliable company with support.

8 furnaces were considered and ultimately the MTI GSL-1700X-100VT-UL furnace was selected as shown in Figure 3.1. The reasons for this decision are as follows [58]. The University of Canterbury has several MTI furnaces and they have been shown to be reliable. Before and after the purchase of these furnaces, MTI's customer service and technical support was found to be excellent. The MTI furnace has additional flexibility as it can use a 80 mm or a 100 mm alumina tube. The MTI furnace was the second cheapest furnace considered, costing 21,733 NZD. While the MTI furnace cost an extra 3,000 NZD than the (cheapest) Labec furnace, the added functionality meant it offered more value. For instance, the MTI furnace has an inbuilt stand to hold the alumina tube, has a small footprint due to incorporating the controller into the furnace and the package includes vital parts such as the alumina tube and flanges which would have to be bought alongside the Labec furnace.

3.2 Design of the Internal Support Structure

Due to selecting the MTI furnace, an internal structure needed to be produced in order to position the sample in the heated zone. The design not only had to hold the sample at the correct height, it had to allow for electrodes to be raised/lowered into the molten material while maintaining an inert environment within the tube. Former researchers of the University of Canterbury produced two preliminary designs for the internal support system. The hanging and bottom support designs are shown in Figure 3.2a and 3.2b respectively.

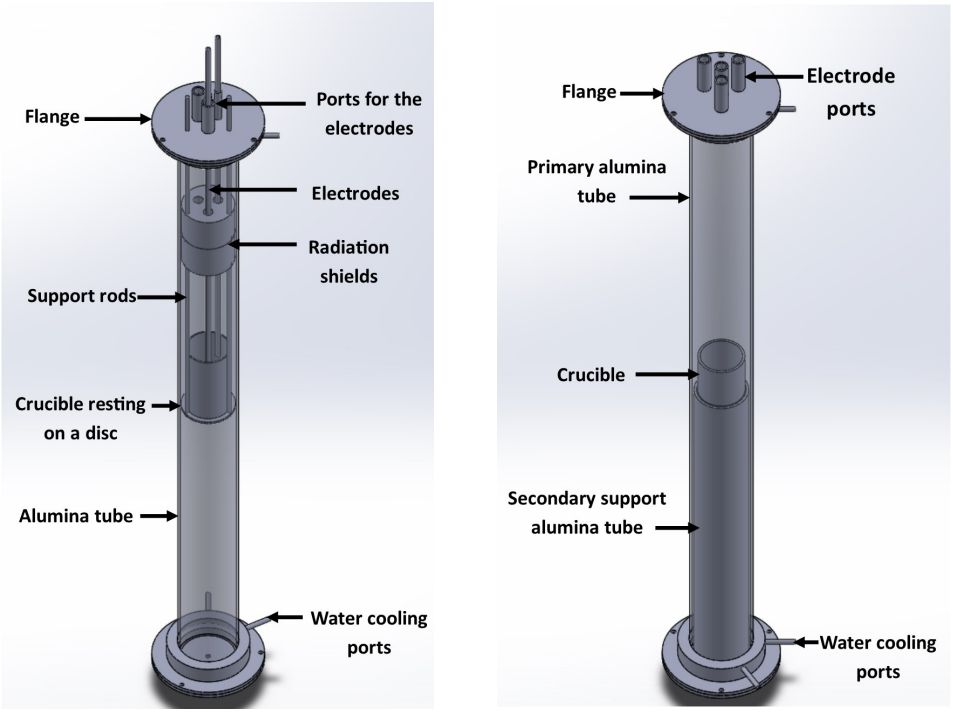

(a) The hanging support system. (b) The bottom support system.

Figure 3.2: Support system designs produced by former University of Canterbury researchers [58].

The hanging design, Figure 3.2a, involves suspending a disc from the top flange with three rods which in turn supports a crucible containing the sample. The bottom support design, Figure 3.2b, is composed of a small alumina tube which is located within the primary alumina tube, and rests on the bottom flange. The crucible can then be placed on top of the small alumina tube.

In terms of the advantages and disadvantages of the two options, the hanging support system requires more individual parts which need to be joined together which adds to its mechanical complexity. However, the support rods allow for the radiation shields and crucible to be positioned at various heights as opposed to the bottom support system which is at one fixed height unless other tube lengths are used.

The bottom support system is simplistic in nature as it only has one part. This allows for a very simple assembly but the long tube length and the density of alumina means that there is a significant amount of weight on the bottom flange. The bottom support system is considered to be inherently safer due its method of failure. If the support rods were to crack in the hanging design, it would result in the crucible being dropped onto the bottom flange. Depending on the mass of the sample this could cause the bottom flange to fail exposing the molten material to the surrounding area. In the case of the bottom design if the tube cracked it would still maintain its structural capabilities as the weight of the crucible and the remaining tube would hold it down.

It was decided that the general principles of the hanging support system would be adopted and continued to be developed. The primary reasons for its adoption was the design's flexibility in positioning the internal parts and its use of more commonly sized parts. The design, as provided, served as a starting point and needed to be developed further. Listed below are the criteria used to guide the continued development of the support structure.

- The structure must be able to maintain its structural integrity while operating in excess of 1650°C for prolonged periods of time.
- It must be able to be reused for a reasonable amount of experiments/thermal cycles.
- It should allow for a range of alumina rod/electrode diameters in order to widen the possible experiments that can be performed.
- It should allow for the placement of alumina blocks on either side of the hot zone in order to prevent the flanges from overheating due to radiative heat transfer and to maintain the heat in the hot zone.
- Ideally the parts should be able to be machined through the CAPE department's workshop and not require outside vendors.
- It should allow for the containment of an inert atmosphere to prevent reoxidation of the electrolytically produced material.

3.2.1 Material Options

The extreme operating temperatures of the furnace (1650°C) severely limited the choice of materials. Even among material classes such as ceramics, which traditionally have a high melting point, only a few members have a sufficiently high melting point e.g. alumina and yttria stabilised zirconia (YSZ). Refractory metals such as molybdenum, tungsten, tantalum, and rhenium can withstand the high temperatures but their performance is reflected in their price. Table 3.1 was created in order to compare potential materials. The cost, melting point, tensile strength, stability with respect to oxygen, and ease of sourcing were important parameters which were used as the selection criteria.

Table 3.1: Advantages and disadvantages of various materials considered for the support structure.

Material	Melting point (°C)	Cost (USD/kg)	Tensile strength, Ultimate (Mpa)	O2 stability	Availability
Platinum	1768	26,000.0 [60]	145 [61]	Stable	Uncommon
YSZ	1173-2690	72.0 [62]	745 [63]	Stable	Uncommon
Titanium	1668	56.0 [4]	220 [64]	Oxide layer	Uncommon
Tungsten	3422	30.0 [65]	300 [64]	Unstable	Uncommon
Alumina	2072	0.5 [66]	260 [67]	Stable	Common
Molybdenum	2623	24.0 [68]	515 [64]	Unstable	Common
Graphite	3642	1.1 [69]	41 [70]	Unstable	Common
Stainless steel	1400-1450	3.4 [71]	505 [72]	Stable	Common

From this comparison, only four materials (alumina, molybdenum, graphite, and stainless steel) could realistically be used for the various parts of the support system and these are examined in closer detail. As for the materials that where not selected, the reasoning was as follows.

- While platinum displays excellent corrosion resistance, stability in oxidising environments, and a high melting point, its extremely high cost renders it unsuitable. It may have been useful for small aspects of the design but materials such as molybdenum were able to perform a similar function more affordably.

- Yttria stabilised zirconia has better physical properties than alumina but it is not produced on the same scale which results in a limited range of parts which are more expensive than its alumina counterpart.

- Titanium was discounted due to having a melting point very close to the operating temperature. While it will remain as a solid up to 1668°C, it will lose most of its structural properties. It can be used as an oxygen capturing device if needed.

- Despite tungsten having a similar market price to molybdenum, it was only viewed as a potential oxygen capturing material due to its limited availability.

Alumina is a ceramic with an extremely high melting point, 2072^{o}C, and is sold in a wide range of forms and sizes at a low price. A 600 mm long, 6.35 mm diameter rod costs 35 USD [73]. The main issue with alumina is its extreme resistance to common steel tools and its brittle nature. Drilling alumina with steel drill bits results in the material shattering or at the very least cutting with a rough, imprecise edge. Abrasive tools such as diamond tipped drill bits allow for a cleaner cut but the range of drill sizes available limits what can be created. Common production methods for alumina involve a sintering/extrusion process which produces products with relatively large tolerances. For instance, the main alumina tube used for the furnace is stated as having an outer diameter of 102 mm $\pm$ 2 mm. Long threaded rods are not common which means connecting the various parts together would of had to be done with high temperature adhesives. Alumina is stable in inert and oxygen-rich atmospheres.

Molybdenum is a refractory metal and has been utilised by numerous research groups [42][34] for high temperature experiments. It is comparatively more expensive than alumina, 54 USD [74] vs 35 USD for a similarly sized rod, but overall it is an affordable material. Unlike alumina, molybdenum is soft enough to be machined with common tools and behaves similarly to cast iron when machined [75]. It maintains reasonable

mechanical properties while at high temperatures, allowing for a moderate amount of load to be held by small parts. Threaded molybdenum are readily available which offers a simplified method to connect the various parts together. While molybdenum has a high melting point of 2623 ^{o}C, it will oxidise to form gaseous MoO_3 at temperatures above 550^{o}C [76]. When cooled MoO_3 forms a white crystal structure. As such, molybdenum requires an inert environment in order to prevent degradation. Depending on the quantity of oxygen in the system, molybdenum's tendency to oxidise can be exploited to act as an oxygen sink and remove trace amounts of oxygen.

Graphite is a cheap, lightweight material and can be machined to a greater degree of precision than alumina but not to the same extent as molybdenum. A 12.7 mm OD rod which is 600 mm long costs 12.6 USD [77]. Graphite is mechanically weaker than either alumina or molybdenum and as such, if it was used to hold any significant weight, the part would have to be larger than its molybdenum or alumina counterpart. Like molybdenum, graphite has a high melting point (3642°C) but will oxidise to form CO or CO_2 when above 800°C. As such, it requires an inert environment. Graphite is a more cost effective oxygen sink than molybdenum and will form non-condensible gaseous CO_2 and CO as opposed to MoO_3 vapour which crystallises upon cooling (which would then have to be cleaned up).

The last material to be considered is stainless steel. The most apparent and significant shortfall of this material is its relatively low melting point of 1400 - 1450^{o}C. As such, it would not be able to be used as an internal material but it can be used in cooler sections of the furnace such as the flanges. The main advantages of using stainless steel is its low cost; it can be readily sourced; has good mechanical properties; and can be machined in-house into a wide range of parts.

3.3 Current Support System Design

The hanging support system shown in Figure 3.2a was used as a starting point and the design was further refined as more requirements became known. The final system is shown in Figures 3.3 and 3.5.

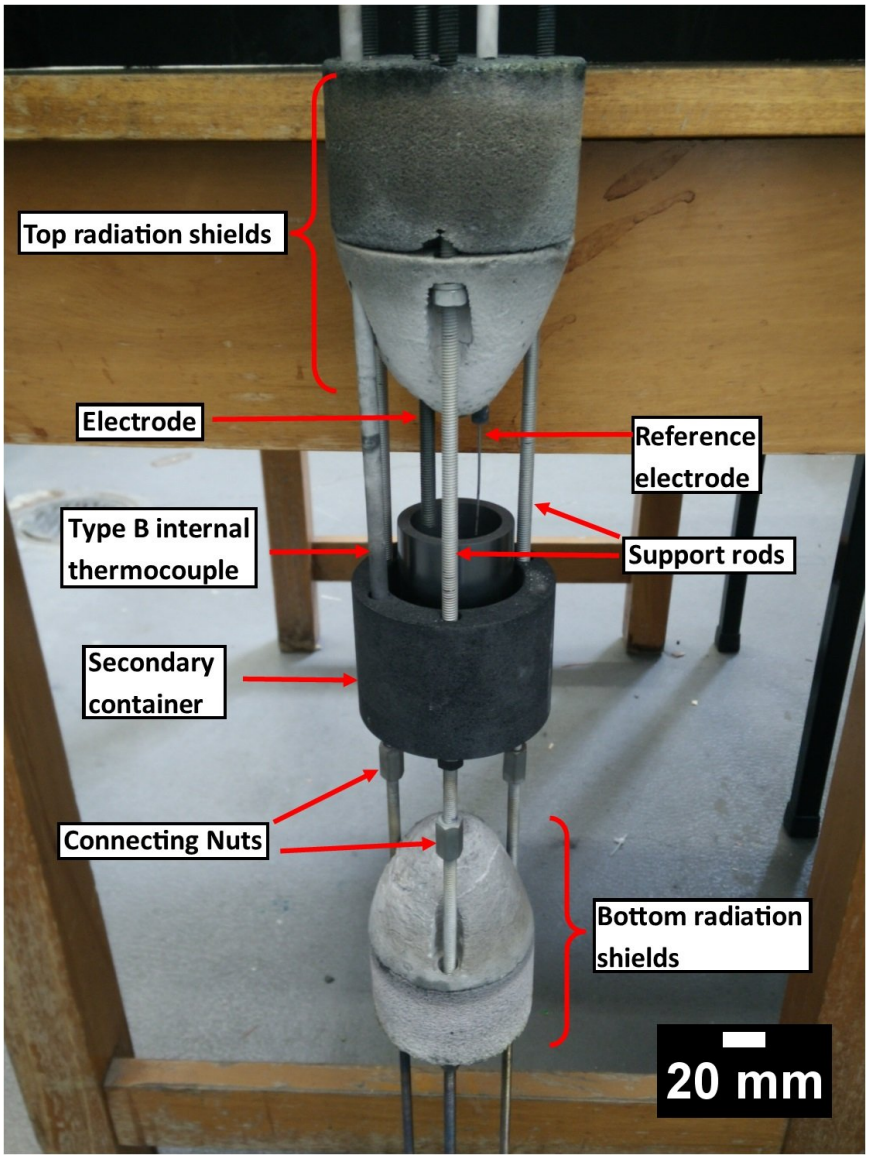

Figure 3.3: Annotated image of the current internal support system showing the various individual components of the structure.

Table 3.2 contains a summary of the constituent parts of the internal support structure and details the relevant dimensions, materials selected, and the supplier used. The functionality and the design decisions made about the individual components are explained in the sections to be follow. Appendix I contains dimensioned drawings of key components of the support structure.

Table 3.2: Bill of materials of the parts used in the support system.

Part	Quantity (all sizes in mm)	Material	Supplier
Flanges	2 assemblies	304 stainless steel	MTI
Radiation shields (cylinder)	2 x 80 D x 65 H	Foam alumina	” ”
Radiation shields (parabolic)	2 x 80 D x 65 H	Foam alumina	” ”
Secondary container	1 x 80 OD x 60 ID x 60 H	Graphite	Graphite Store
Support rods	3x M6 x 600 L,	Molybdenum	Extreme Bolt
	3 x M6 x 350 L		& Fastener
Connecting nuts	3 x M6 x 18 H	Molybdenum	” ”
Washers	15 x M6	Molybdenum	” ”
Nuts	15 x M6	Molybdenum	” ”
Crucible	1 x 45 OD x 35 ID x 80 H	Graphite	Baofeng Graphite

3.3.1 Flanges

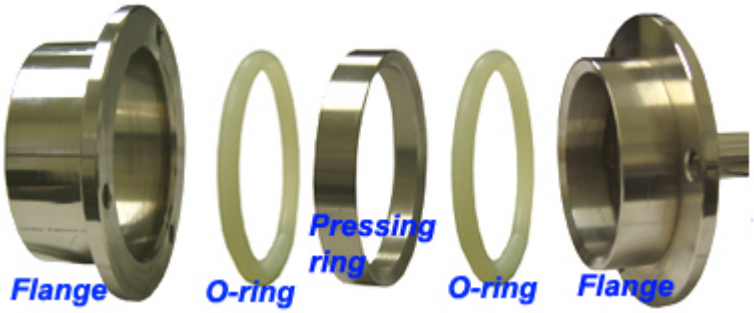

Figure 3.4: The individual components in the flange assembly. Obtained from: [57].

The purpose of the flanges is to control the gaseous environment inside the furnace's main alumina tube. Using the top flange as an example, the flange consists of two stainless steel sections. The lower section, left side of Figure 3.4, has a water cooling jacket, a slightly larger outer diameter than the alumina tube, and can freely move up and down the tube. The top flange section, right side of Figure 3.4, rests on the top surface of the alumina tube. To create an air tight seal two silicone O-rings and a steel pressing ring are situated between the two flange sections, which can be seen in the centre of Figure 3.4. The bottom flange section is raised and connected to the top section via three bolts. When the bolts are tightened the silicon O-rings are compressed against the flanges and the pressing ring, which creates an airtight seal.

The flanges are a stock item from the furnace manufacturer and have been modified to be fit-for-function. As shown in Figure 3.5, there are three ultra-torr^{TM} vacuum fittings which allow for items to be raised or lowered into the system. When the items have been lowered to the correct height the fittings can be tightened to create an effective gas seal. Two of these ports are dedicated to electrodes with the third outer-most fitting being used for an internal type B thermocouple. There are three holes to allow for the support rods to be connected to the flange as well as a gas

outlet. Should the crucible be used as an anode, the three support rods are electrically connected together to distribute the current evenly. Depending on the configuration of the radiation shields, water cooling may be necessary in order to keep the silicone O-rings below the maximum service temperature of 315°C [78]. The relatively low temperatures experienced by the flanges allow for the use of inexpensive stainless steel.

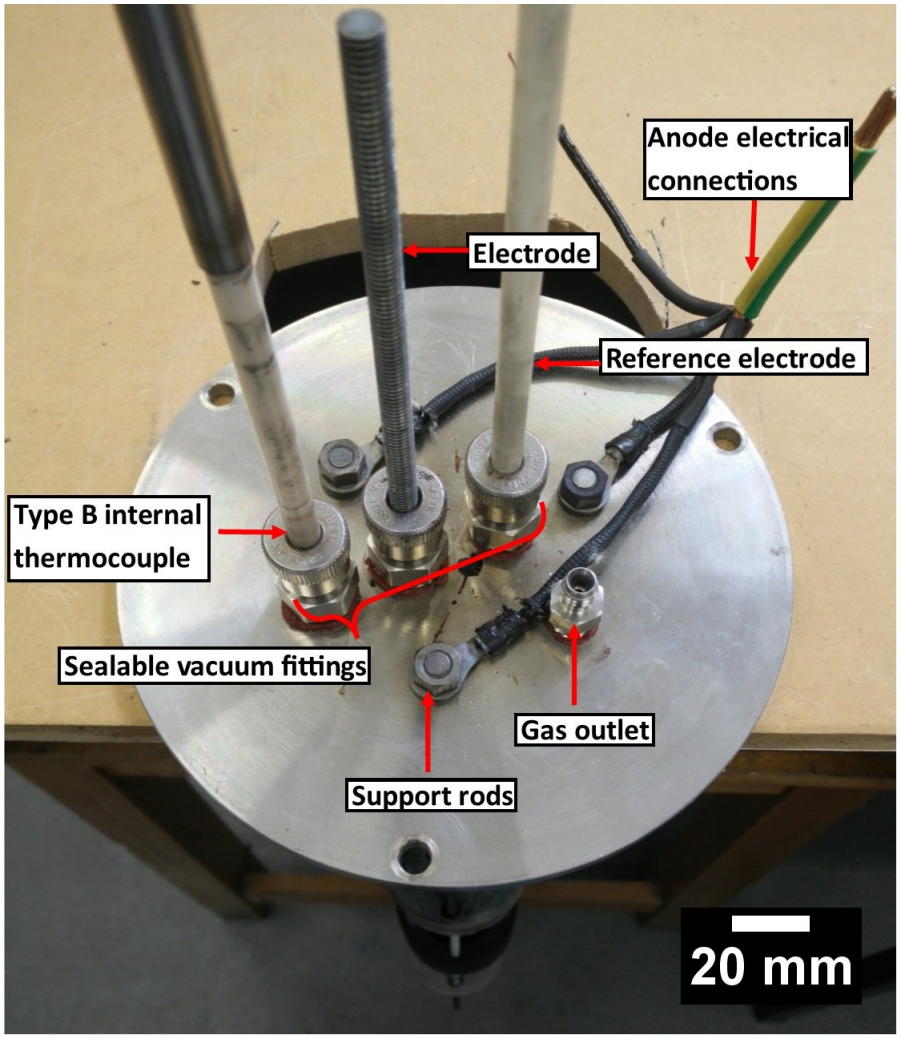

Figure 3.5: Annotated image of the top flange used in the support system assembly.

3.3.2 Radiation Shields

Radiation shields were positioned either side of the sample in order to reflect the heat back towards the hot zone therefore preventing energy loss. Two pairs of shields are located on either side of the sample. The blocks closest to the sample are parabolic in shape followed by a cylindrical shield, as shown in Figure 3.3. The reasons for this configuration are discussed in section 4.3. An ideal radiation shield should be able to maintain its structure while at high temperatures; be highly reflective; have a low thermal mass, and low thermal conductivity. This is so the incident radiation is not absorbed by the shield and propagated away from hot zone.

Two materials were considered and used during experimentation and these were foam alumina, and to a lesser extent titanium. Foam alumina was used for most experiments due to its high melting point, reflective properties, and low density. Titanium was only used in one experiment which showed that it was unsuitable due to poor mechanical properties at high temperatures.

3.3.3 Secondary Container

The secondary container holds the crucible and is present to capture any molten material that should escape in the event of the crucible failing. The crucible could fail due to a number of reasons such as corrosion by the molten material; being thermally shocked; or physically damaged by the electrodes if they were dropped and impacted the bottom of the crucible.

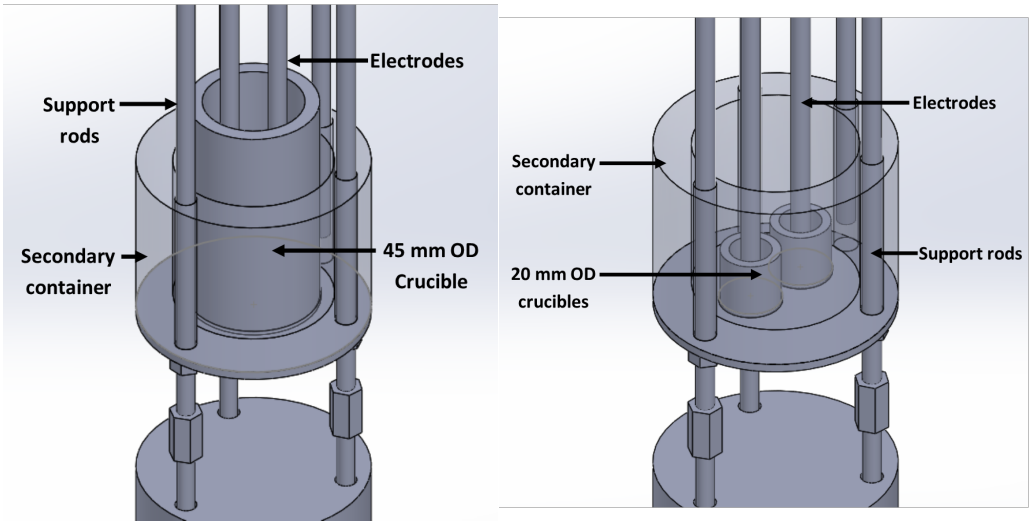

(a) 45 mm OD crucible.

(b) 20 mm OD crucibles.

Figure 3.6: Annotated images of the secondary container containing varying crucible sizes.

The secondary container also helps to keep the crucible in an ideal position for the electrodes. This is achieved by having a circle sunken into the bottom of the container which is slightly larger than the crucibles being used. An alternative design was created which allowed for two smaller crucibles as shown in Figure 3.6b. If the crucible fails the secondary container will most likely need to be disposed of and as such a cheap material should be used. Graphite was considered the most viable material based on its cost and low density. Alumina is also a cheap material but the number of holes that need to be drilled, along with its high density, makes alumina an impractical material.

Graphite's electrical conductivity allows for a crucible to act as an anode by providing the required electrical pathway from crucible to the molybdenum support rods, which can in turn be connected to a power source.

3.3.4 Support Rods

The support rods connect all of the support structure parts to the top flange. Six threaded molybdenum rods in total are used with half of them being 600 mm in length and the rest being 350 mm long. These two sections are connected with molybdenum connector nuts. The system is broken into two sections due to manufacturing constraints as 600 mm is the longest that can be provided. These threaded rods allow for the variable positioning of the radiation shields and the sample. This proved to be very valuable as the exact positioning of the radiation shield was a key aspect in maintaining the furnace's temperature which is discussed in Section 4.4.

Alumina and graphite were considered as potential materials but were determined to be less effective than molybdenum due to their physical properties. Also, as discussed previously alumina cannot be machined easily and as such threaded alumina rods are uncommon. Without a threaded assembly method, high temperature adhesives would have to be used which would make adjustments to the height of parts difficult. To compound this, high temperature adhesives need to be fired before they are effective and the bulky structure makes this challenging. Graphite threaded rods are available but are not ideal due to their degradation from daily use. Graphite is a weaker material than molybdenum and it is a risk that oxidation would weaken this further. Molybdenum rods are more expensive than graphite but their durability is greater.

3.3.5 Crucible

An ideal crucible in this context should be cheap, resistant to thermal shock, structurally stable at high temperatures, and must not be eroded by nor chemically affect the sample. Below is a list of crucible materials which were considered.

- Graphite
- Alumina
- Magnesium oxide
- Yittria stabilized zirconia
- Platinum
- Boron nitride
- Molybdenum

The NZS iron slag has been shown to chemically interact with platinum and alumina [79]. Alumina has also been shown to absorb the slag into its lattice structure. This absorption is not ideal as it creates stresses in the crucible as the different materials will cool with differing coefficients of thermal expansion. For brittle materials such as alumina, this can create fractures. Graphite and molybdenum have been investigated and do not show signs of significant chemical interaction/penetration. Graphite was chosen as the primary crucible material due to its chemical stability, wide range of sizes, and extremely low cost. Graphite's electrical conductivity was also considered a beneficial property as it allows the crucible to act as an anode.

An example of the interaction NZS iron slag has with the crucible material is shown in Figure 3.7. The interaction has been shown to be dependent on the iron/iron oxide content of the slag. Prepared synthetic slags which are of the same chemical composition, but are free of iron/iron oxide, do not display the interaction, as shown in Figure 3.8. The composition and use synthetic slags are discussed in greater detail in section 5.1.1.

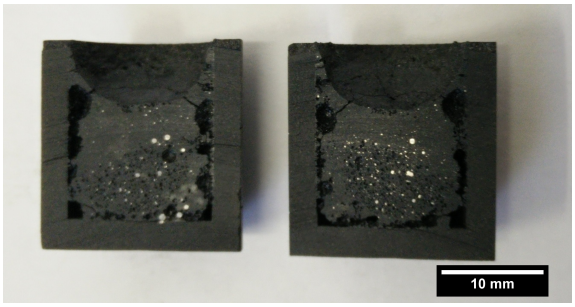

Figure 3.7: NZS iron slag displaying wetting behaviour in a graphite crucible, as indicated by the concave meniscus.

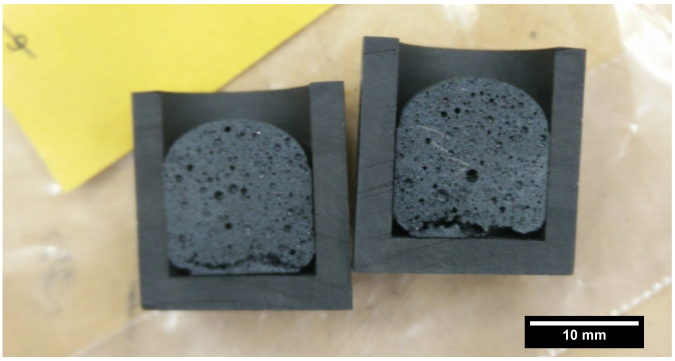

Figure 3.8: Synthetic slag #1 (free of iron) in a graphite crucible. The convex meniscus indicates a lack of wetting behaviour.

Chapter 4

Thermal Profiling Experiments

The previous chapter covered the work performed to design and develop an internal support structure for a MTI GSL - 1700x-100VT-UL vertical tube furnace, in order to facilitate electrolysis experiments. Before these electrolysis experiments were conducted, a series of commissioning experiments were performed to determine if the furnace was fit-for-purpose. During these experiments it was discovered, after a fracture developed in the alumina tube, that the system was susceptible to thermal shock and that the internal temperature differed from the furnace's stated temperature by a larger than expected margin. Before electrolysis experiments could be conducted, these issues had to be addressed so that the furnace could be used for multiple experiments without failure and at a suitable temperature. Due to the high cost and procurement time of the alumina tubes and support materials, a rigorous approach was required to minimise the chance of fracturing the tube. This highlighted that ultra-high temperature operations are challenging from an engineering perspective due to operating close to the limitations of the materials.

This chapter focuses on the work done to minimise the thermal stress on the system by experimentally examining the external insulation configuration and the internal position of the radiation shields. The geometric shape of the radiation shields was evaluated by the development of a qualitative ANSYS thermal model.

4.1 Commissioning the Furnace

There were two main goals of the commissioning process which are stated below.

- Confirm that the alumina tube and the flange seals would not fail during the process.
- Confirm that the support structure will maintain its structure and hold at the same height for the entire process.

To confirm these criteria, the furnace was heated to a temperature of 1600°C as described below.

4.1.1 Methodology

The support system was configured to hold a crucible with NZS iron slag sample in the constant temperature zone of the furnace with cylindrical radiation shields on either side. The position of the radiation shields was based on the recommended position from the manufacturer, which is shown in Figure 4.1. Both flanges were water-cooled at a flow rate of 1200 ccm to prevent the silicone O-rings from melting. The main alumina tube was held in place by two clamps at either end of the tube. The built-in clamps are designed so that the clamp will move with the tube as it expands in the longitudinal direction, preventing restricted thermal expansion of the tube. A 60 mm ID, 35 mm high molybdenum crucible was 70% filled with NZS iron slag. The sample

was heated to 1600°C, held for 90 minutes, and then cooled to room temperature. The heating/cooling rates used were 10°C/min when below 1200°C and 5°C/min when above 1200°C. These were the recommended rates from the furnace manufacturer [78].

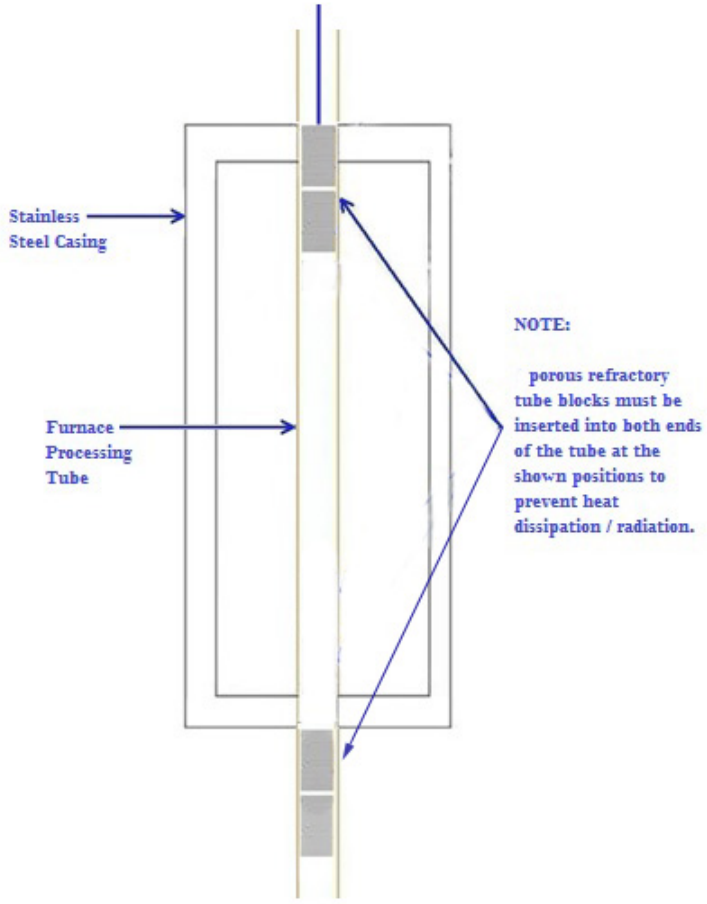

Figure 4.1: The recommended placement of the radiation shields for a MTI GSL-1700x100VT-UL vertical tube furnace by the manufacturer. Obtained from: [57].

4.1.2 Alumina Tube Fracture

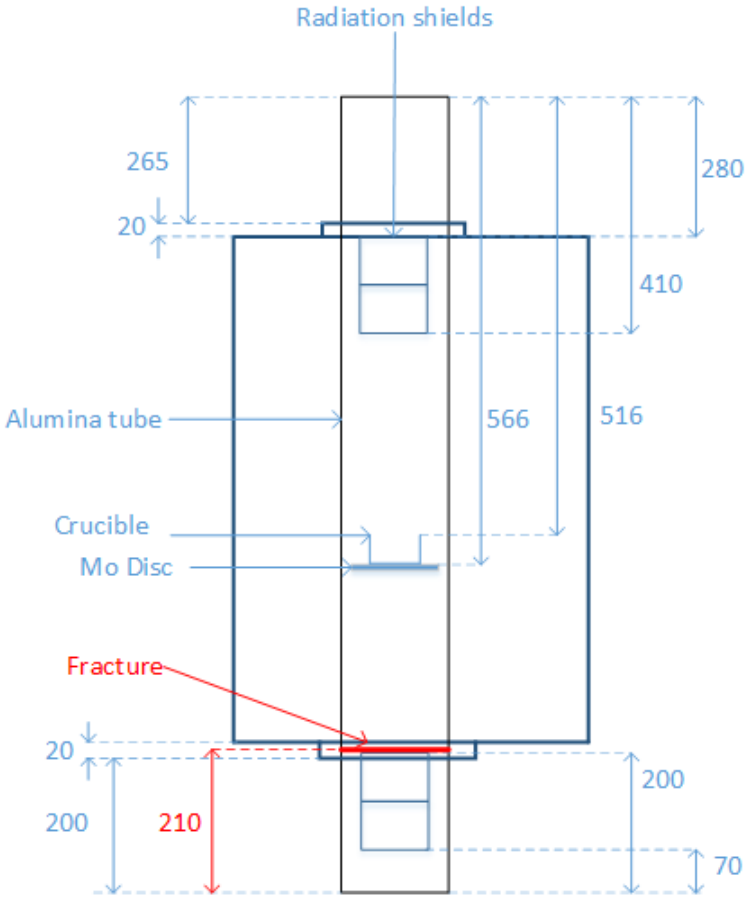

Figure 4.2: The fracture in the alumina tube is shown in red along with the support structure's configuration.

Once the furnace was at room temperature, the alumina tube was inspected and it was discovered that there was a circumferential fracture located in the bottom half of the tube, close to where the tube exits the internal refractory as shown in Figure 4.2. Factors which contributed to the fracture and how to minimise these were investigated.

Previously in Section 2.4.1 it was discussed how thermal stress is due to the restricted expansion from internal or external constraints. The most prominent external constraints are the clamps holding the tube in place. They were not considered to be a major constraint due to their ability to expand with the tube. However, as the tube can be fully supported with a single clamp, subsequent experiments only used one clamp to reduce this constraint.

A heterogeneous temperature distribution along the tube is a prominent form of internal constraint and large temperature changes can result in the propagation or development of the cracks. The fracture is localised, as shown in Figure 4.2, in the bottom half of the tube, close to where the tube emerged from the internal insulation. The top face of the radiation shields was also in close proximity to the fracture. It was believed that the absence of the external insulation resulted in a large drop in temperature due to the ambient air cooling the tube. While this was not specified in the furnace's operating procedure, it was evident that this should have been implemented. The effects of the external insulation are explored in section 4.2.

The general recommendation for high temperature tube furnaces is to spread out the longitudinal temperature gradient as much as possible to reduce the maximum [80]. This is done by applying external insulation in a tiered fashion so that the thickest part of the insulation is where the tube emerges from the internal refractory. This helps to prevent a sudden drop in temperature when the tube leaves the internal refractory. As distance from the opening increases, the insulation thickness is reduced so that the temperature can dissipate before it contacts the flanges which have specific temperature requirements. In terms of the radiation shield placement, this was specified by the manufacturer. It is theorised that the flat face of the shield reflected the radiation towards the sides of the tube, creating a localised hot section.

This in turn would have created stress and therefore would have contributed to the fracture. The heating/cooling rate is an important factor to consider as it effectively propagates a temperature difference along the tube during the heating/cooling process. As the tube is heated/cooled it takes time for the tube's temperature to equilibrate and a high rate will temporarily create high thermal gradients. Likewise, a slow heating/cooling rate allows the tube to more closely resemble its equilibrium condition as it is heating/cooling. The heating/cooling rates stated in the user manual, 10°C/min when below 1200°C and 5°C/min when above 1200°C, were compared against other recommendations to determine if they were appropriate.

Researchers at Callaghan Innovation were contacted as they routinely operate high temperature tube furnaces. They recommended a rate between 1-2°C/min [79]. This value was echoed by an alumina tube supplier, McDanel Advanced Ceramic Technologies, who recommended a rate of 1.7°C/min [80] for a similarly dimensioned alumina tube and also advised against the use of multiple heating/cooling rates. Based on these recommendations a constant heating/cooling rate of 1°C/min was implemented in all subsequent experiments.

Correspondence with MTI revealed that they are aware of the furnace's sensitivity to thermal shock and that it is not uncommon for alumina tubes to break on their first use [81]. This painted a rather bleak outlook on the frequency of tube fractures with the existing system. As it was not practical to be constantly replacing the alumina tube, work needed to be done to improve the furnace configuration with the longevity of the alumina tube in mind.

Factors influencing the temperature distribution along the alumina tube

The variables that could affect the temperature gradient on the system were identified and are listed below. As it was not definitive which factor contributed the most to the fracture, all factors that could practically be improved, were.

- Heating/cooling rate.
- Thickness and height of the external insulation.
- The position of the radiation shields.
- The geometric shape of the radiation shields.
- The use of water-cooling in the flanges.
- The operating temperature.
- The diameter and thickness of the alumina tube.

The two factors that were not addressed were the operating temperature and the diameter/thickness of the alumina tube. The operating temperature cannot be changed as a liquid slag is required for an electrolysis process and this is a fundamental parameter. The thickness of the alumina was investigated but economically, a thinner walled tube would not be practical. All of the other factors are addressed in sections 4.2 and 4.3.

4.2 External Thermal Profile Experiments

4.2.1 Introduction

The absence of external insulation material was previously identified as a source of stress for the system. The ideal configuration of the insulation material was unknown and experiments were conducted to quantify the longitudinal thermal gradient on the exposed alumina tube sections, and to use it as a metric. The experimental thermal gradient values were compared against a literature source [80] for a tolerable thermal gradient (3.9°C/mm) and used to guide the configuration of the insulation material. The temperature of the flanges was also monitored in order to determine if water cooling would be required to keep the silicone O-rings below their maximum service temperature of 315°C.

A series of experiments were conducted which involved heating the furnace to a certain temperature, then recording the alumina tubes external temperature profile once it had reached equilibrium. 1200°C was used as the first hold temperature as the relatively low temperature was unlikely to result in immediate failure conditions. The hold temperature of subsequent experiments would be increased in steps if the flange and thermal gradient values were below their maximum values. If the two conditions were not met then the configuration of the insulation would of been adjusted. This was a cautious approach due to the expense of the materials in question and the lead time to acquire them.

4.2.2 Methodology

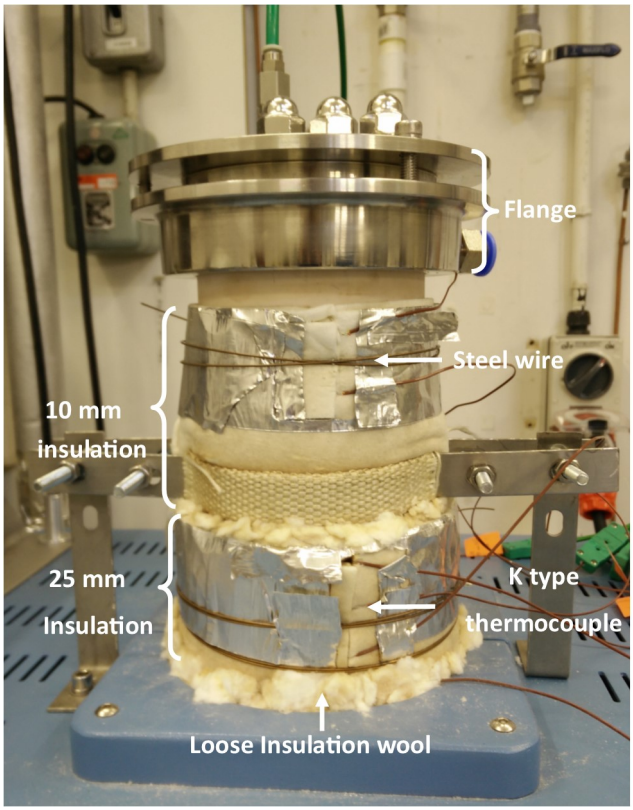

Figure 4.3: Annotated image of the insulation's configuration on the top section of the alumina tube.

To measure the temperature along the alumina tube, 10 K-type thermocouples were produced (5 per section). The thermocouple beads were held against the side of the alumina tube at known, fixed locations so that with the recorded temperatures, a thermal gradient could be calculated. The thermocouples were held in place with various layers of blanket Kaowool^{TM} which in turn was held in place via thin gauge steel wire which was wrapped around the insulation and gently tightened. This configuration is shown in Figure 4.3.

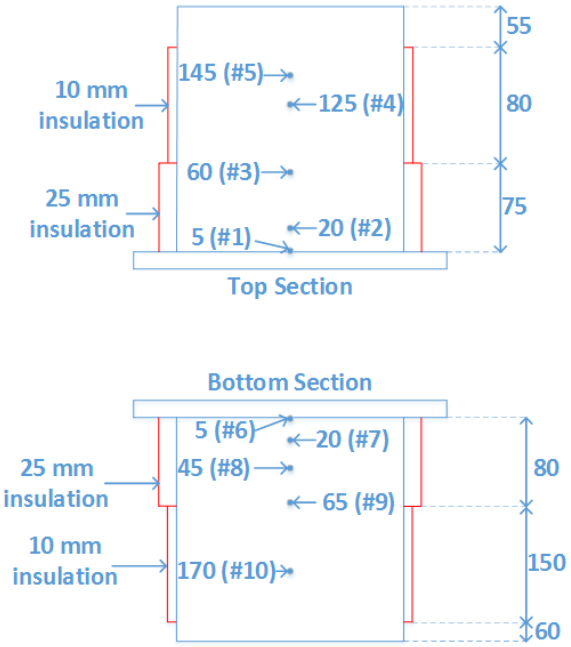

Figure 4.4: The structure of the external insulation and position of the thermocouples. The distances are stated in mm and are relative to the tube's opening from the internal insulation.

Figure 4.4 shows the relative position of the thermocouples and the tiered structure of the insulation. When the alumina tube transitions from the internal to external insulation, there is potential for a large temperature change due to the relatively high localised temperature. This issue is compounded by alumina displaying weaker mechanical properties at high temperatures, and therefore is more susceptible to fractures [54]. To address this, the thickest part of the insulation, 25 mm uncompressed, is situated where the tube emerges from the internal refractory. Loose insulation wool was gently packed into the spaces where the blanket could not reach. As the alumina tube progressed away from the opening, the thickness of the insulation was reduced to 10 mm and is then absent right before the flange.

The thermocouples were connected to two USB TC-08 Pico data loggers which recorded the temperature at 1 minute intervals. For each experiment, the furnace was heated at a rate of 1°C/min, and held at temperature for 90 minutes before measurements were taken to allow for the tube's temperature to stabilise. After the hold sequence the furnace was cooled at a rate of 1°C/min. The main alumina tube was held in place with only one clamp on the bottom tube section in order to reduce the external constraints to a minimum.

4.2.3 Results and Discussion

Figure 4.5 and 4.6 details the thermal gradient values for multiple experiments, across the length of the top and bottom alumina tube sections respectively. The experiment temperature was varied between 1200°C and 1600°C, with water-cooled flanges used in three experiments when they were required. The recommended maximum thermal gradient value is 3.9°C/mm [80]. The maximum measured thermal gradient values are shown in Figure 4.7.

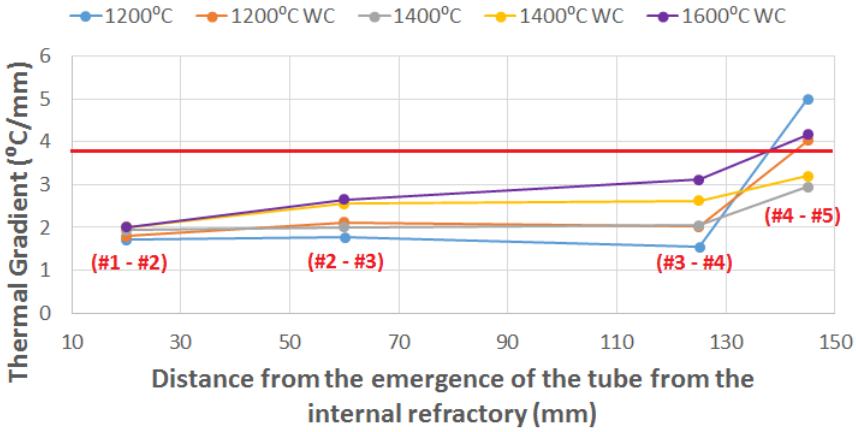

Figure 4.5: The exterior thermal gradient of the top alumina tube section. The "WC" denotes the use of water-cooled flanges. The red horizontal line represents the maximum thermal gradient. As discussed, the results from thermocouple #4 and #5 were not used to draw conclusions.

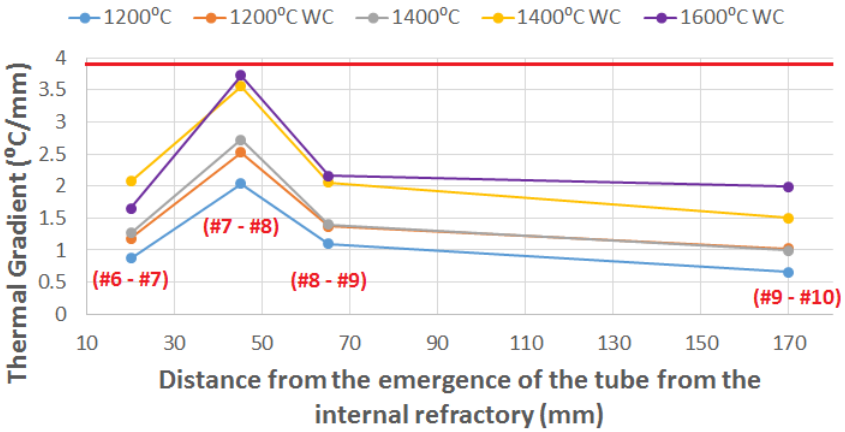

Figure 4.6: The exterior thermal gradient of the bottom alumina tube section. The "WC" denotes the use of water-cooled flanges. The red horizontal line represents the maximum thermal gradient.

During experimentation, thermocouple #5 showed signs of intermittent physical contact with the tube, which corresponded to large deviations in the reported temperature. Therefore, the thermal gradient between thermocouple #4 and#5 was overstated and was not used to draw conclusions. It is included in Figure 4.5 for comparison. The first experiment performed was at 1200°C and the highest thermal gradient value obtained was 51% of the threshold. The highest values for the top and bottom sections were 1.78 and 2.04 °C/mm respectively. The temperature of top and bottom flanges were also below the maximum service temperature of silicon (315°C) at 95 and 127°C respectively.

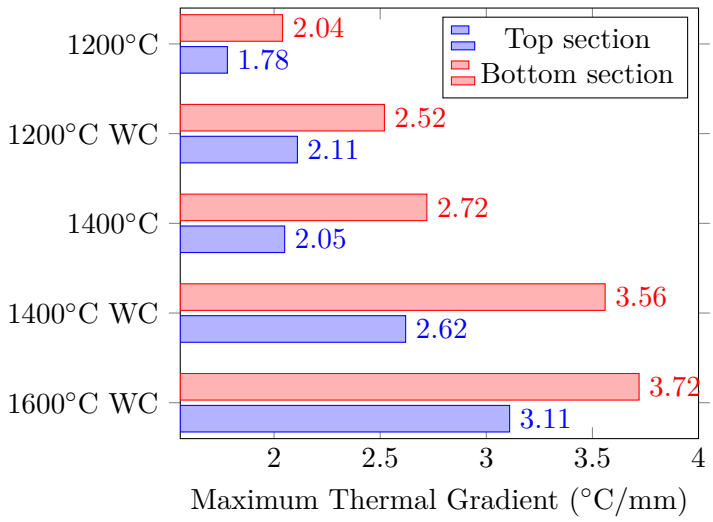

Figure 4.7: The maximum thermal gradient values obtained from the top and bottom alumina tube sections, across five experiments. The suffix "WC" indicates the use of water-cooled flanges.

As the conditions were met, the next experiment was performed at 1400°C. The 200°C increase in the furnace temperature resulted in thermal gradient increasing by 0.27 and 0.68°C/mm, for the top and bottom sections. Previous flange temperature measurements were obtained by manually pressing a thermocouple against the exterior section of the flanges. The 1400°C experiment had the thermocouple fixed in position for the entire experiment; positioned between the flange and the alumina tube. The temperature of the top and bottom flange increased to 329 and 281°C, surpassing the maximum service temperature. Consequently, the configuration of the flange had to be adjusted before the temperature of the furnace could continue to be heated. Water cooling was added to the flanges in order to reduce the temperature of the O-rings. Other options were considered, as discussed in Appendix B. There was uncertainty as to what degree the water-cooled flanges would influence the thermal gradient and as such, the 1200°C experiment was repeated with the use of water cooling in order to determine their effect.

The experiment showed that the inclusion of water-cooled flanges, relative to the non water-cooled 1200°C experiment, had increased the maximum thermal gradient for the top and bottom sections by 0.33 and 0.48°C/mm. This is the same order of magnitude as increasing the furnace temperature from 1200°C to 1400°C. With the effects of water cooling established, the last experiment held the furnace at 1400°C for 90 minutes and then progressed up to 1600°C.

Ultimately the 1600°C experiment showed that the thermal gradient of the top and bottom sections were 3.11 and 3.72°C/mm, which did not exceed the recommended maximum of 3.9°C/mm. Therefore, the insulation configuration was deemed to be appropriate, and did not stress the alumina tube with excessive thermal gradients.

4.2.4 Conclusions

External insulation was applied to the exposed sections of the alumina tube in order to prevent a rapid drop in the alumina tube's temperature when it emerged from the internal refractory. The external insulation configuration was extensively tested, across a temperature range of 1200°C to 1600°C, which showed that the alumina tube sections were not subjected to excessive longitudinal thermal gradients. Water-cooled flanges were shown to be required in order to maintain the temperature of the O-rings below there maximum service temperature.

4.3 Modelling of the Internal Thermal Profile

The geometric shape of the radiation shields were considered to be a contributing factor to the high thermal gradient experienced by the alumina tube. One theory was that the flat face of the radiation shields resulted in an abrupt axial temperature gradient, thereby creating a local area of excessive thermal stress. As covered in section 2.4.2, radiative heat transfer is determined primarily by the temperature of the surfaces involved and their geometric shape. In complex geometries, view factors are difficult to calculate by hand which promotes the use of modelling software such as ANSYS or COMSOL.

Thereafter, a qualitative ANSYS model was developed which simulated the temperature across the alumina tube including the external insulation and the radiation shields. The primary aim of this model was to determine the longitudinal thermal gradients of the alumina tube and to vary the geometric shape of the radiation shields in order to find a geometry which minimised the maximum thermal gradient. In the interests of time, it was decided to produce a qualitative, as opposed to a quantitative model. A qualitative model will not be a perfect representation of the furnace but allows for relative comparisons between the shield geometries.

4.3.1 Model Description

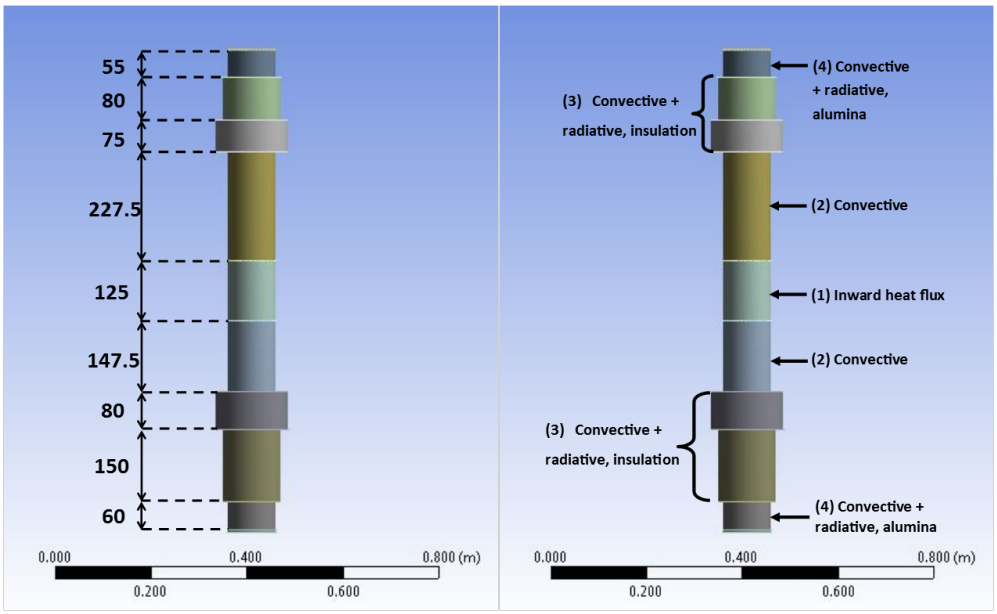

(a) (b)

Figure 4.8: The modelled geometry used in the ANSYS simulation annotated to show the dimensions (on the left) and the heat fluxes applied to them (on the right).

The main alumina tube, external insulation, and radiation shields were modelled in SolidWorks and imported into ANSYS. Dimensionally, this model is accurate to the physical system and is shown in Figure 4.8a. The main alumina tube was sectioned into 4 unique parts due to different fluxes being applied. Figure 4.8b shows these sections and the types of applied fluxes. Despite being sectioned, all parts are bonded together to allow for conduction between them. Section (1) represents the heated section of the tube which is 125 mm high. This portion of the tube was assumed to be the only heated section and had a heat flux of 3380 W applied evenly across its area. This heat flux is based on the maximum energy consumption (5580 W) of the furnace and the applied flux is 65% of this. This percentage is an estimated value and gives section (1) a temperature between 1643 and 1920°C depending on the radiation shield configuration.

On either side of the heated zone (1) are the sections of the tube which are inside the internal refractory but not directly heated (2). A convective heat transfer term (8 W/m^2 °C) is applied to these tube sections, which is a simplified representation of the heat flux leaving the tube by the internal refractory. The tube now "exits" the internal refractory and the tube sections (3) are wrapped in external insulation material in the same configuration used in the section 4.2.2, as described in Figure 4.4. It is assumed that the insulation is tightly wrapped around the tube and therefore there is no convective cooling on the alumina tube directly. Heat can propagate from the alumina tube to the insulation via conduction. Radiative and convective heat transfer terms were applied to the outward facing insulation surfaces to represent the heat transfer to the ambient air (22°C). The temperature dependent convection coefficients used were built-in, tabular values for a vertical plane which range from 3.8 to 14.2 W/m^2 °C.

The last sections (4) of the alumina tube were those which were not covered by the external insulation and are the outer most sections of the alumina tube. Here, as they are exposed to ambient conditions, they have a convective and radiative heat transfer term applied to them. The alumina tube was sealed at either end with a 5 mm thick steel disc which acted as the flanges. They were subjected to convective and radiative heat losses and conduction to its connected alumina tube section.

The internal radiative heat transfer was modelled with ANSYS' surface-to surface mode. This model assumes that the system is perfectly enclosed; all surfaces are grey, diffuse and opaque; and Kirchoff's law applies. Section 2.4.2 has explored these assumptions along with the equations which ANSYS uses to determine the heat fluxes. From these assumptions, it can be stated that the only radiative material property required is the emissivity which was obtained from literature and is 0.57 and 0.075 for alumina, and steel respectively [82]. As the experimental heating/cooling rate is

extremely low, 1°C/min, it was assumed that the system would not deviate much from its equilibrium conditions and therefore a steady state model was considered. An initial temperature of 200°C was set for all bodies.

4.3.2 Results and Discussion

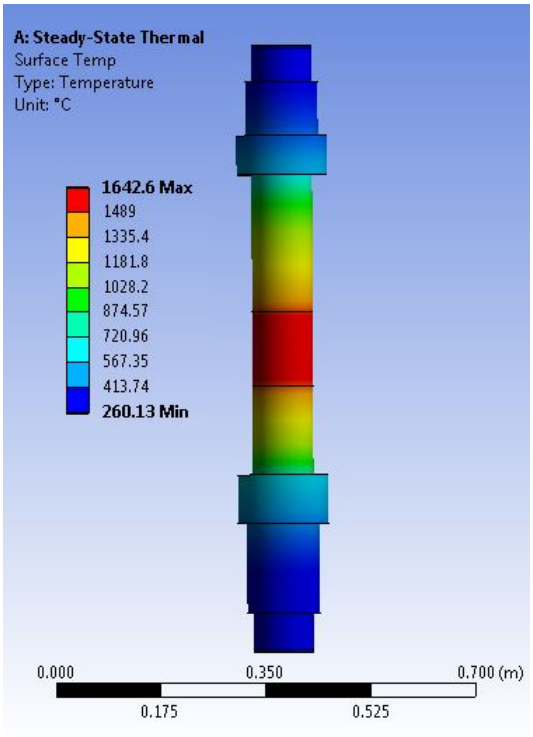

Figure 4.9: The temperature distribution along the modelled geometry when no radiation shields are used.

Five unique shield geometries were considered which were: parabolic, half-parabolic, conical, cylindrical, and stacked discs. The geometries are shown in Figure 4.10 and for each geometry the maximum diameter and height were kept constant at 80 mm and 130 mm respectively. The geometries were incorporated into individual thermal models as well as a system without any shields. The models calculated the temperature across the system and an example of this is shown in Figure 4.9.

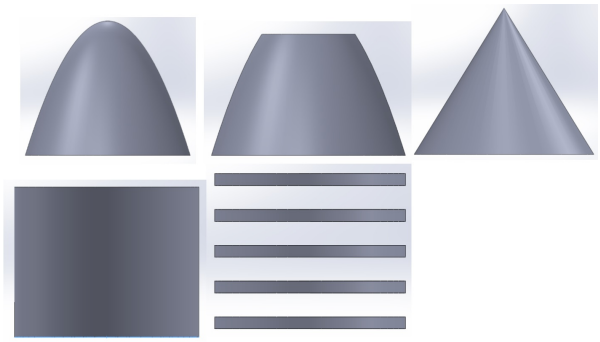

Figure 4.10: Starting at the top left, the geometries considered were: parabolic, half-parabolic, conical, cylindrical, and a series of stacked discs.

Figure 4.11 plots the temperature and calculated thermal gradient values against the height of the alumina tube to show the location of the maximum thermal gradients. Four definitive peaks are observed and occur either side of the heated section (1), and where the system transitions from the internal to external insulation (2).

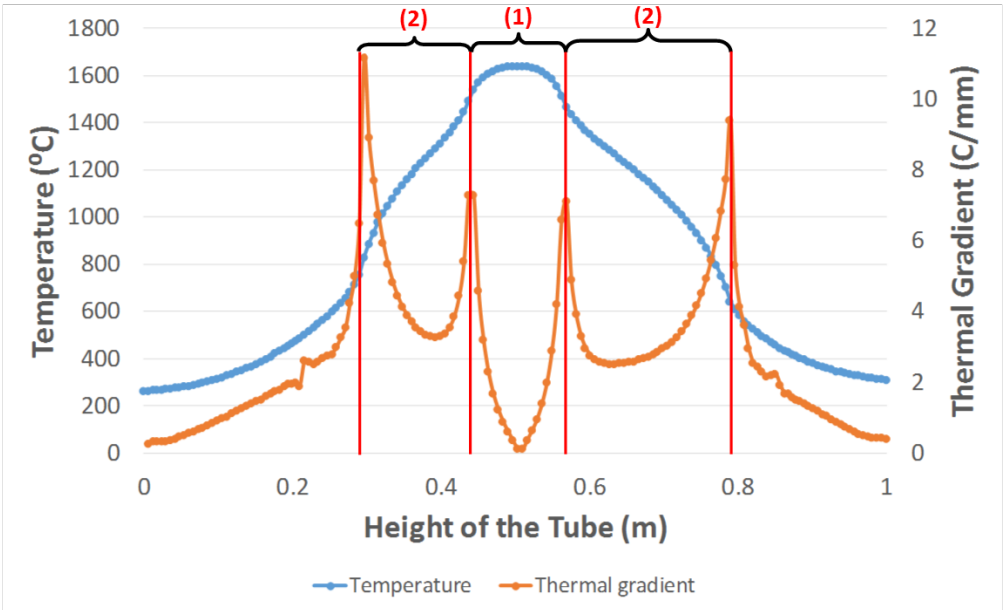

Figure 4.11: The temperature and thermal gradient values plotted against the height of the alumina tube when no radiation shields are used. Two pairs of peaks occur, the first where the heated zone (1) ends, and the second where the internal insulation zones (2) end and transitions to the external insulation.

The magnitude of these peaks is due to an underestimation of the outgoing heat fluxes from the internal portions of the tube. However, the position of thermal gradient peaks in the transition between the external and internal insulation are realistic. As detailed in section 4.1.2, a fracture due to a temperature difference occurred in this location.

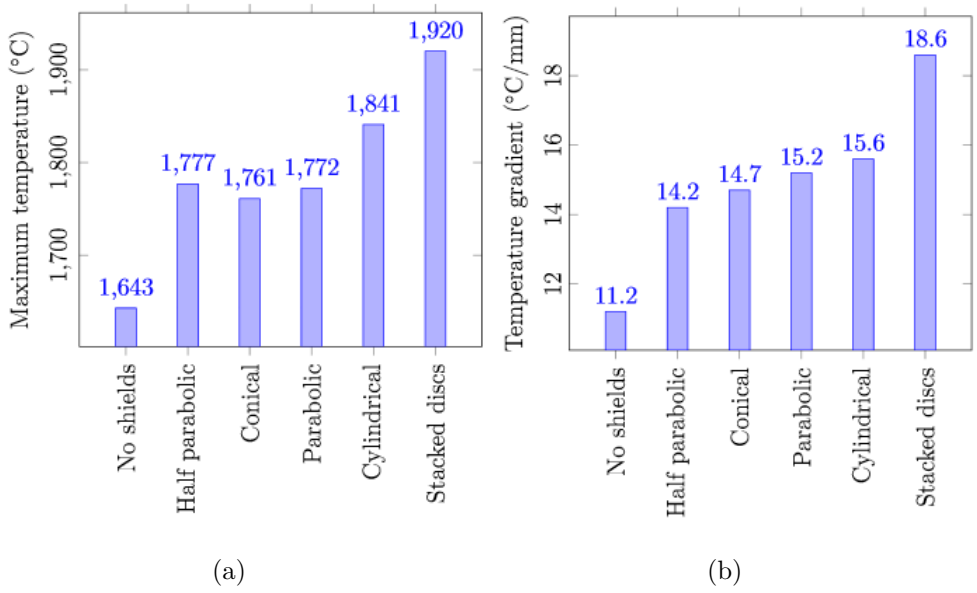

(a) (b)

Figure 4.12: The maximum temperatures (on the left) and thermal gradient values (on the right) obtained from six thermal models with different radiation shield geometry configurations.

Figure 4.12a and 4.12b compares the performance of the various geometries in terms of maximum thermal gradient and temperature respectively. The system without radiation shields showed a greater temperature distribution as reflected by its maximum thermal gradient of 11.2 °C/mm. However, its distribution of heat has resulted in a relatively low maximum temperature of 1643°C. This reinforces the established notion that radiation shields are needed in order to maintain the heat in the furnace. The use of cylindrical radiation shields significantly improves the maximum temperature (from 1643 to 1841°C) but at the expense of the maximum thermal gradient (11.2 to 15.6

°C/mm). This highlights that this is a balancing act between the various factors. The extreme of this is shown with the stacked discs configuration which had the highest maximum temperature of 1920°C but was also accompanied by the highest gradient of 18.6°C/mm.

The parabolic, half parabolic, and conical geometries all showed lower thermal gradients than the cylindrical geometry, with varying maximum temperature values. The most notable of these is the half parabolic which, out of the three, had the highest maximum temperature (1777°C) and the lowest thermal gradient (14.2°C/mm). When compared against the default geometry, there is still a trade off between heat retention and the thermal gradient. However, in the interests of lowering the thermal gradient, it is the most suitable geometry.

In subsequent experiments, parabolic radiation shields were adopted. A parabolic, rather than half parabolic, geometry was used due to late alterations/fixes to the model. Previous versions of the model showed the parabolic had the lowest thermal gradient but the necessary alterations changed the results of the conical and half parabolic geometries which rendered them more effective that the parabolic. For future work, it is suggested that the half-parabolic geometry be used instead.

4.3.3 Conclusions

The thermal modelling of the various radiation shield geometries highlighted the trade off between heat retention and its distribution. The stacked discs geometry had the highest internal temperature of 1920°C but at the expense of having the highest thermal gradient of 18.6°C/mm. The half parabolic geometry had the lowest thermal gradient (14.2°C/mm) and maintained a temperature of 1777°C, and as such is the recommended geometry. If this model is to be developed further for quantitative purposes, there is potential for the external tube temperature values obtained in section 4.2 to be used to validate the model.

4.4 Internal Temperature Discrepancy

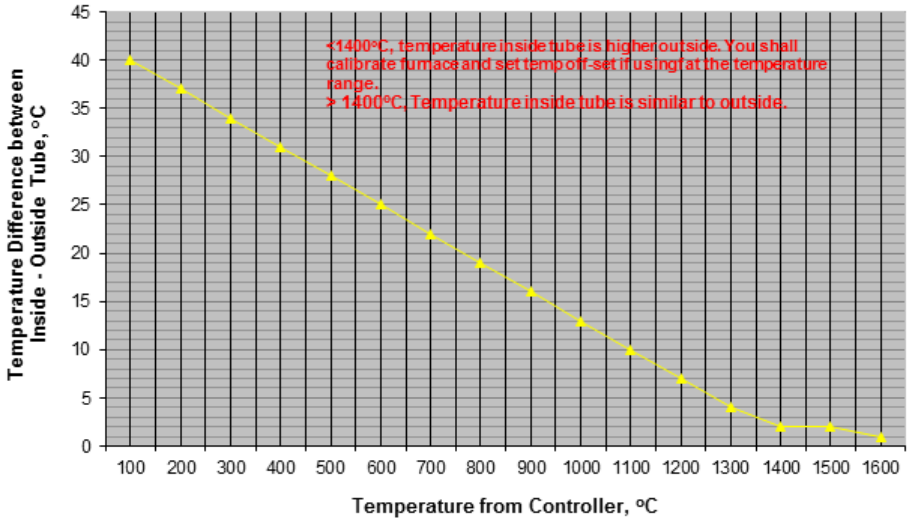

Figure 4.13: The predicted internal-external alumina tube temperature difference as stated by the manufacturer. Obtained from: [57].

According to the manufacturer, and as shown in Figure 4.13, it is expected that there will be a radial temperature gradient whereby the outside of the tube is hotter than the interior. The manufacturer recommended recording the internal temperature and then adjusting the controller to account for the difference. To verify the internal temperature and adjust the controller accordingly, a type B thermocouple was obtained from National Basic Sensor. The first measurements showed that there was a significantly larger temperature difference than expected. According to Figure 4.13, a temperature difference of below 5°C should be achieved past 1250°C. In tests this difference was 150°C. The large temperature difference could have been due to several factors: The internal temperature probe may not have been in the hottest part of the furnace; the controller/data-viewer may have been misrepresenting the voltage of the thermocouple; or a significant quantity of heat may have been drawn away from the constant temperature zone lowering its temperature.

To determine if the controller/data-viewer was misrepresenting the voltage, the built-in furnace's thermocouple voltage was measured using a high accuracy voltmeter while the furnace was at high temperature. A high accuracy voltmeter was required for this measurement as type B thermocouples produce a small signal relative to their temperature. When the furnace controller stated that the temperature was 1600°C, the voltage of the controller thermocouple was 11.22mv. This corresponds to 1600°C as indicated by the voltage table which can be seen in appendices C. At the same time, the internal thermocouple stated that the temperature was 1426°C and the measured voltage was 9.40mv. This corresponds to a temperature of 1430°C. These measurements showed that the controller/data viewer were accurately reporting the voltages produced by the thermocouples, and therefore the temperatures.

The next factor was the location of the constant temperature zone. In theory, the middle of the constant temperature zone is situated 500 mm from the top of the alumina tube and is 125 mm in size according to the manual [78]. Previous experiments have had the tip of the thermocouple 515 mm from the top of the alumina tube. The aim of the experiment was to confirm the location and size of the constant temperature zone, and to see if it varied at different temperatures. The furnace was set to hold at 1400°C and then heated to 1600°C.

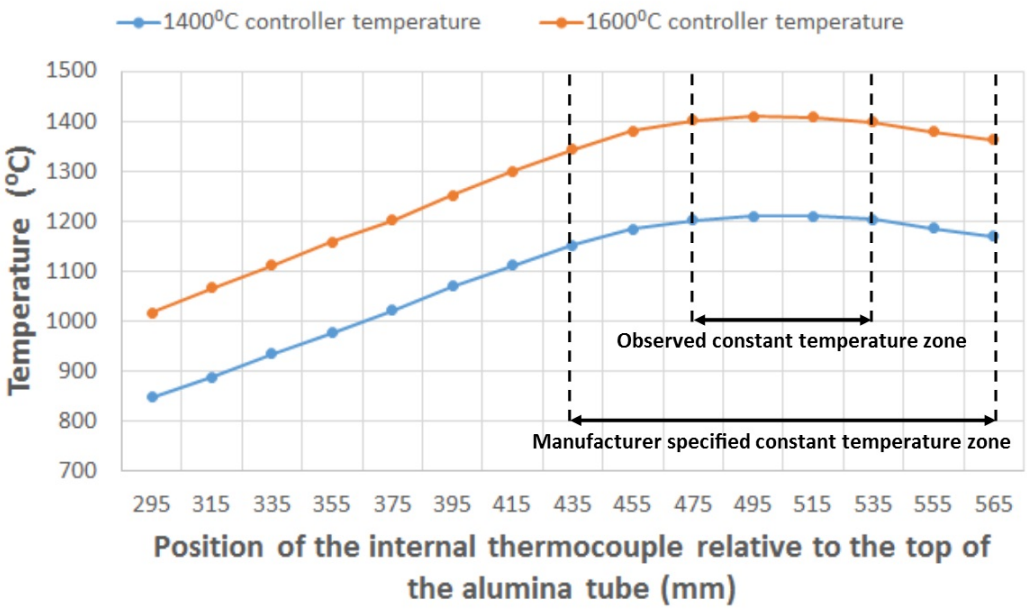

Figure 4.14: The measured internal temperature of the furnace showing the position of the constant temperature zone.

Once the furnace had equilibrated to its hold temperature, the internal thermocouple was lowered down and measurements were taken every 20 mm. Figure 4.14 shows that the constant temperature zone is 60 mm in height, a departure from the 125 mm as stated by the manual. The size of the observed constant temperature zone did not vary significantly with respect to the temperature but this is a narrow temperature range (1400-1600°C).

4.4.1 Radiation Shield Positioning

In order to electrolyse the slag it has to be a liquid in order to promote the free movement of charge and material. In order to melt the slag, the furnace has to reach an internal temperature of 1550°C [59]. As the furnace can reach 1650°C for long periods of time, a temperature difference of 100°C was considered manageable. A smaller discrepancy is preferable as it reduces the maximum temperature the furnace would be subjected to and therefore increase the life span of the alumina tube.

While there are other minor aspects of the system that could account for a small difference in temperature, namely the radial position of the internal thermocouple or the protective alumina sheath, the most likely reason for the temperature difference was that heat was being drawn away from the constant temperature zone. To counteract this the support system, and the radiation shields specifically, needed to be adjusted. Five experiments were carried out which had multiple aims and Table 4.1 summarises the results. Each experiment adjusted the position or geometry of the radiation shields and recorded the temperature as stated by the controller and measured internal temperature as stated by a type B thermocouple.

Table 4.1: The difference (°C) between the stated temperature of the furnace's controller and the measured interior temperature across various radiation shield positions.

#	Description	1200°C	1300°C	1400°C	1600°C	1650°C
1	Minimal shields	190	185	-	-	-
2	Thin titanium shields	-	-	-	132	-
3	Even shield placement	-	-	115	112	-
4	75 mm separation	-	-	105	85	-
5	65 mm separation	-	-	-	-	77

Experiment #1 featured the use of only the parabolic radiation shields and they were positioned 10 mm away from the flanges, as shown in Figure 4.15a. This experiment acted as a control as the parabolic radiation shields are only present to reduce the temperature experienced by the flanges. The furnace was heated to a controller temperature of 1200°C and then onto 1300°C. At these temperatures, the temperature difference was 190 and 180°C respectively.

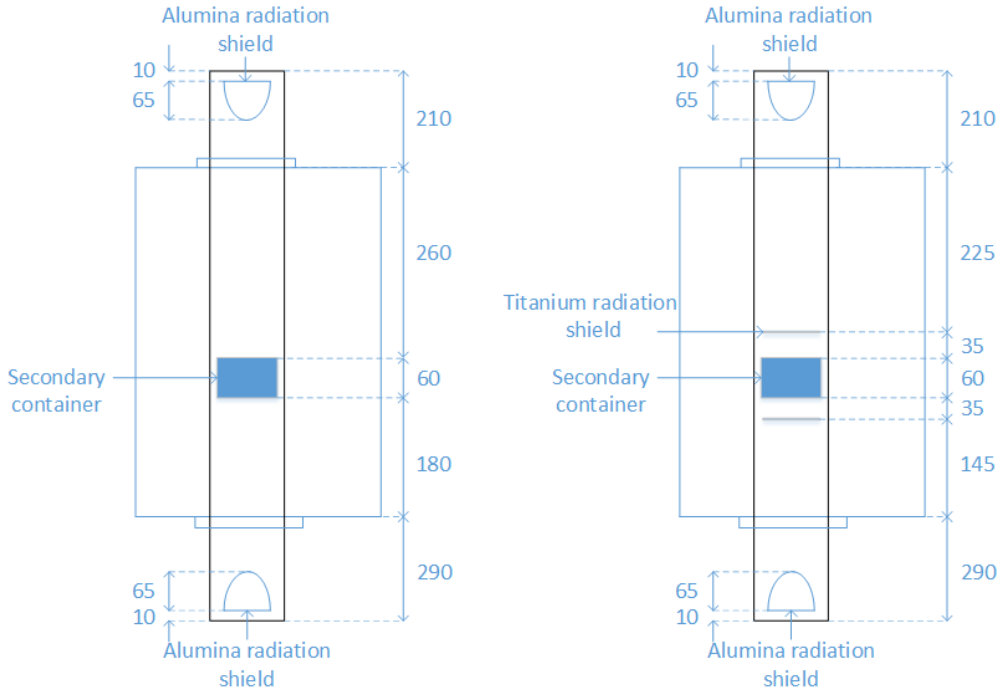

(a) Experiment #1 configuration. (b) Experiment #2 configuration.

Figure 4.15: The internal support configuration for experiment #1 (on the left) and #2 (on the right). All measurements are stated in mm.

Thin titanium radiation shields were considered in experiment #2 as an alternative to alumina shields as the material could be easily machined and could act as a oxygen-capture device. They were positioned 35 mm from the secondary container's outer faces as shown in Figure 4.15b. The discs had a diameter of 80 mm. The temperature difference was 132°C but resulted in significant warping and damage to the titanium

discs as shown in Figures 4.16a and 4.16b. Despite their thin nature, they were able to reduce the temperature difference significantly which suggested that a tiered structure of thin discs could be an effective shield configuration. Nonetheless, the additional parts could needlessly increase the complexity of the system.

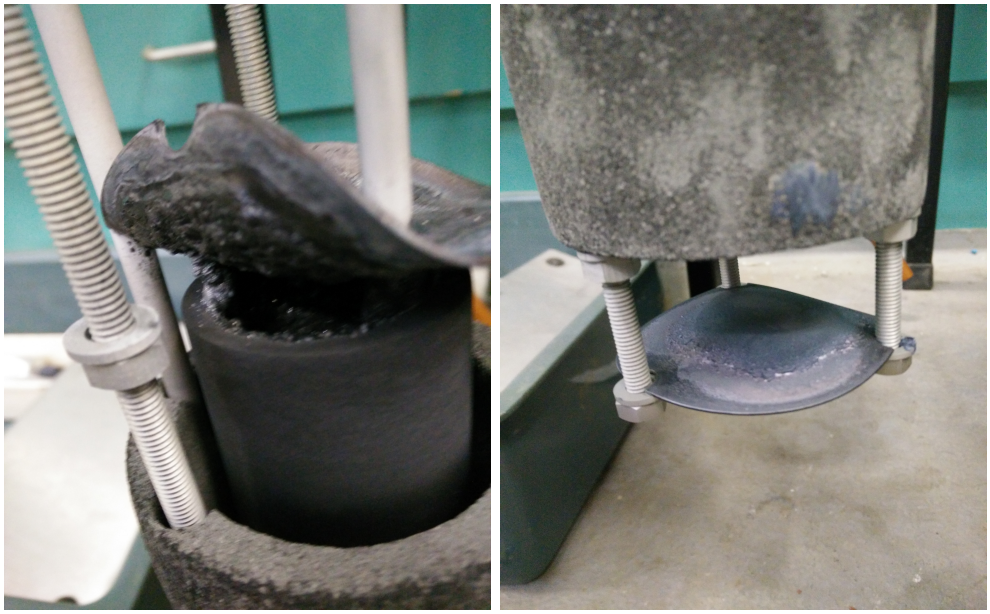

(a) Top titanium shield. (b) Bottom titanium shield.

Figure 4.16: The top and bottom titanium radiation shields after being fired to 1600°C.

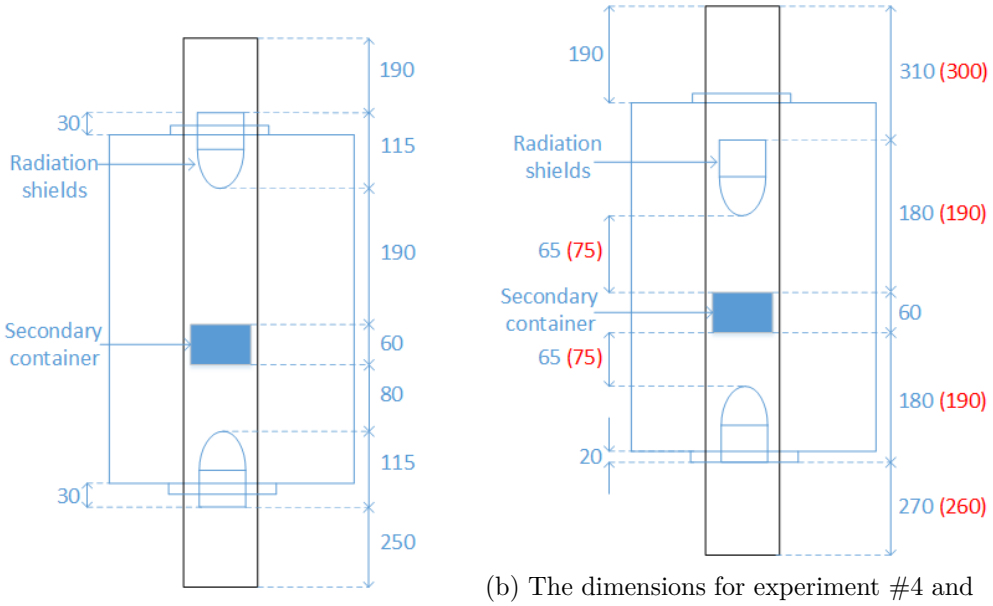

(a) Experiment #3 configuration.

(b) The dimensions for experiment #4 and #5 are stated by the blue and red values respectively.

Figure 4.17: The internal support configuration for experiment #3 (on the left) and #4-5 (on the right). All measurements are stated in mm.

Experiment #3 positioned the radiation shields in close proximity to the transition between the internal and external insulation and is shown in Figure 4.17a. The temperature difference was lowered to 112°C. In experiment # 4, the radiation shields were reconfigured so that they were evenly placed with respect to the secondary container and therefore the constant temperature zone. The configuration of the radiation shields is shown in Figure 4.17b. The tip of the radiation shields were 75 mm away from the outer face edge of the secondary container which is significantly closer than the last experiment. This reduced the temperature difference to 85°C. While this was not ideal, the difference had been reduced enough for electrolysis experiments.

Experiment #5 was in combination with an electrolysis experiment and it further reduced the gap from 75 to 65 mm. This was to see how much the difference could be improved upon. The position of the radiation shields is shown in Figure 4.17b and the dimensions used are stated in red. The internal furnace temperature was able to reach 1573°C which corresponds to an offset of 77°C as opposed to the 85°C difference of the previous experiment.

4.4.2 Conclusions

The experiments showed that the primary reason for the temperature offset was due to the position of the radiation shields. The data in table 4.1 shows that alumina radiation shields are needed and that they have to be close to the hot zone to be effective. The smallest temperature difference obtained between the measured interior and furnace controller was 77°C. While this is a workable temperature difference, this is unlikely to be the optimal configuration and it should therefore be re-visited. The reason for not pursuing this further is that the system is usable for preliminary electrolysis experiments in the current configuration.

4.5 Conclusions

This chapter has detailed the work done to minimise the identified factors which caused a fracture to develop in the alumina tube, during the commissioning experiments. A tiered configuration of external insulation was applied to the exposed alumina tube sections, to prevent a sudden drop in temperature when the tube emerged from the internal refractory. The configuration was determined to be suitable across a temperature range of 1200 to 1600°C via five thermal profile experiments. Water-cooled flanges were determined to be necessary in order to maintain their functionality above 1400°C.

A qualitative ANSYS thermal model was developed which examined the geometric shape of the radiation shields and their effect on the thermal gradient experienced by the alumina tube. It was determined that a half-parabolic geometry contributed the least to the maximum thermal gradient.

Lastly, the difference between the temperature as stated by the furnace's controller and the measured internal temperature was examined. A suitable position for the radiation shields was established which lowered the temperature difference from 190°C to 77°C. Overall, the risk of the alumina tube fracturing due to excessive thermal stresses was reduced. This allows for high temperature electrolysis experiments to be conducted.

Chapter 5

Electrolysis Experiments

Once the furnace was able to reach high temperatures without failure, start-up followed by baseline experiments were conducted. This chapter covers the work done to develop a suitable experimental methodology, the preliminary electrolysis experiments and the subsequent analysis.

5.1 Start-up Experiments

In order to maximise the utility of the thermal profile experiments, basic electrochemical experiments were run at the same time. They were carried out with the desire to perfect the system and methodology for future experiments. The improvements obtained ranged from basic user experience, to broadening the understanding of the system's electrical conductivity. The two experiments described below aimed to identify the potential at which the faradaic reactions occurred at, through the performance of linear sweep voltammetry. This was unsuccessful but did give an insight into the electrical conductivity of a NZS iron slag and synthetic slag system.

5.1.1 Electrical Conductivity of a NZS Iron Slag System

In the first experiment, 135 grams of powdered NZS iron slag was heated in a 35 mm ID, 80 mm H graphite crucible to a furnace temperature of 1600°C which corresponds to an interior temperature of 1468°C. The configuration of the support system is identical to the one shown in Figure 4.15b. A three electrode configuration was used with three molybdenum wires being used for the cathode, anode, and reference electrode and were contained in a quad bore, 1.57 mm ID, 6.35 mm OD alumina tube. Once at temperature the electrodes were lowered into the slag. To do this the vacuum fitting was loosened so the alumina sheath could be freely moved. Before the experiment, the height of the alumina sheath, relative to the top surface of the flange was measured when it was level with the slag. This was done in order to provide an estimate of how much the alumina sheath needed to be lowered. The sheath was lowered and when it was close to the predetermined height, the resistance between the cathode and anode was measured with a voltmeter. The resistance was used as an indicator to determine when electrical contact was made. When the resistance dropped significantly, it was assumed that the electrode had just touched the slag. The electrodes were then lowered to their desired depth (15 mm) and the sheath was held in place by tightening the vacuum fitting.

Operating under the knowledge that a faster scan rate would produce a sharper current peak/trough, a 1000 mV scan rate was provided by the model 371 Princeton Applied Research potentiostat and a model 175 universal programmer. The voltage was swept from +2V to -2V between the cathode and anode. Examination of the voltage-current graph, as shown in Figure 5.1, did not reveal any major current peaks or troughs which would be indicative of a faradaic reaction. The inverse gradient of the linear trend line showed that the resistance of the system was 0.39 Ohms.

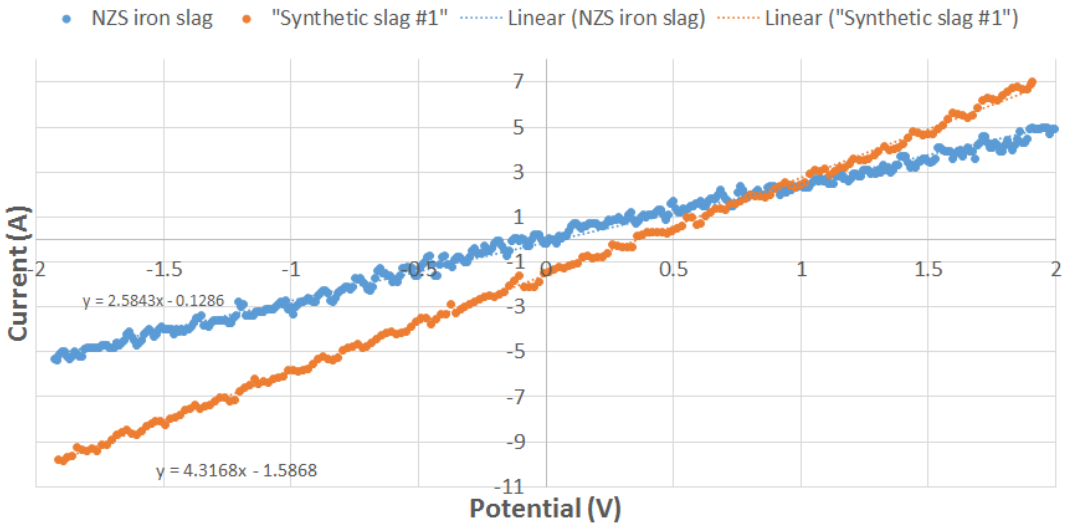

Figure 5.1: +2V to -2V linear voltage sweeps on the NZS iron and synthetic slags at a scan rate of 1000 mV.

One of the possible reasons for such a low resistance was the presence of 4.3% iron oxide and an unknown quantity of metallic iron; a left-over production from the iron-making process in the NZS iron slag. It was theorised that removing the iron and iron oxide from the system would reduce the electronic conductivity of the slag.

Several synthetic slag blends were commissioned from Callaghan Innovation. These blends had varying levels of TiO_2 and the majority components found in the slag. These synthetic slags did not contain any iron, iron oxide, or trace chemical components. They were produced as it was suspected that iron oxide would hinder electrolytic extraction due to its high electronic conductivity and low reduction potential.

5.1.2 Electrical Conductivity of a #1 Synthetic Slag System

In the second experiment synthetic slag #1 was used which, as shown by Table 5.1, has a similar chemical composition to the NZS iron slag. A similar methodology was used except, as this was done at the same time as the thermal profile experiments, the radiation shields were different. The support system configuration has been shown in Figure 4.17b. 130 grams of synthetic slag #1 was added to a graphite crucible which was heated to a furnace temperature of 1650°C, which corresponds to an interior temperature of 1568°C. The voltage was swept in the same manner as the previous experiment and showed a similar absence of faradaic peaks. Unexpectedly the system's resistance was lower at 0.23 Ohms compared with the previous resistance of 0.39 Ohms.

Table 5.1: Concentrations of the compounds found in synthetic slag #1 and the NZS iron slag.

Compound	NZS iron slag (wt.%) [10]	Synthetic slag #1 (wt.%) [83]
TiO_2	32.52	33.70
Al_2O_3	18.50	16.50
CaO	16.36	18.40
SiO_2	13.79	16.70
MgO	13.60	14.30
Fe_2O_3	4.30	-
MnO	0.90	-
Na_2O	0.42	-
K_2O	0.15	-
P_2O_5	0.02	-
V_2O_5	-	0.04
SrO	-	0.01
ZrO_2	-	0.01
Nb_2O_5	-	0.01
WO_3	-	0.03

There were two factors which would account for the difference in the systems resistance. The first factor is temperature difference between the two experiments. An interior temperature of 1468°C was obtained in the first experiment and it is likely to have only resulted in partial melting of the NZS iron slag. While at room temperature, and in solid form, the slag is an insulator. If the slag only partially melted then the electrical pathways would have been reduced, resulting in a higher reported resistance. The other factor is varying electrode depths in the melt due to the slag wetting the electrode.

The contact area between the slag and electrode impacts the amount of electrical pathways between the two and therefore impacts the resistance of the system. In both experiments it was aimed to have the electrodes 15 mm deep into the slag. However, the wetting of the NZS iron slag up the electrodes added an uncertainty to the electrodes depth which would have impacted the resistance of the system.

The voltage drop along the cathode was examined and it was found to be significant. The average resistivity of a 1 mm diameter, 600 mm long molybdenum electrode was calculated, and this can be seen in appendix D. The voltage drop across the cathode was found to be 1.5 V at a current of 10A. To reduce this voltage loss, the diameter of the electrode was increased to 6 mm. 6 mm was chosen as it had a low theoretical voltage drop of 0.04V (at a current of 10A) and 6 mm molybdenum rods were on hand as they are also used as the connecting material for the support system. With regards to the slag/electrode interface, it is important to keep the contacted surface area to a minimum as a large contact surface area would provide more electrical pathways, reducing the resistance and therefore increase the current demand.

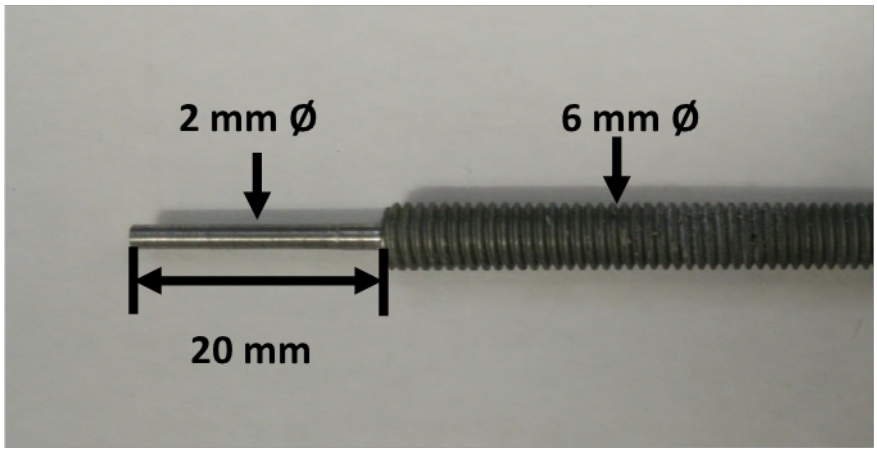

Figure 5.2: The end of the modified molybdenum cathode highlighting the change in diameter.

This lead to the current electrode design. The M6 rod would provide a low resistance pathway for the current up to the slag. A 20 mm section at the end of the 600 mm long molybdenum rod was reduced to a 2 mm diameter, and is shown in Figure 5.2. This kept the electrode/slag surface area to a minimum. 2 mm is the smallest diameter that could practically be machined in the CAPE workshop. The increased size of cathode discounted the use of alumina bore tubes as an electrical insulator between the cathode and flange. Telfon heat shrink was considered as an electrical insulation material due to its melting point of 260°C being higher than the expected flange temperature. When tested, it did not melt but in practice it became so malleable that the act of raising and lowering the electrode would result in the material flaking off. Kapton tape was also considered and found to effectively maintain its structure across multiple runs. Kapton tape is a polymer based, adhesive tape which is an electrical isolator and can withstand temperatures up to 400°C.

The potentiostat used (model 371 Princeton Applied Research) was able to reach a potential of ±2V before it reached its 10A current limit. There was a desire to examine a wider voltage range but this required a potentiostat with a higher current

limit. Due to lack of suitable equipment, focus was shifted to performing constant voltage electrolysis experiments while suitable equipment was sourced. Section 5.2.3 established a set of criteria to be used to source a suitable power supply/potentiostat.

In summary, the start-up experiments showed that the NZS iron and synthetic slag systems possess a high electrical conductivity. The voltage drop along the cathode was examined and shown to be significant (1.5 V at 10A). The cathode's geometry was adjusted to reduce this voltage drop to 0.04V at 10A.

5.2 Baseline Experiment

5.2.1 Aim

The aim of this experiment was to perform a constant voltage electrolysis experiment in order to deposit titanium.

5.2.2 Methodology

The internal support system was configured to allow for an internal temperature of at least 1550°C: high enough to melt synthetic slag #1 [59]. This configuration was previously shown in Figure 4.17b. A 35 mm ID, 80 mm H graphite crucible was 80% filled with 130 grams of powdered synthetic slag # 1.

The system was purged with zero grade argon for 90 minutes at a flow rate of 500 ccm while the furnace was at room temperature. Once the oxygen content, as detected by a Thermox CG-1000 oxygen analyser, was confirmed to be below 100ppm, the flow rate was lowered to 150 ccm for the remainder of the experiment. After the purge sequence, the sample was heated to a furnace temperature of 1630°C, which corresponded to an internal temperature of 1550°C, at a rate of 1°C/min. The sample was held at temperature for 360 minutes before cooling at the same rate.

The graphite crucible acted as the anode and a molybdenum rod, as described in Figure 5.2, was used as the cathode. A 1 mm molybdenum wire served as the reference electrode. The reference electrode was sheathed in a 6.35 mm OD, 1.3 mm ID alumina single bore tube. The top of the bore tube, which housed the reference electrode, was sealed to prevent oxygen from entering the system. While at temperature, the cathode

was lowered until an electrical connection was established, as detected by a voltmeter measuring the resistance between the cathode and anode. At this point the cathode is assumed to be touching the surface of the molten slag. The electrode was lowered an additional 15 mm, its desired depth. Special care was taken to monitor the depth of the cathode to prevent the cathode from touching the bottom of the crucible/anode and short circuiting the system.

A Measurement Computing 1808 data logger was used to record the voltages between the cathode, anode, and reference electrode. A diagram of the electrical connections is shown in Appendix E. A 1 mΩ shunt resistor was used to convert the current into a voltage signal which could be detected by the data logger.

A cell voltage of 2.7 V was then applied and maintained for 150 minutes with the use of a Powertech MP3090 power supply. The material was electrolysed until the system started its cooling sequence. At this point the applied voltage was halted and the cathode was raised from the melt to allow easier examination and SEM sample preparation. Upon cooling, the cathode was freed from the support material, as shown in Figure 5.3, and was cross-sectioned perpendicular to the cathode's longitudinal axis at roughly 5 mm intervals using a high speed diamond saw.

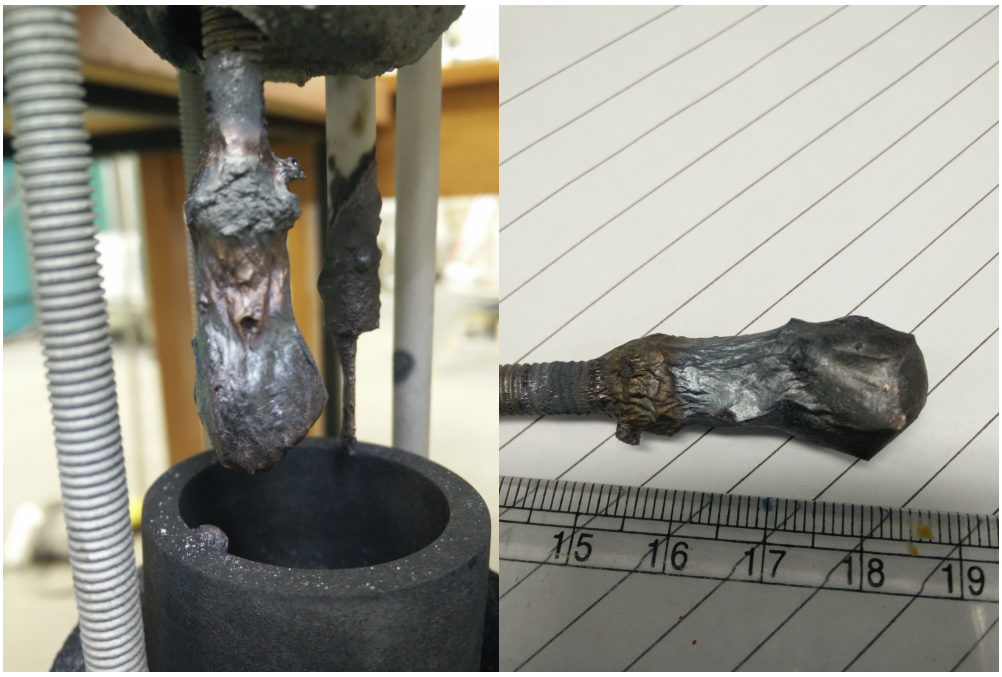

(a) Cathode post firing. (b) Scaled picture of the cathode.

Figure 5.3: The molybdenum cathode post electrolysis experiment with material adhered to it.

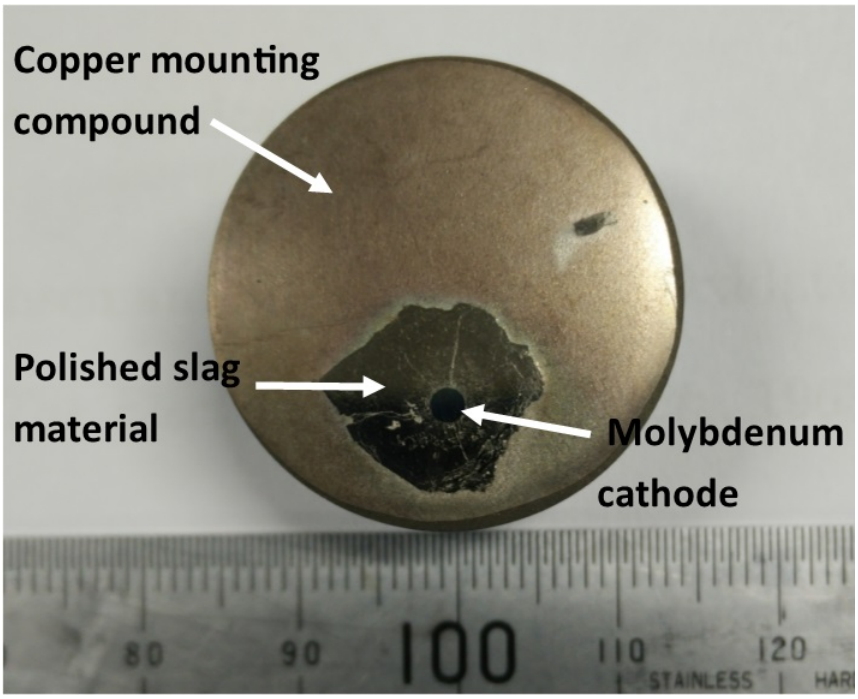

Figure 5.4: A polished slag sample set in a copper mounting compound, prepared for SEM analysis.

In preparation for imaging with a scanning electron microscope (SEM), the samples were set in ProbeMet, a copper based compression mounting compound; polished using progressively finer grade silicon carbide sandpaper (180, 320, 400, 600); and finally polished using a diamond sandpaper with an average particle size of 9 µm. The exterior surface of the sample was carbon coated. A prepared sample can be seen in Figure 5.4. The composition and micro-structure of the produced material was examined using a JEOL IT-300 scanning electron microscope with energy-dispersive x-ray spectroscopy (EDS) and back scatter electron detection (BED-C).

5.2.3 Results and Discussion

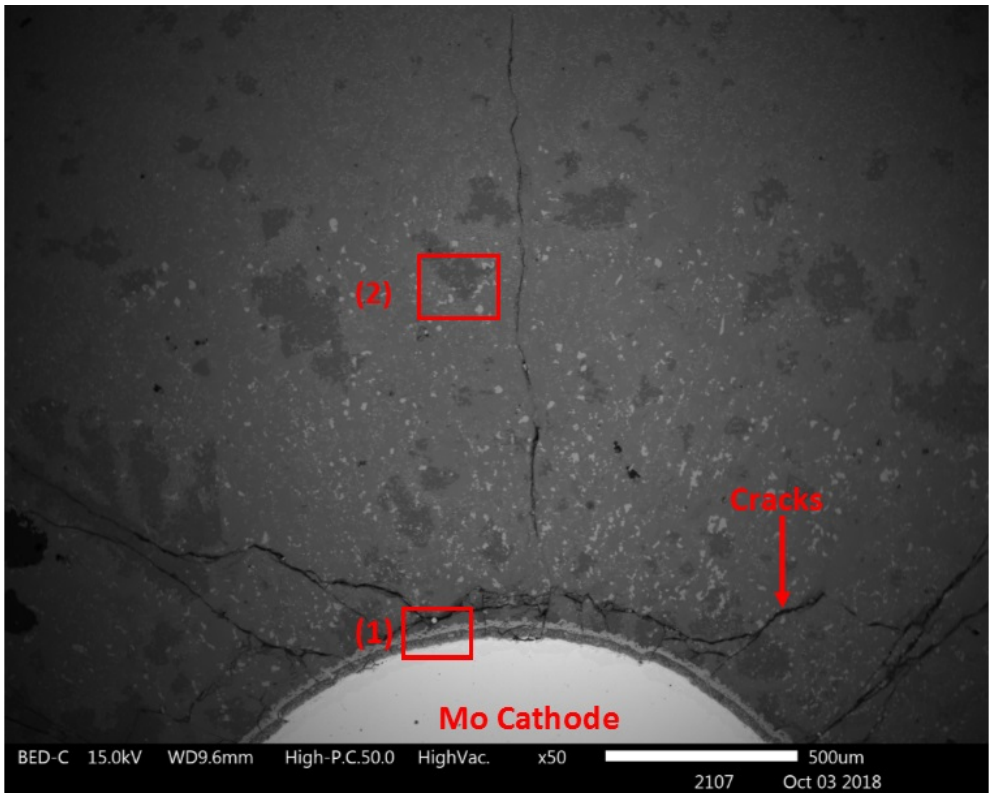

Figure 5.5: Overview picture of the cathode/slag interface highlighting the higher magnification areas (1): Figure 5.6, (2): Figure 5.8.

Figure 5.5 is an overview of the cathode and the surrounding slag. It shows a clear band of produced material around the molybdenum cathode (1) along with a large quantity of lightly coloured, speckled material in the surrounding areas (2). Figure 5.5, 5.6, and 5.8 were captured using BED-C where elements with high atomic weights are lightly coloured and vice versa. To examine these points of interest two higher magnification images were taken at the highlighted areas. Zones (1) and (2) can be seen in Figure 5.6 and 5.8 respectively.

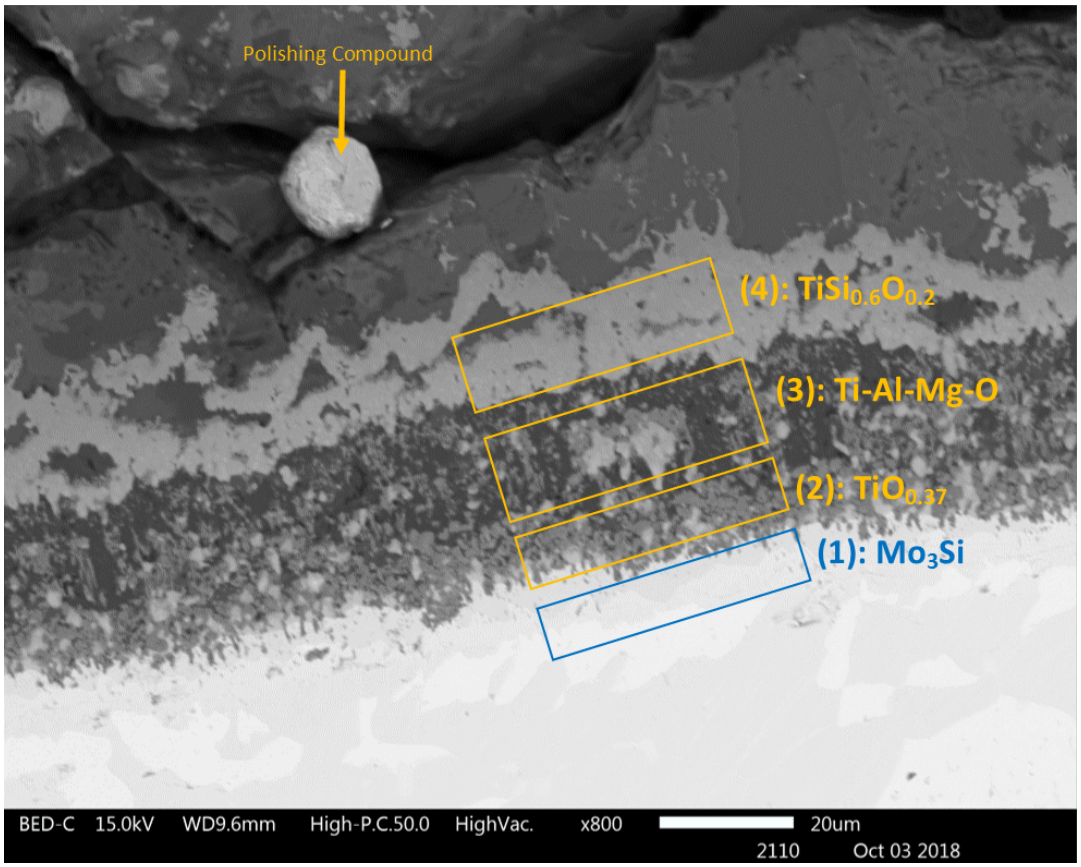

Figure 5.6: Annotated image showing the layered structure of the deposited material on the molybdenum cathode.

Four distinct layers were identified by examining Figure 5.6 and its X-ray counterpart, Figure 5.7. The average atomic % of each layer is shown in Table 5.2 and summarised below. For the remainder of the chapter, all stated % are atomic %.

- Layer 1, which is best seen in Figure 5.7 as the bottom purple band, is 65.0% molybdenum, 21.1% silicon and 9.1% oxygen. The molybdenum and silicon are in an approximate 3:1 ratio respectively (Mo_3Si).

- Layer 2 is comprised of titanium, 67.0%, and oxygen, 24.7%. There are small quantities of molybdenum and silicon with trace amounts of the other slag elements.

- Layer 3 is a slag phase seen in the bulk material which is discussed later.

- Layer 4 is 47.4% titanium, 29.7% silicon and 14.2% oxygen. Molybdenum is also present in small quantities.

Table 5.2: Atomic % of the elements found in the layers of material adhered to the cathode and the approximate ratios of key elements, as shown in Figure 5.6.

	Layers			
Element	(1)	(2)	(3)	(4)
O	9.1	24.7	58.5	14.2
Mg	0.8	0.5	8.3	0.7
Al	0.5	0.4	11.5	0.5
Si	21.1	3.0	4.5	29.7
Ca	0.7	0.7	4.8	0.8
Ti	2.6	67.0	12.3	47.4
Mo	65.0	3.6	0.1	6.8
ratio of key elements	$MoSi_{0.3}O_{0.1}$	$TiO_{0.37}$	TiAlMgO	$TiSi_{0.6}O_{0.2}$

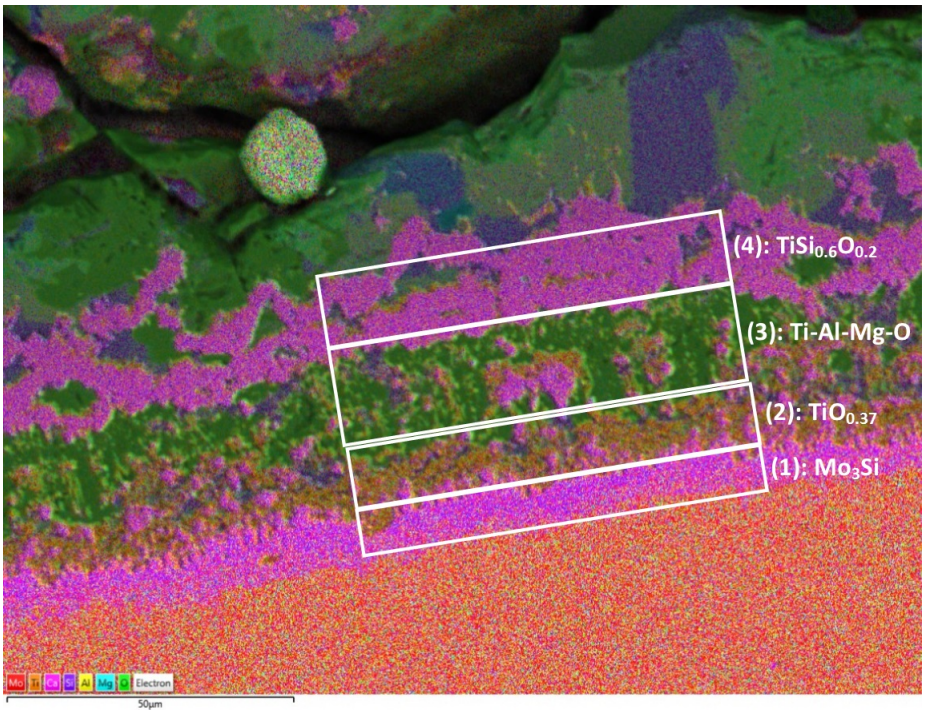

Figure 5.7: X-ray image of the cathode/slag interface showing the distribution of specific elements.

The morphology of the layers suggests that it was once a completely connected layer and it has then been broken up by some mechanism. In layer 3 there are isolated pockets of material from both layers 2 and 4 which are irregular in shape and size. There are two possible explanations for this. As mentioned previously, the applied voltage is discontinued once the furnace had reached the end of its hold time. The slow cooling rate of 1°C/min would have allowed for an extended period of time where the attracted, deposited material could have relaxed and drifted away from the cathode while still a liquid. Alternatively, at the end of the hold sequence the formed layers could have been fractured due to lifting the cathode up from the melt. In the future, this hypothesis could be checked by leaving the cathode in the sample for the entire experiment and applying a voltage until the material has frozen in place.

Comparisons can be made between layers 1 and 2. Due to the extremely similar deposition voltages of titanium and silicon, and the large over-potential applied, it is unlikely that one material would be deposited without the other. Layer 2's high titanium content seems to contradict this as only titanium is present. One theory is that both materials were deposited in similar ratios to that seen in layer 4 but the silicon either dissolved in, or formed a stable structure with, the molybdenum cathode.

Assuming that the oxygen present in layer 1 is associated with the silicon, then the silicon has been reduced going from SiO_2 to $SiO_{0.43}$. The same assumption was applied to the Ti:O ratio in layer 2, where the titanium was reduced from TiO_2 to $TiO_{0.37}$. It is hard to draw conclusions with layer 4 due to not knowing which element, titanium or silicon, is associated with the oxygen. If the oxygen is soley associated with silicon the ratio is $SiO_{0.5}$; and it is $TiO_{0.30}$ if it is only associated with the titanium. If it is split between titanium and silicon the ratio is $MO_{0.19}$ where M is the sum of titanium and silicon. Silicon (29.7%) and titanium (47.4%) are not present in

equal quantities, $Ti_{1.6}Si$, which suggests that the kinetics of titanium's electrochemical reaction is greater than that of silicon.

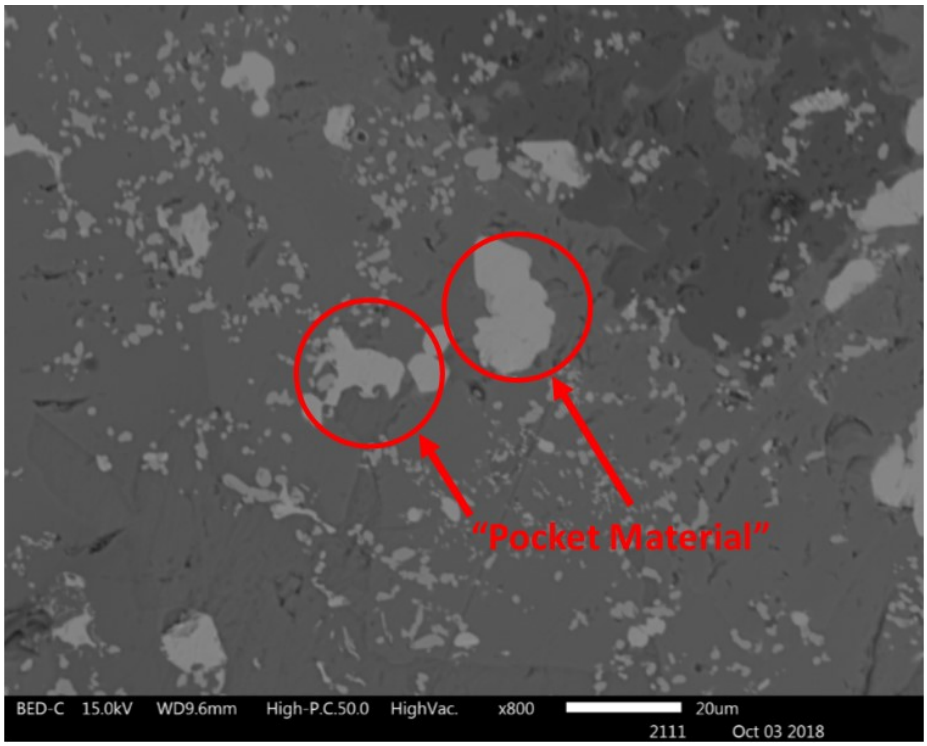

Figure 5.8: Magnified view of the lightly coloured, pockets of partially reduced Ti/Si found near the cathode.

The pockets of lightly coloured material are approximately 56 % titanium, 32% silicon, and 11% oxygen. This material is referred to as the "pocket material" for the rest of the thesis. Two observations about the chemical composition can be made. Firstly, it was noted that there was a greater Ti:Si ratio in this pocket material ($Ti_{1.75}Si$) than there was in layer 4 ($Ti_{1.6}Si$). Secondly, the oxygen-to-metal ratio was calculated and the pocket material's ratio was found to be lower ($MO_{0.13}$) than in layer 4 ($MO_{0.19}$). These two values can be explained by the following notions.

- The pocket material's location in the bulk slag could have allowed for easier transport of titanium into and oxygen out of the pocket material.

- The conditions at the pocket material could have promoted a faster kinetic rate for the titanium reduction reaction.
- The composition of the two materials could have been incorrectly identified due to variation within the material.

It is suggested that this be examined further in future experiments in order to draw solid conclusions.

The distance between the pocket material and the cathode is a matter of interest. The composition suggests that there has been electrochemical reduction but it would be expected for this to occur at the cathode's surface and not in the surrounding areas. The reduced material is concentric with respect to the cathode and does not occur beyond 2500 µm from the outer edge of the cathode. The counter-point to this would be that the reaction occurred spontaneously and was not the result of the applied current.

A control experiment was performed in order to establish if the pocket material was produced through electrochemical means or if it was an expected phase. A 5.0 gram sample, which has the same chemical composition as the last experiment, was prepared in a 14 mm ID, 20 mm H graphite crucible and was heated in the same manner as outlined in the previous methodology. This time the cathode was not lowered into the melt and therefore no current was passed through the sample.

After firing, the sample was examined with a SEM, prepared following the same methodology outlined previously, and no pockets of reduced material were found. Table 5.3 details the phases that were present in both samples. Visually this can be seen in Figure 5.9. The absence of the pocket material in the control experiment results supports the notion that this is indeed an electrochemical product.

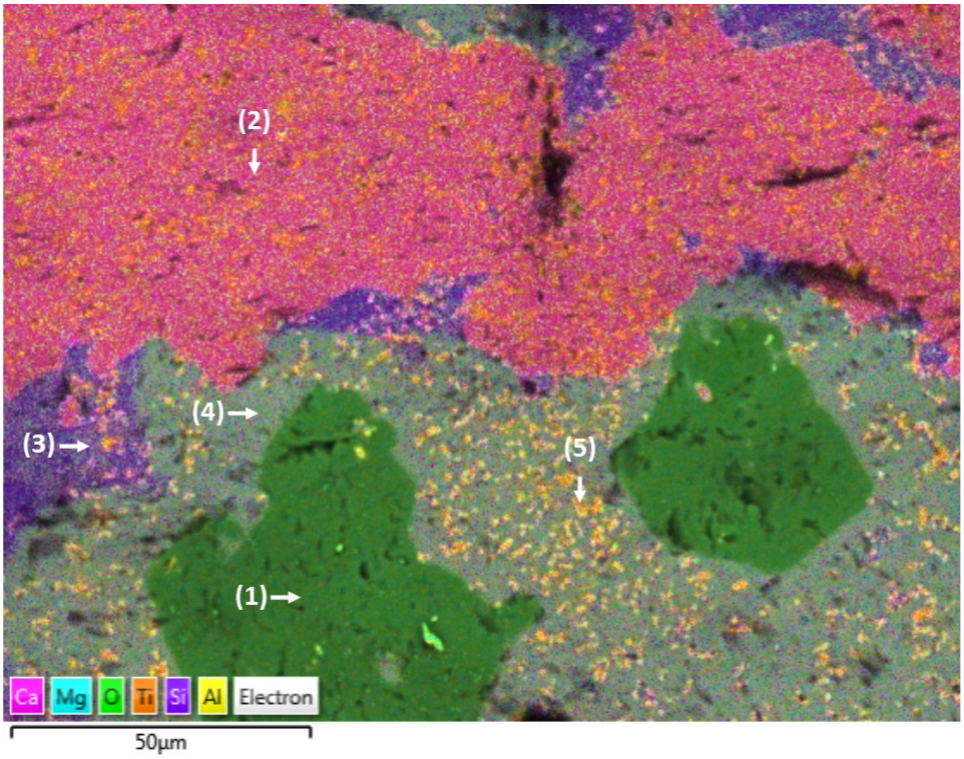

Figure 5.9: X-ray map of slag #1 showing the different phases detailed in Table 5.3.

Table 5.3: Atomic % of the different elements present in the phases of synthetic slag #1, as shown in Figure 5.9 and the approximate ratios of key elements.

Element	Dark green (1)	Pink (2)	Purple (3)	Light green (4)	Yellow (5)
O	52.5	56.1	50.9	50.8	43.9
Mg	16.1	0.0	7.7	11.3	5.0
Al	26.3	0.2	3.4	12.1	5.0
Si	0	0.1	17.7	8.2	3.5
Ca	1.1	21.1	18.0	7.0	3.2
Ti	3.9	22.4	2.2	10.5	39.3
Ratio	Al_2MgO_3	$TiCaO_3$	$CaSiMg_{0.5}O_{2.8}$	$TiAlMgSi_{0.5}Ca_{0.5}O$	TiO

There are two possible theories which would explain the reduced material's location. The first possibility is that dendrites formed, radiating outwards from the molybdenum cathode, towards the graphite crucible and formed an electrical pathway to the pockets of materials. Dendrites are defined as branch like, highly ordered structures which originate from protrusions on the cathode and grow outwards. They are produced due to high current, diffusion-limited systems and only occur past a well defined over-potential [84]. Before dendrites are formed there is an induction period where precursors are formed and become concentrated. Figure 5.10 shows an example of the branching structure of dendrites.

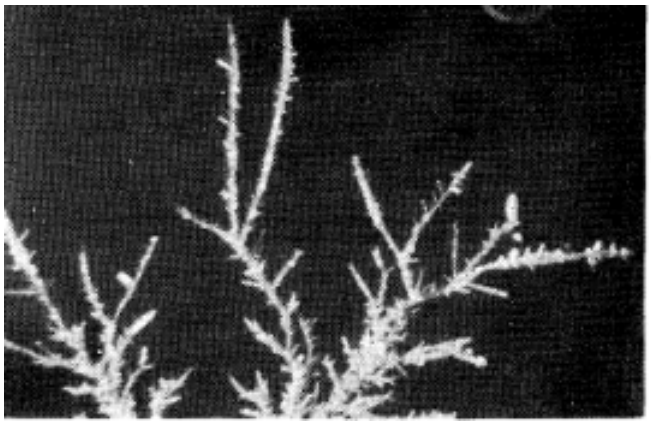

Figure 5.10: An example of the expected structure for electrolytically produced dendrites. Obtained from: [85].

While there are cracks radiating from the cathode going outward, as shown in Figure 5.5, there is not the branching structure connected to the produced material which would be indicative of dendrite formation. It is more likely that these cracks are the result of the high speed diamond saw used to prepare the samples for SEM imaging. The only other likelihood is that the branch-like structures were formed and then dissolved back into the slag upon cooling.

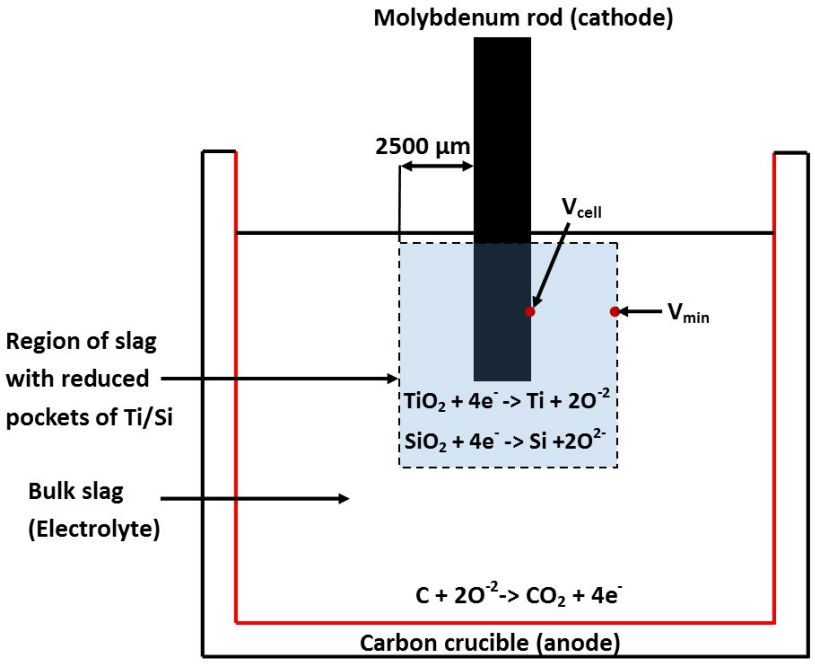

Figure 5.11: An annotated diagram of the electrolytic cell detailing the voltages at the cathode and at the point where no more pocket material is found. These voltages are relative to the anode, which is outlined in red.

The second and more likely theory is that the bulk reduction of titanium and silicon was caused by a large over-potential which, due to the high electrical conductivity of the slag, has allowed for the material around the cathode to be at a sufficient potential for reduction to occur. Figure 5.11 shows an annotated diagram of the electrochemical cell. The light blue region represents the area in which the pockets of $TiSi_{0.57}O_{0.20}$ are found. As the distance from the cathode increases, the potential drops from the cell potential (V_{cell}) to the minimum reduction potential (V_{min}). V_{min} occurs approximately 2500 µm from the cathode surface and past this point, no more reduced material is found. Graphically this is also shown in Figure 5.12.

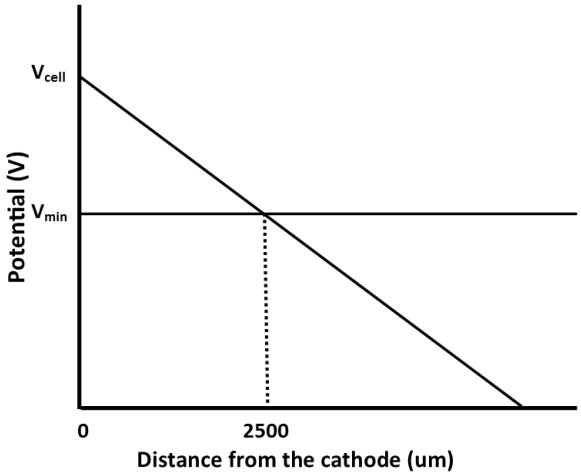

Figure 5.12: Supporting diagram detailing the voltage variation as the distance from the cathode increases.

Current Efficiency

As the name suggests, the current efficiency of a system is a good indication of how effective the electrolytic cell is at reducing material and has been calculated below for that purpose. The volume of reduced material on the cathode and the reduced pocket material was estimated from examining the SEM images. A constant chemical composition was assumed based on the observed values. Appendix A lists all of the assumptions used and the full calculations used to obtain this value. The current efficiency is stated by equation 5.1.

$$e = \frac{\Delta m_{\text{experimental}}}{\Delta m_{\text{theoretical}}} * 100 = 1.1\% \tag{5.1}$$

Where $m_{\text{experimental}}$ is the mass of the reduced material found at the cathode and in the pocket material. $m_{\text{theoretical}}$ is the mass of the material that should be produced based on the Faraday's law of electrolysis. The calculation highlights that most of the electrolytically produced material is found in the bulk slag (0.425 g) and not at the cathode (0.009 g), and that the process is very inefficient. To put this into

perspective, high temperature electrolysis of copper sulfides to copper on a lab scale has a current efficiency of around 5% [34]. The established Hall-Héroult process, used in the production of aluminium, has an efficiency between 85 and 95 % [25]. Lastly the FFC Cambridge process is reported to have a current efficiency of 50% [24]. There are several possible explanations [86] for a low current efficiency which are:

- The loss of products due to sample preparation.
- The occurrence of secondary reactions involving the products.
- Short circuits in the electrical configuration.
- Ohmic heating.
- The re-oxidation of reduced materials after the electrolysis process.

The full electrolytic process is not yet fully understood, so it is possible that the current is being diverted away to an unknown electrochemical reaction. Given the scale of the reaction however, evidence of this unknown reaction should have been seen during the SEM analysis. In this situation, the extremely low current efficiency should be primarily associated with the high electrical conductivity of the electrolyte, which has resulted in a large amount of ohmic heating as the electrons pass through the electrolyte.

As the current efficiency is lower than expected, the electrolysis experiments should be run for longer to produce more material for analysis. If the electrolyte's high electrical conductivity is the primary reason for the low efficiency, its composition could be adjusted to improve the ionic conductivity and reduce the electronic conductivity. There is research that shows an increased ionic conductivity in TiO_2 melts with the inclusion of BaO [47].

Power supply/Potentiostat

In order to perform more insightful and complex electrochemical analytical techniques, a more suitable power supply/potentiostat is required. Due to the extremely high current requirement it is unlikely that a potentiostat would be economically feasible. If a new power supply were to be purchased for this project the following procurement criteria should be used.

- Needs to be able to sweep potentials from 0V to 5V with currents up to 60A.
- Needs to be able to interface with a computer for control and data logging purposes.
- The resolution on the data logging should be able to distinguish on the mV scale.
- The best price in terms of value.
- Compact size for effective lab placement.

Interfacing with a computer is important for data logging purposes and for the control of the voltage. A high degree of control over the potential will allow for linear sweep voltammetry to be carried out a various scan rates.

5.3 Conclusions

The baseline electrolysis experiment showed that there were four unique layers of material on the cathode. The outermost layer showed the partial electrolytic reduction of titanium and silicon (47.4% titanium, 29.7% silicon, and 14.2% oxygen). The deposition of titanium and silicon at different proportions indicated that the kinetics of the titanium reaction were higher than that of the silicon reaction. Pockets of reduced material (56% titanium, 32% silicon, 11% oxygen) were located up to 2500 µm from the cathode due to the high electrical conductivity of the slag. The system's low current efficiency (1.1%) was primarily associated with the energy lost to ohmic heating.

Chapter 6

Conclusions and Recommendations

6.1 Conclusions

A high temperature support system, made from a composite of materials, was designed and produced for a MTI GSL-1700X-100VT-UL vertical tube furnace. The support system allowed for samples to be held in the constant temperature zone and for the introduction of electrodes into the system while maintaining an inert environment. Early design decisions to have an easily adjustable configuration proved to be advantageous when it came to the commissioning of the furnace.

Early experiments resulted in the main alumina tube fracturing which was associated with a high heating/cooling rate, a large thermal gradient in the longitudinal and radial direction, and a lack of external insulation. The heating/cooling rate was reduced to 1°C/min, from 10°C/min when above 1200°C and 5°C/min above 1200°C. External insulation was added to the exposed ends of the alumina tubes in a tiered

manner. To evaluate the effectiveness of the insulating material, the temperature along the exposed ends of the tube was monitored with 10 K type thermocouples. The metric used to evaluate the effectiveness of the insulation was the thermal gradient (°C/mm) which was compared against a reliable manufacturer's specifications for large diameter alumina tubes [80]. A series of experiments was conducted where the temperature was slowly increased and water cooling was introduced when required. The thermal gradient values were within the recommended values, and the insulation configuration was deemed to be appropriate. A basic, qualitative ANSYS thermal model was developed to determine what radiation shield geometric shape contributed the least to the maximum thermal gradient experienced by the alumina tube. Five shapes and a control configuration were considered and it was determined that a half-parabolic shape had the lowest maximum thermal gradient.

It was observed that there was a large difference between the temperature stated by the controller and that of an internal thermocouple; significantly larger than predicted by the manufacturer. The cause of this discrepancy was associated with the position of the radiation shields. As such, a series of experiments were performed which optimised their position. A suitable position of the radiation shields was found which reduced the temperature difference from 190°C to 77°C.

Baseline electrolysis experiments were conducted and SEM analysis showed that there was four distinct layers of material on the cathode. Two layers showed clear signs of reduction. The first was high in titanium (67.0%) with moderate quantities of oxygen (24.7%). The second layer was predominately titanium (47.4%) , silicon (29.7%), and oxygen (14.2%). Pockets of titanium (56.0%), silicon (32.0%), and oxygen (11.0%) were found up to 2500 µm from the cathode in the bulk slag. The pockets of $TiSi_{0.57}O_{0.20}$ were confirmed to be the product of an electrochemical reaction via

a control experiment and did not occur spontaneously. The presence of pockets of reduced of $TiSi_{0.57}O_{0.20}$ in the bulk electrolyte instead of being attached to the cathode was explained by two theories. Firstly, dendrites could have grown from the cathode which would have connected the pockets to the charged cathode. This theory was deemed to be unlikely as no sign of the dendrites were seen during SEM analysis. The second, and favoured, theory was that the low resistance of the molten slag allowed for the deposition potential to be achieved away from the cathode. The current efficiency of the process was determined to be 1.1% which suggested that the conductivity of the slag is predominately electronic, and that energy was being lost due to ohmic heating.

Ultimately, experimental capabilities for an ultra-high temperature electrolytic process was developed. Baseline electrolysis experiments were conducted which showed the partial reduction of titanium and silicon. This thesis provides existing and future University of Canterbury researchers a solid starting point to fully characterise and optimise the electrochemical reduction of titanium oxide to titanium from New Zealand iron-making slag.

6.2 Recommendations

- While the current system allows for high temperature electrolysis experiments, minor usability, and longevity improvements can be made. Currently a 101 mm OD alumina tube is used to contain the sample in a controlled environment. Large diameter alumina tubes are not ideal as they are more expensive, and more sensitive to thermal shock than their smaller diameter counterpart. As per the manufacturer's specifications, the furnace can accept a 101 or 80 mm OD tube.

  The use of an 80 mm OD tube is an improvement but it could theoretically be reduced further, but would require modifications to the internal refractory to prevent too much heat from escaping the hot zone. If a smaller tube were to be used then the support structure would have to be downsized accordingly and this allows the opportunity to fix a minor usability issue. The current position of the vacuum fittings makes tightening them with tools at high temperatures difficult, as access to them is restricted. The current flange design is shown in Figure 6.1a and the proposed solution is to shift a vacuum fitting to the right, as shown in Figure 6.1b.

- The internal temperature difference is currently tolerable, but ideally this should be reduced as much as possible. A smaller difference increases the temperature range at which we can operate, and also reduces the amount of stress experienced by the system. This can be achieved by the continued development of the ANSYS model to try to further optimise the position/shape of the radiation shields. The accuracy of this model could be increased further by including the presence of the remaining support structure.

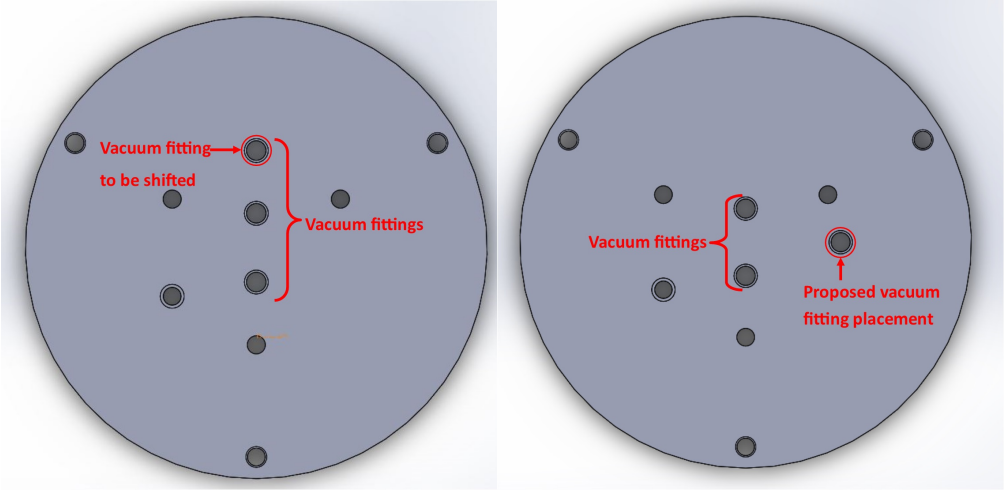

(a) Current flange design. (b) Proposed flange design changes.

Figure 6.1: The position of vacuum fittings in the current and proposed flange design to allow for improved tool access.

- The electrolysis experiments showed that titanium and silicon were deposited together but titanium seemed to be kinetically favoured. Previously it was discussed that the potential at which deposition occurs for titanium and silicon is very similar. The exact potentials at which silicon and titanium are deposited needs to be fully defined as it might be possible to selectively deposit titanium, being the more valuable product. To do this, linear sweep voltammetry should be re-examined with an appropriate power supply/potentiostat. Section 5.2.3 outlined a set of criteria for a suitable power supply.

- The high electrical conductivity of the slag proved to be an issue in terms of the current requirements and contributed to the low current efficiency. The composition of the slag should be examined to try and reduce its electronic conductivity while improving its ionic conductivity. Ionic melt components such as BaO have been included by other research groups for the purpose of increasing the ionic conductivity [47]. A methodology to quantify and distinguish between electrical and ionic conductivity will have to be developed/adopted. There are a

variety of methods which have been used successfully by other research groups [48].

- The material deposited on the cathode had a layered structure which might indicate a multistep reduction process. This notion is supported by literature which has shown that the reduction from TiO_2 to Ti occurs across five steps [87]. An electrolysis experiment should be run under the same conditions as the previous experiment but the slag should be electrolysed for as long as practical, and the cathode should be left in the slag until it has solidified, so as not to disturb the developed layers. The longer electrolysis time should allow for more material to be deposited and make analysis clearer. It might also show the relative size of the layers which might indicate the relative rates of the steps.

Bibliography

(1) Krebs, R. E., *The history and use of our earth's chemical elements: a reference guide*; Greenwood Publishing Group: 2006.

(2) Gázquez, M. J.; Bolívar, J. P.; Garcia-Tenorio, R.; Vaca, F. *Materials Sciences and Applications* **2014**, *5*, 441.

(3) Veiga, C; Davim, J.; Loureiro, A., et al. *Rev. Adv. Mater. Sci* **2012**, *32*, 133–148.

(4) Ag metal miner: titanium market price., [Online]. Available: `https://goo.gl/32yj5h`, Accessed: 2018-10-19.

(5) Ag metal miner: carbon steel market price., [Online]. Available: `https://goo.gl/Gpp3aQ`, Accessed: 2018-10-19.

(6) Boyer, R. *Jom* **2010**, *62*, 21–24.

(7) Hanson, B. *Materials & Design* **1986**, *7*, 301–307.

(8) Subramanyam, R. B. *Bulletin of Materials Science* **1993**, *16*, 433–451.

(9) Sommer, D.-I. K.; Friedrich, B; Recycling, M. In *Proceedings of EMC*, 2005, p 1.

(10) Mclaughlin, T. Characterisation of Iron Sand and Iron Slag from the New Zealand Steel Process., Bachelors of engineering with honours, University of Canterbury, 2016.

(11) *Use of melter slag as aggregate in open-graded emulsion mixes*; tech. rep.; OPUS international consultants limited, 1998.

(12) Allanore, A. *Journal of The Electrochemical Society* **2015**, *162*, E13–E22.

(13) Sibum, H.; Güther, V.; Roidl, O.; Habashi, F.; Wolf, H. U., *Titanium, Titanium Alloys, and Titanium Compounds*; American Cancer Society: 2000.

(14) Turner, P. C.; Hartman, A. D.; Hansen, J. S.; Gerdemann, S. J. *Low cost titanium–myth or reality*; tech. rep.; Albany Research Center (ARC), Albany, OR, 2001.

(15) Kroll and Armstrong process diagrams., [Online]. Available: `https://goo.gl/MnN1Su`, Essential Chemical Industry, 2018.

(16) Wilhelm, K. Method for manufacturing titanium and alloys thereof., US Patent 2,205,854, 1940.

(17) Gerdemann, S. J. *Advanced materials & processes* **2001**, *159*.

(18) Wartman, F.; Baker, D. H.; Nettle, J.; Homme, V. *Journal of the Electrochemical Society* **1954**, *101*, 507–513.

(19) Kraft, E., *Summary of emerging titanium cost reduction technologies*; EHK Technologies: 2004.

(20) Chen, W.; Yamamoto, Y.; Peter, W. H.; Gorti, S. B.; Sabau, A. S.; Clark, M. B.; Nunn, S. D.; Kiggans, J.; Blue, C. A.; Williams, J., et al. *Powder technology* **2011**, *214*, 194–199.

(21) Anderson, R; Benish, A; Jacobsen, L; Ernst, W; Kogut, D In *16th Annual AeroMat Conference, Orlando, FL*, 2005.

(22) Chen, G. Z.; Fray, D. J.; Farthing, T. W. *Nature* **2000**, *407*, 361.

(23) Metalysis information page., [Online]. Available: `https://goo.gl/BhwUZA`, Accessed: 2017-09-04.

(24) Mohandas, K.; Fray, D. *Trans. Indian Inst. Met* **2004**, *57*, 579–592.

(25) Haupin, W. Electrochemistry of the Hall-Heroult process for aluminum smelting., 1983.

(26) Suzuki, R. O.; Ono, K.; Teranuma, K. *Metallurgical and Materials Transactions B* **2003**, *34*, 287–295.

(27) Landmarks, A. C.S.N.H. C. Hall Process: Production and Commercialization of Aluminum., [Online]. Available: https://goo.gl/iKgNbw, 2018.

(28) Gaskell, D. R., *Introduction to metallurgical thermodynamics*, 1981.

(29) Crow, D. R., *Principles and applications of electrochemistry*; Routledge: 2017.

(30) Linear Sweep and Cyclic Voltametry: The Principles., [Online]. Available: https://goo.gl/dovWE5, Accessed: 2018-11-21.

(31) Chemistry libretexts: linear sweep voltammetry., [Online]. Available: https://goo.gl/7SHUdt, Accessed: 2018-11-21.

(32) Scholz, F. et al., *Electroanalytical methods*; Springer: 2010; Vol. 1.

(33) Inzelt, G.; Lewenstam, A.; Scholz, F., *Handbook of reference electrodes*; Springer: 2013.

(34) Sokhanvaran, S.; Lee, S.-K.; Lambotte, G.; Allanore, A. *Journal of The Electrochemical Society* **2016**, *163*, D115–D120.

(35) Kasem, B. K. K.; Jones, S. *Platinum Metals Review* **2008**, *52*, 100–106.

(36) Wiencke, J.; Lavelaine, H.; Panteix, P.-J.; Petitjean, C.; Rapin, C. *Journal of Applied Electrochemistry* **2018**, *48*, 115–126.

(37) Kim, H.; Paramore, J.; Allanore, A.; Sadoway, D. R. *Journal of The Electrochemical Society* **2011**, *158*, E101–E105.

(38) Allanore, A.; Yin, L.; Sadoway, D. R. *Nature* **2013**, *497*, 353.

(39) Wang, D. In *3rd reactive metals workshop, MIT, Cambridge, MA*, 2007.

(40) Vai, A.; Yurko, J.; Wang, D.; Sadoway, D. *Minerals, Metals and Materials Society/AIME, 420 Commonwealth Dr., P. O. Box 430 Warrendale PA 15086 USA.[np]. 14-18 Feb* **2010**.

(41) Sahu, S. K.; Chmielowiec, B.; Allanore, A. *Electrochimica Acta* **2017**, *243*, 382–389.

(42) Yan, B. C. K. Electrolysis of Titanium Oxide to Titanium in Molten Cryolite Salt., Master of Applied Science, University of Toronto, 2016.

(43) Allanore, A. *Electrochimica Acta* **2013**, *110*, 587–592.

(44) Mills, K.; Yuan, L; Jones, R. *Journal of the Southern African Institute of Mining and Metallurgy* **2011**, *111*, 649–658.

(45) Brauer, D. S.; Karpukhina, N.; Law, R. V.; Hill, R. G. *Journal of Non-Crystalline Solids* **2010**, *356*, 2626–2633.

(46) Gaune-Escard, M., *Molten salts: from fundamentals to applications*; Springer Science & Business Media: 2012; Vol. 52.

(47) Fried, N. A.; Rhoads, K. G.; Sadoway, D. R. *Electrochimica acta* **2001**, *46*, 3351–3358.

(48) Schiefelbein, S. L. A New Technique to Measure the Electrical Properties of Molten Oxides., Ph.D. Thesis, Massachusetts Institute of Technology, 1996.

(49) Huggins, R. A. *Ionics* **2002**, *8*, 300–313.

(50) Fried, N. A. Electrical properties of binary solutions of molten titanium dioxide-barium oxide., Ph.D. Thesis, Massachusetts Institute of Technology, 1996.

(51) Sante Furnace: split vertical tube furnace image., [Online]. Available: `https://goo.gl/84KMyT`, Accessed: 2018-11-24.

(52) Barron, R. F.; Barron, B. R., *Design for thermal stresses*; John Wiley & Sons: 2011.

(53) Hasselman, D. *Materials Science and Engineering* **1985**, *71*, 251–264.

(54) Auerkari, P., *Mechanical and physical properties of engineering alumina ceramics*; Technical Research Centre of Finland Espoo: 1996.

(55) Perry, J. H., *Chemical engineers' handbook*; ACS Publications: 1950.

(56) ANSYS fluent 12.0 user's guide.; ANSYS, INC., 2009.

(57) MTI GSL - 1700x-100VT-UL furnace picture., [Online]. Available: `https://goo.gl/ZHZp3E`, Accessed: 2018-11-21.

(58) Nichols, S. Design and Build an Ultra High Temperature Electrolytic Cell., Summer research project, University of Canterbury, 2017.

(59) Weaver, N. Thermodynamic Characterisation of Iron Smelter Slag., Unpublished Master's of engineering thesis, University of Canterbury, New Zealand, 2018.

(60) Ap mex: platinum market price., [Online]. Available: https://goo.gl/ULNptJ, Accessed: 2018-10-19.

(61) Matweb: platinum tensile strength., [Online]. Available: https://goo.gl/tpvLXj, Accessed: 2018-11-22.

(62) YSZ wholesale price., [Online]. Available: https://goo.gl/7BcDWJ, Accessed: 2018-10-19.

(63) Noguchi, K.; Fujita, M.; Masaki, T.; Mizushina, M. *Journal of the American Ceramic Society* **1989**, *72*, 1305–1307.

(64) Edition, M. H. N. *American Society for Metals* **1979**.

(65) Metalary: tungsten market price., [Online]. Available: https://goo.gl/H3M8ya, Accessed: 2018-10-19.

(66) Focus economics: alumina market price., [Online]. Available: https://goo.gl/8FpxFs, Accessed: 2018-10-19.

(67) Matweb: alumina tensile strength., [Online]. Available: https://goo.gl/Pc9Ada, Accessed: 2018-11-22.

(68) London metal exchange: molybdenum market price., [Online]. Available: https://goo.gl/Tj39tm, Accessed: 2018-10-19.

(69) Focus graphite: graphite market price., [Online]. Available: https://goo.gl/2PSMZS, Accessed: 2018-10-19.

(70) Poco graphite: graphite tensile strength., [Online]. Available: https://goo.gl/UNB4PK, Accessed: 2018-11-22.

(71) Ag metal miner: 304 stainless steel market price., [Online]. Available: https://goo.gl/M7bMyw, Accessed: 2018-10-19.

(72) Matweb: 304 stainless steel tensile strength., [Online]. Available: https://goo.gl/Qo9AbP, Accessed: 2018-11-22.

(73) Wareham, C., Quotation, CoorsTek, 2017.

(74) Gambale, K., Quotation, Extreme Bolts and Fasteners, 2017.

(75) Mitchell, G., Personal communication, University of Canterbury, Workshop Technician, 2017.

(76) Gulbransen, E.; Andrew, K.; Brassart, F. *Journal of the Electrochemical Society* **1963**, *110*, 952–959.

(77) Graphite Store: e-store prices for graphite rods., [Online]. Available: `https://goo.gl/6Lu6WF`, Accessed: 2017-05-06.

(78) 1700°C Vertical Vaccuum Tube Furnace Operation Manual.; MTI Corporation, 2018.

(79) Brown, I., Personal communication, Callaghan Innovation, 2017.

(80) General considerations for the use of ceramic furnace tubes.; McDanel Advanced Ceramic Technologies, 2015.

(81) Liu, P., Personal communication, MTI Corporation, 2017.

(82) Emissivity of common materials., [Online]. Available: `https://goo.gl/3MsEbU`, Accessed: 2018-12-02, Omega.

(83) Jia, Y. XRF analysis of prepared synthetic slag samples., Callaghan Innovation, 2017.

(84) Popov, K. I.; Živković, P. M.; Nikolić, N. D. *Zaštita materijala* **2016**, *57*, 55–62.

(85) Horiuchi, T.; Kammel, R. *Japanese Journal of Applied Physics* **1972**, *11*, 6.

(86) Creighton, H. J. M.; Koehler, W. A., et al., *Principles and applications of electrochemistry*; J. Wiley & sons, inc.: 1943.

(87) Meng, F.; Lu, H. *ISRN Metallurgy* **2013**, *2013*.

(88) Revised Type B thermocouple reference tables., Accessed: 2018-12-02; Omega.

(89) Desai, P.; Chu, T.; James, H. M.; Ho, C. *Journal of physical and chemical reference data* **1984**, *13*, 1069–1096.

(90) Duffy, J. *Journal of chemical education* **1996**, *73*, 1138.

(91) Shu, Q.; Hu, X.; Yan, B.; Zhang, J.; Chou, K.-C. *Ironmaking & Steelmaking* **2010**, *37*, 387–391.

(92) Zhang, G.-H.; Chou, K.-C. *Journal of Iron and Steel Research, International* **2010**, *17*, 1–4.

Appendix A

Current Efficiency Calculation

	Density, p [g/cm^3]	Molar mass, M [g/mol]
Ti	4.51	47.87
Si	2.32	28.09

Cathode radius, r [mm]	2.00
Height of electrolyzed material, h [mm]	20.00
Faradays constant [C/mol]	96485.33
Amp seconds, It [A.s]	364129.77

Assumptions

- **The material is fully reduced and is composed of titanium and silicon only.**
- **The "pocket material" constitutes 20% of the bulk slag material from the surface of the cathode up to 2500 µm into the bulk material. This was based on observations of the SEM images**
- **The ring reduced material around the cathode's surface has a uniform thickness of 20 um.**

$$It = \sum I * \frac{1}{f}$$

Determined from the experiments logged current values. Where f is the recording frequency, and I is the current.

	Cathode material	Pocket material
Band thickness, t [mm]	0.02	2.50
Area %	1.00	0.20
Ti_x (at.%)	0.64	0.62
Si_y (at.%)	0.36	0.39
Si_yTi_x density, p [g/cm3]	3.71	3.66
Si_yTi_x molar mass, M [g/mol]	40.67	40.25
Material area, A [mm^2]	0.13	5.72
Material volume, V [cm^3]	0.003	0.11
Material mass, m [g]	0.009	0.43

Values obtained from examining the SEM analysis

$$p_{TiSi} = Ti(at.\%) * p_{Ti} + Si(at.\%) * p_{Si}$$

$$M_{TiSi} = Ti(at.\%) * M_{Ti} + Si(at.\%) * M_{Si}$$

$$A_{material} = \left(\pi(r_{cathode} + t)^2 - \pi r_{cathode}^2\right) * \%$$

$$V_{material} = A_{material} * h$$

$$m_{material} = \frac{(V_{material} * p_{SiTi})}{M_{SiTi}}$$

$m_{experiment}$ [g]	0.4
M_{theory} [g]	38.4
Current efficiency	**1.1 %**

$$m_{experiment} = m_{cathode\,material} + m_{pocket\,material}$$

$$m_{theory} = \frac{M * I * t}{nF}$$

$$Current\ efficency = \frac{m_{experiment}}{m_{theory}} * 100$$

Figure A.1: Calculations used to determine the current efficiency of the electrolytic process detailed in section 5.2.

Appendix B

Flange Sealing Methods

The flange design relied on during the 1200 and 1400°C experiments, as described in section 4.2.3, used silicone o-rings which were compressed to form a gas seal. As the temperature increased it surpassed the maximum service temperature of silicone (315°C [78]) which resulted in the gas seal being ineffective due to the reduced mechanical properties of silicone. There were several potential modifications to the flange sealing method which address the rising temperatures and are listed below:

- Metal O-rings
- Silicone O-rings with water cooling
- Face sealing method
- Sealing with high temperature glues

The most immediate solution to the problem is to obtain an O-ring material which can withstand a higher temperature and still seal the system. In terms of plastics there are very few that can outperform silicone. PTFE and PEEK have a slightly higher melting point at 326 and 343°C respectively but these are only marginal gains.

Metal O-rings are a possibility but the higher strength of the metals requires more force to create the seal which might in turn damage the alumina tube.
An alternative method is to hold the inner faces of the flange against the edges of the alumina tube which might create a sufficient seal. This was tested by configuring the system and flowing zero grade argon across through the tube and recording the oxygen content of the outlet stream. After flowing 500 ccm of argon for two hours the reported O_2 levels had not changed from ambient conditions and as such it was deemed that there was an insufficient seal. This method could be improved via the use of high temperature adhesives to fill any gaps. This method is not ideal as the flange has to be removed after each run to recover the sample and the removal of the adhesive would be difficult.

The last option is to continue to use the silicone O-rings but use water cooled flanges. This is a preferred solution in terms of usability but the effect it has on the thermal gradient needs to be determined through low temperature experiments before higher temperatures can be achieved. This has been explored in section 4.2.3.

Appendix C

Type B Thermocouple Voltage-Temperature Table

Thermoelectric Voltage in Millivolts

°C	0	1	2	3	4	5	6	7	8	9	10	°C
1200	6.788	6.797	6.807	6.818	6.828	6.838	6.849	6.859	6.869	6.880	6.890	1200
1210	6.890	6.901	6.911	6.922	6.932	6.942	6.953	6.963	6.974	6.984	6.995	1210
1220	6.995	7.005	7.016	7.026	7.037	7.047	7.058	7.068	7.079	7.089	7.100	1220
1230	7.100	7.110	7.121	7.131	7.142	7.152	7.163	7.173	7.184	7.194	7.205	1230
1240	7.205	7.216	7.226	7.237	7.247	7.258	7.269	7.279	7.290	7.300	7.311	1240
1250	7.311	7.322	7.332	7.343	7.353	7.364	7.375	7.385	7.396	7.407	7.417	1250
1260	7.417	7.428	7.439	7.449	7.460	7.471	7.482	7.492	7.503	7.514	7.524	1260
1270	7.524	7.535	7.546	7.557	7.567	7.578	7.589	7.600	7.610	7.621	7.632	1270
1280	7.632	7.643	7.653	7.664	7.675	7.686	7.697	7.707	7.718	7.729	7.740	1280
1290	7.740	7.751	7.761	7.772	7.783	7.794	7.805	7.816	7.827	7.837	7.848	1290
1300	7.848	7.859	7.870	7.881	7.892	7.903	7.914	7.924	7.935	7.946	7.957	1300
1310	7.957	7.968	7.979	7.990	8.001	8.012	8.023	8.034	8.045	8.056	8.066	1310
1320	8.066	8.077	8.088	8.099	8.110	8.121	8.132	8.143	8.154	8.165	8.176	1320
1330	8.176	8.187	8.198	8.209	8.220	8.231	8.242	8.253	8.264	8.275	8.286	1330
1340	8.286	8.298	8.309	8.320	8.331	8.342	8.353	8.364	8.375	8.386	8.397	1340
1350	8.397	8.408	8.419	8.430	8.441	8.453	8.464	8.475	8.486	8.497	8.508	1350
1360	8.508	8.519	8.530	8.542	8.553	8.564	8.575	8.586	8.597	8.608	8.620	1360
1370	8.620	8.631	8.642	8.653	8.664	8.675	8.687	8.698	8.709	8.720	8.731	1370
1380	8.731	8.743	8.754	8.765	8.776	8.787	8.799	8.810	8.821	8.832	8.844	1380
1390	8.844	8.855	8.866	8.877	8.889	8.900	8.911	8.922	8.934	8.945	8.956	1390
1400	8.956	8.967	8.979	8.990	9.001	9.013	9.024	9.035	9.047	9.058	9.069	1400
1410	9.069	9.080	9.092	9.103	9.114	9.126	9.137	9.148	9.160	9.171	9.182	1410
1420	9.182	9.194	9.205	9.216	9.228	9.239	9.251	9.262	9.273	9.285	9.296	1420
1430	9.296	9.307	9.319	9.330	9.342	9.353	9.364	9.376	9.387	9.398	9.410	1430
1440	9.410	9.421	9.433	9.444	9.456	9.467	9.478	9.490	9.501	9.513	9.524	1440

°C	0	1	2	3	4	5	6	7	8	9	10	°C
1550	10.679	10.691	10.703	10.714	10.726	10.738	10.749	10.761	10.773	10.784	10.796	1550
1560	10.796	10.808	10.819	10.831	10.843	10.854	10.866	10.877	10.889	10.901	10.913	1560
1570	10.913	10.924	10.936	10.948	10.959	10.971	10.983	10.994	11.006	11.018	11.029	1570
1580	11.029	11.041	11.053	11.064	11.076	11.088	11.099	11.111	11.123	11.134	11.146	1580
1590	11.146	11.158	11.169	11.181	11.193	11.205	11.216	11.228	11.240	11.251	11.263	1590
1600	11.263	11.275	11.286	11.298	11.310	11.321	11.333	11.345	11.357	11.368	11.380	1600
1610	11.380	11.392	11.403	11.415	11.427	11.438	11.450	11.462	11.474	11.485	11.497	1610
1620	11.497	11.509	11.520	11.532	11.544	11.555	11.567	11.579	11.591	11.602	11.614	1620
1630	11.614	11.626	11.637	11.649	11.661	11.673	11.684	11.696	11.708	11.719	11.731	1630
1640	11.731	11.743	11.754	11.766	11.778	11.790	11.801	11.813	11.825	11.836	11.848	1640
1650	11.848	11.860	11.871	11.883	11.895	11.907	11.918	11.930	11.942	11.953	11.965	1650
1660	11.965	11.977	11.988	12.000	12.012	12.024	12.035	12.047	12.059	12.070	12.082	1660
1670	12.082	12.094	12.105	12.117	12.129	12.141	12.152	12.164	12.176	12.187	12.199	1670
1680	12.199	12.211	12.222	12.234	12.246	12.257	12.269	12.281	12.292	12.304	12.316	1680
1690	12.316	12.327	12.339	12.351	12.363	12.374	12.386	12.398	12.409	12.421	12.433	1690
1700	12.433	12.444	12.456	12.468	12.479	12.491	12.503	12.514	12.526	12.538	12.549	1700
1710	12.549	12.561	12.572	12.584	12.596	12.607	12.619	12.631	12.642	12.654	12.666	1710
1720	12.666	12.677	12.689	12.701	12.712	12.724	12.736	12.747	12.759	12.770	12.782	1720
1730	12.782	12.794	12.805	12.817	12.829	12.840	12.852	12.863	12.875	12.887	12.898	1730
1740	12.898	12.910	12.921	12.933	12.945	12.956	12.968	12.980	12.991	13.003	13.014	1740
1750	13.014	13.026	13.037	13.049	13.061	13.072	13.084	13.095	13.107	13.119	13.130	1750
1760	13.130	13.142	13.153	13.165	13.176	13.188	13.200	13.211	13.223	13.234	13.246	1760
1770	13.246	13.257	13.269	13.280	13.292	13.304	13.315	13.327	13.338	13.350	13.361	1770
1780	13.361	13.373	13.384	13.396	13.407	13.419	13.430	13.442	13.453	13.465	13.476	1780
1790	13.476	13.488	13.499	13.511	13.522	13.534	13.545	13.557	13.568	13.580	13.591	1790

Figure C.1: Literature values for the voltages produced by type b thermocouples across a range of temperatures [88].

Appendix D

Electrode Voltage Loss Calculations

Assumptions

- The temperature along the cylindrical electrode is evenly distributed
- The total resistivity of the electrode is an average based on the resistivity values along the electrode

Furnace temperature	1773	K
Electrode length, *l*	50	cm
Current, I	10	A

	1 mm electrode	6 mm electrode
Cross-sectional area, A [cm^2]	0.0079	0.2827
Resistance, R [ohm]	0.16	0.0046
Voltage loss, V [V]	1.6	0.046

$$A = \pi r^2$$

$$R = p\frac{l}{A}$$

$$V = IR$$

Temperature (K)	Molybdenum Resistivity, p
300	5.52
400	8.02
500	10.57
600	13.17
700	15.81
800	18.50
900	21.23
1000	24.00
1100	26.81
1200	29.66
1300	32.54
1400	35.46
1500	38.42
1600	41.41
1700	44.43
1800	47.48
Average	25.81

Figure D.1: Estimations of the voltage drop across molybdenum electrodes based on literature resistivity values [89].

Appendix E

Data Logger Connections

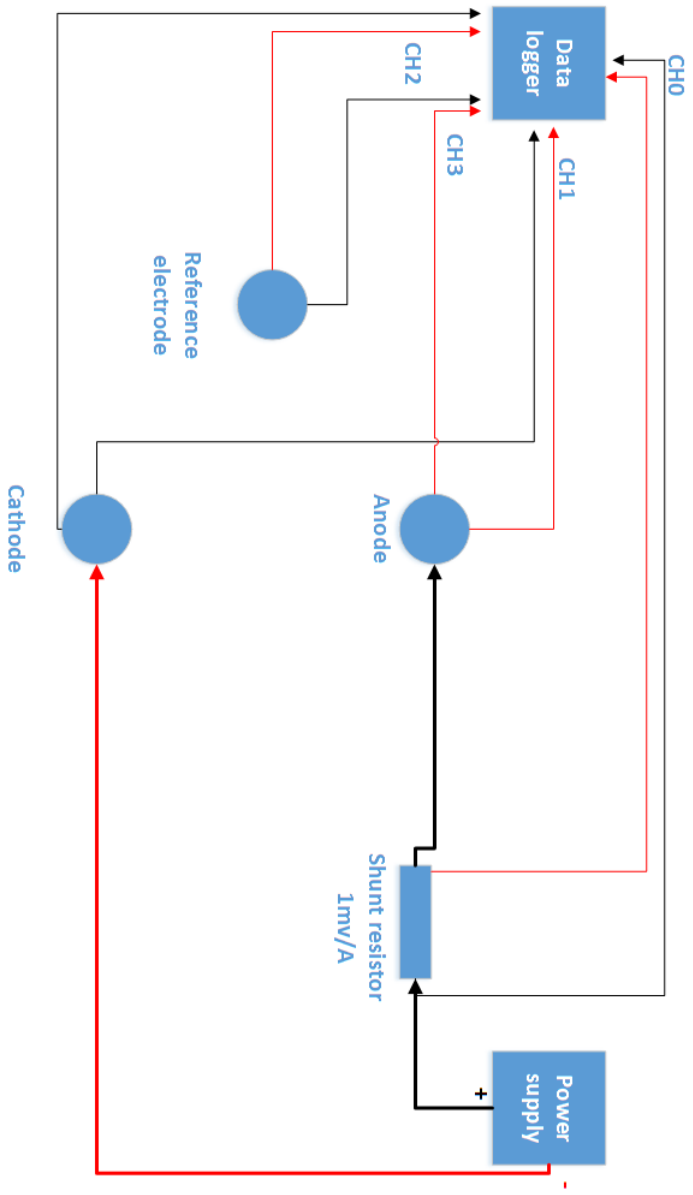

Figure E.1: The electrical connections of the power supply and data logger used in the experiment described in section 5.2.

Appendix F

Half Cell Reduction Potential Calculations

T (K)	G (J)	E (V)	G (J)	E (V)	G (J)	E (V)	G (J)	E (V)	G (J)	E (V)	G (J)	E (V)	G (J)	E (V)	G (J)	E (V)
298	-394350.32	-1.02	-240960.10	-1.25	-	-	-	-	-858446.00	-2.22	-	-	-	-	-	-
350	-394394.00	-1.02	-237707.50	-1.23	-	-	-	-	-849450.00	-2.20	-	-	-	-	-	-
400	-394436.00	-1.02	-234580.00	-1.22	-	-	-	-	-840800.00	-2.18	-	-	-	-	-	-
450	-394478.00	-1.02	-231452.50	-1.20	-	-	-	-	-832150.00	-2.16	-	-	-	-	-	-
500	-394520.00	-1.02	-228325.00	-1.18	-	-	-	-	-823500.00	-2.13	-	-	-	-	-	-
550	-394562.00	-1.02	-225197.50	-1.17	-	-	-	-	-814850.00	-2.11	-	-	-	-	-	-
600	-394604.00	-1.02	-222070.00	-1.15	-	-	-	-	-806200.00	-2.09	-	-	-	-	-	-
650	-394646.00	-1.02	-218942.50	-1.13	-	-	-	-	-797550.00	-2.07	-	-	-	-	-	-
700	-394688.00	-1.02	-215815.00	-1.12	-	-	-	-	-788900.00	-2.04	-	-	-	-	-	-
750	-394730.00	-1.02	-212687.50	-1.10	-	-	-	-	-780250.00	-2.02	-	-	-	-	-	-
800	-394772.00	-1.02	-209560.00	-1.09	-	-	-	-	-771600.00	-2.00	-	-	-	-	-	-
850	-394814.00	-1.02	-206432.50	-1.07	-	-	-	-	-762950.00	-1.98	-	-	-	-	-	-
900	-394856.00	-1.02	-203305.00	-1.05	-	-	-	-	-754300.00	-1.95	-	-	-	-	-	-
950	-394898.00	-1.02	-200177.50	-1.04	-	-	-	-	-745650.00	-1.93	-	-	-	-	-	-
1000	-394940.00	-1.02	-197050.00	-1.02	-	-	-	-	-737000.00	-1.91	-	-	-	-	-	-
1050	-394982.00	-1.02	-193922.50	-1.00	-	-	-	-	-728350.00	-1.89	-	-	-	-	-	-
1100	-395024.00	-1.02	-190795.00	-0.99	-	-	-	-	-719700.00	-1.86	-	-	-	-	-	-
1150	-395066.00	-1.02	-187667.50	-0.97	-	-	-	-	-711050.00	-1.84	-	-	-	-	-	-
1200	-395108.00	-1.02	-184540.00	-0.96	-	-	-	-	-702400.00	-1.82	-	-	-	-	-	-
1250	-395150.00	-1.02	-181412.50	-0.94	-	-	-	-	-693750.00	-1.80	-	-	-	-	-	-
1300	-395192.00	-1.02	-178285.00	-0.92	-	-	-	-	-685100.00	-1.78	-	-	-	-	-	-
1350	-395234.00	-1.02	-175157.50	-0.91	-	-	-	-	-676450.00	-1.75	-	-	-	-	-	-
1400	-395276.00	-1.02	-172030.00	-0.89	-	-	-	-	-667800.00	-1.73	-	-	-	-	-	-
1450	-395318.00	-1.02	-168902.50	-0.88	-	-	-	-	-659150.00	-1.71	-	-	-	-	-	-
1500	-395360.00	-1.02	-165775.00	-0.86	-	-	-	-	-650500.00	-1.69	-	-	-	-	-	-
1550	-395402.00	-1.02	-162647.50	-0.84	-	-	-	-	-641850.00	-1.66	-	-	-	-	-	-
1600	-395444.00	-1.02	-159520.00	-0.83	-	-	-	-	-633200.00	-1.64	-	-	-	-	-	-
1650	-395486.00	-1.02	-156392.50	-0.81	-	-	-	-	-624550.00	-1.62	-	-	-	-	-	-
1700	-395528.00	-1.02	-	-	-	-	-	-	-615900.00	-1.60	-1132000.00	-1.96	-390729.92	-2.02	-	-
1750	-395570.00	-1.02	-	-	-	-	-606200.00	-1.57	-607250.00	-1.57	-1116000.00	-1.93	-380554.17	-1.97	-908125.00	-2.35
1800	-395612.00	-1.03	-	-	-151142.00	-0.78	-	-	-598600.00	-1.55	-1100000.00	-1.90	-370397.55	-1.92	-888620.00	-2.30
1850	-395654.00	-1.03	-	-	-148876.50	-0.77	-	-	-589950.00	-1.53	-	-	-360259.53	-1.87	-869115.00	-2.25
1900	-395696.00	-1.03	-	-	-146611.00	-0.76	-	-	-581300.00	-1.51	-	-	-350139.61	-1.81	-849610.00	-2.20
n	-	4	-	2	-	2	-	4	-	4	-	6	-	2	-	4

Figure F.1: The calculations of the half cell reactions of key compounds from literature Gibbs energy values [28].

Appendix G

Optical Basicity Theoretical Background

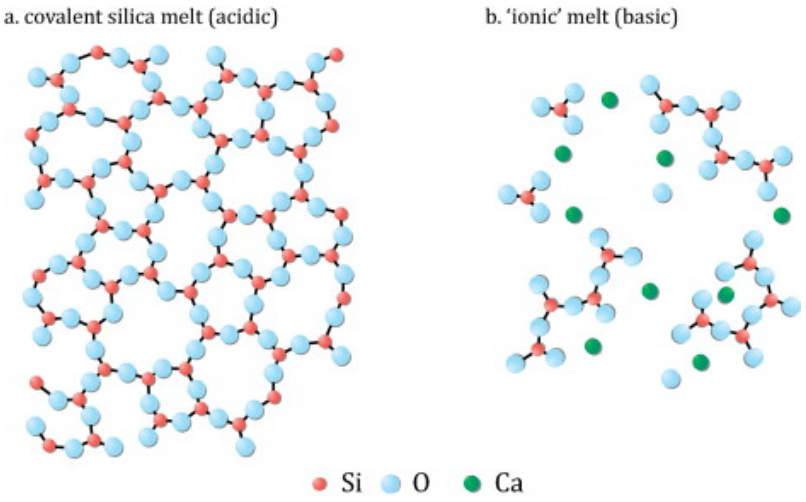

Figure G.1: Graphical representation of an acidic and basic metal oxide melt [43].

It has been proposed that molten oxide systems can be described in a similar manner to the Lewis model for acidity/basicity [90]. Basicity in this context can be described as the average negative charge borne by the oxygen atoms in an oxide-containing

system [90]. Theoretically, the optical basicity values are obtained by examining the ultra-violet 6s and 6p absorption band. The separation between the two bands is related to the positive charge of the metal ion. Ultimately, this produces an optical basicity value which is relative to CaO, which has a value of 1.0 and is considered to be a highly basic material. Table G.1 shows the optical basicity values for key oxides. The optical basicity of a composite material can be calculated as shown in equation G.1. Where X_A is the equivalent mole fraction of the cations present; and Λ is the optical basicity of the compound. The optical basicity for NZS iron slag was calculated using equation G.1 and found to be 0.61. This indicates that the slag is relatively "acidic".

Table G.1: Optical basicity values for common metal oxide compounds [90].

Compound	Optical Basicity (Λ)
Na_2O	1.15
CaO	1.00
FeO	1.00
MgO	0.78
TiO_2	0.61
Al_2O_3	0.60
SiO_2	0.48
B_2O_3	0.42

$$\Lambda = \Lambda_A X_A + \Lambda_B X_B \tag{G.1}$$

Optical basicity can be used as a comment on the level of polymerisation. "Acidic" samples have higher levels of network formers such as SiO_2, and therefore the sample is more structured. Likewise a "basic" sample has higher proportions of network breakers, such as CaO, and are more segmented. Optical basicity has been shown to be linked to physical properties such as viscosity and density, as shown in Figure G.2. There are empirical relations between optical basicity, viscosity [91] and density [92] for certain molten oxide systems. The optical basicity of the electrolyte can be used to

evaluate the compatibility of the electrolyte with the electrode and crucible material. As previously mentioned, research [37] has shown significant levels of corrosion of an iridium electrode in a basic solution but was deemed suitable in acidic conditions.

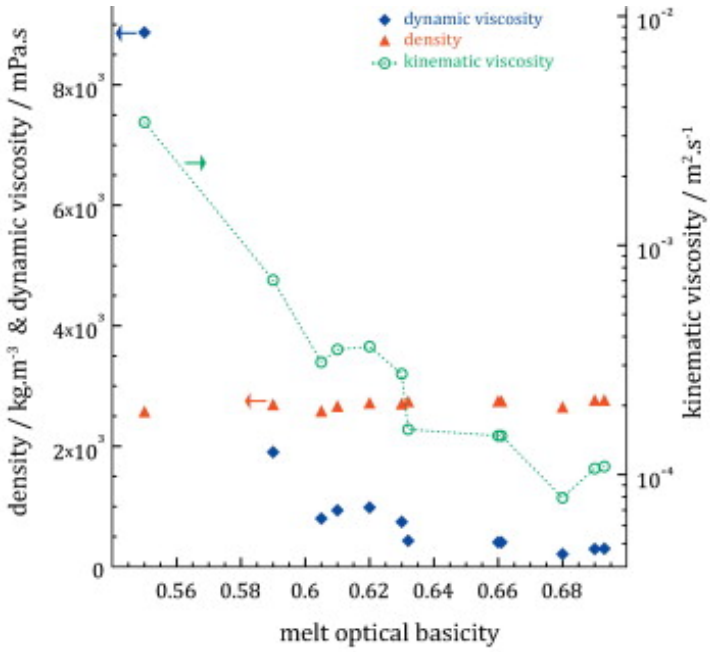

Figure G.2: The effects of optical basicity on the physical properties of a SiO_2-Al_2O_3-MgO-CaO melt [43].

Appendix H

SEM Line Graphs

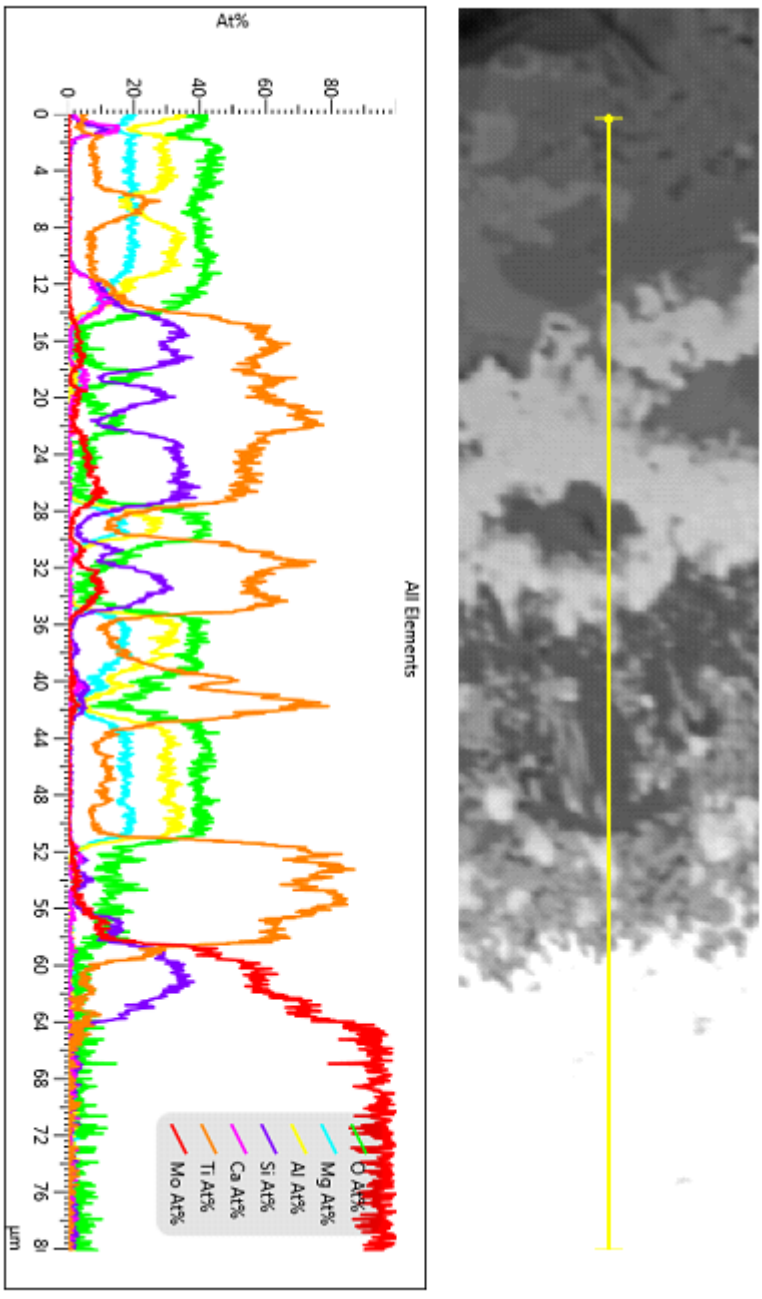

Figure H.1: A line scan across the cathode/slag interface, as shown in Figure 5.6, showing the elemental composition of the layered material on the molybdenum cathode.

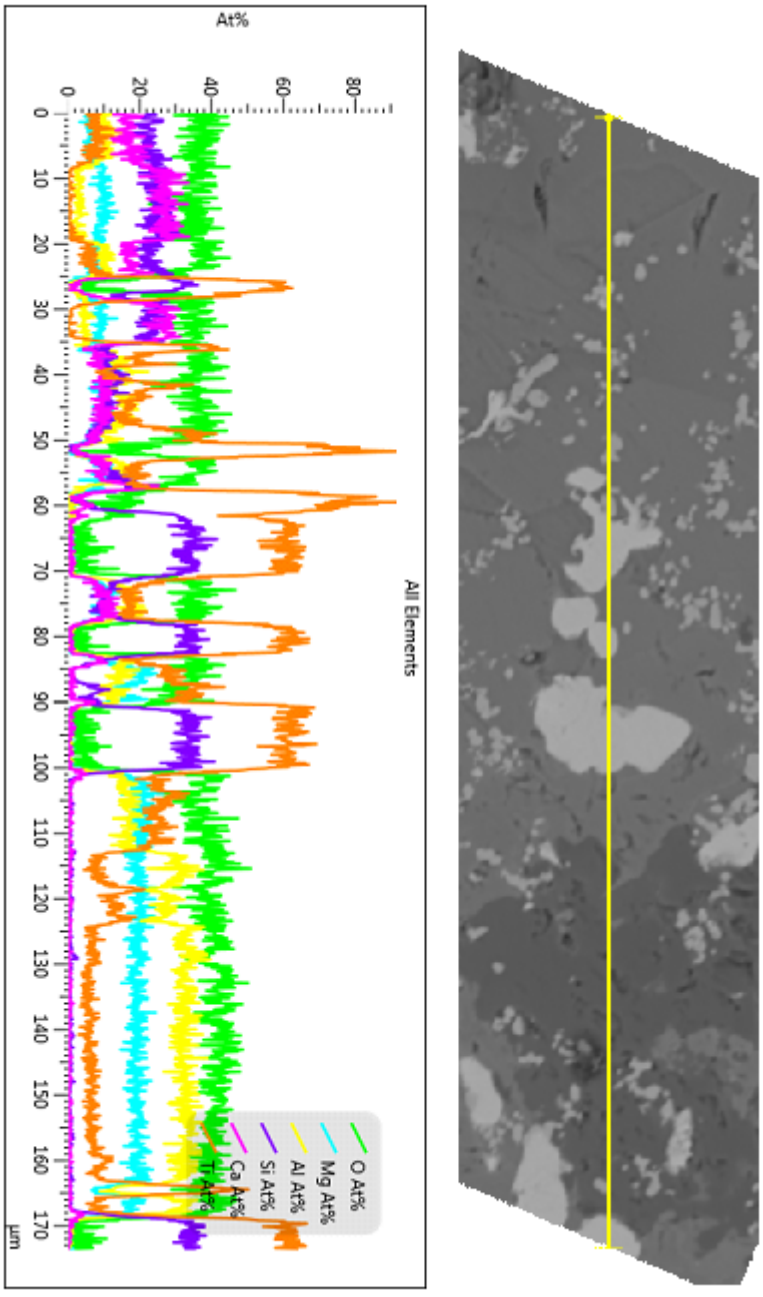

Figure H.2: A line scan across the pocket material, as shown in Figure 5.8, showing the elemental composition of the pocket material and the slag immediately surrounding it.

Appendix I

Key Engineering Drawings

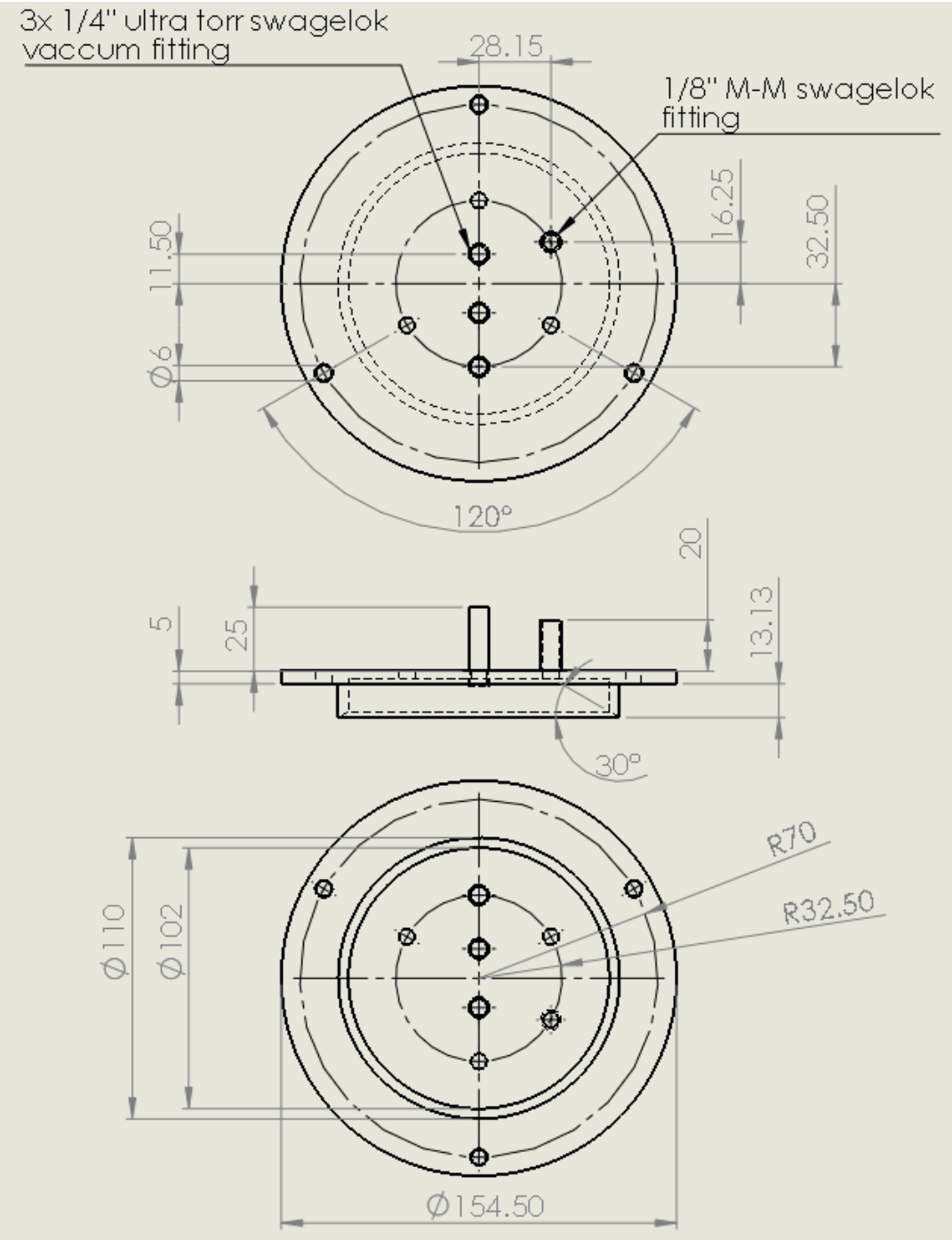

Figure I.1: Dimensioned drawing of the modified top flange.

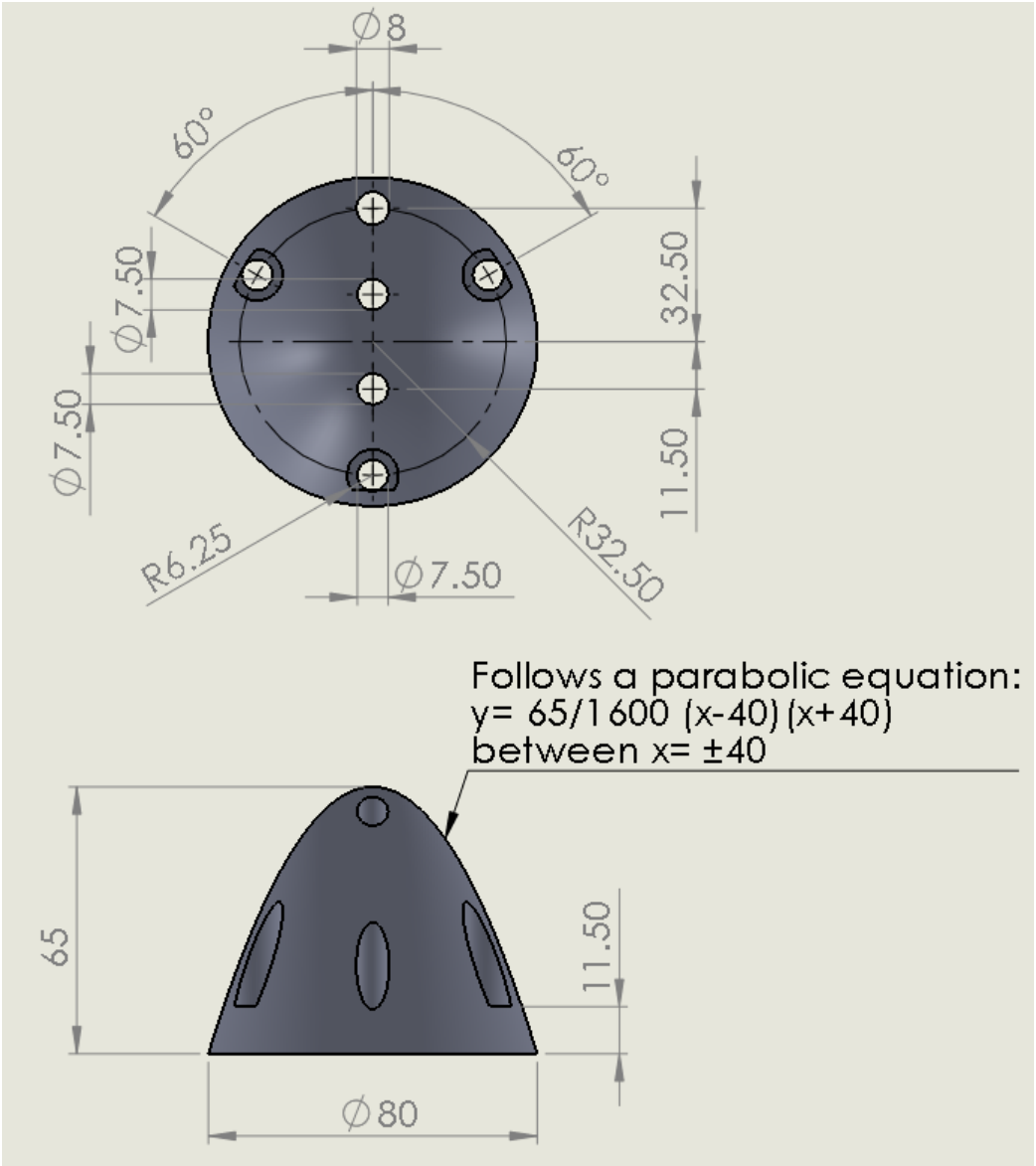

Figure I.2: Dimensioned drawing of the top parabolic radiation shield.

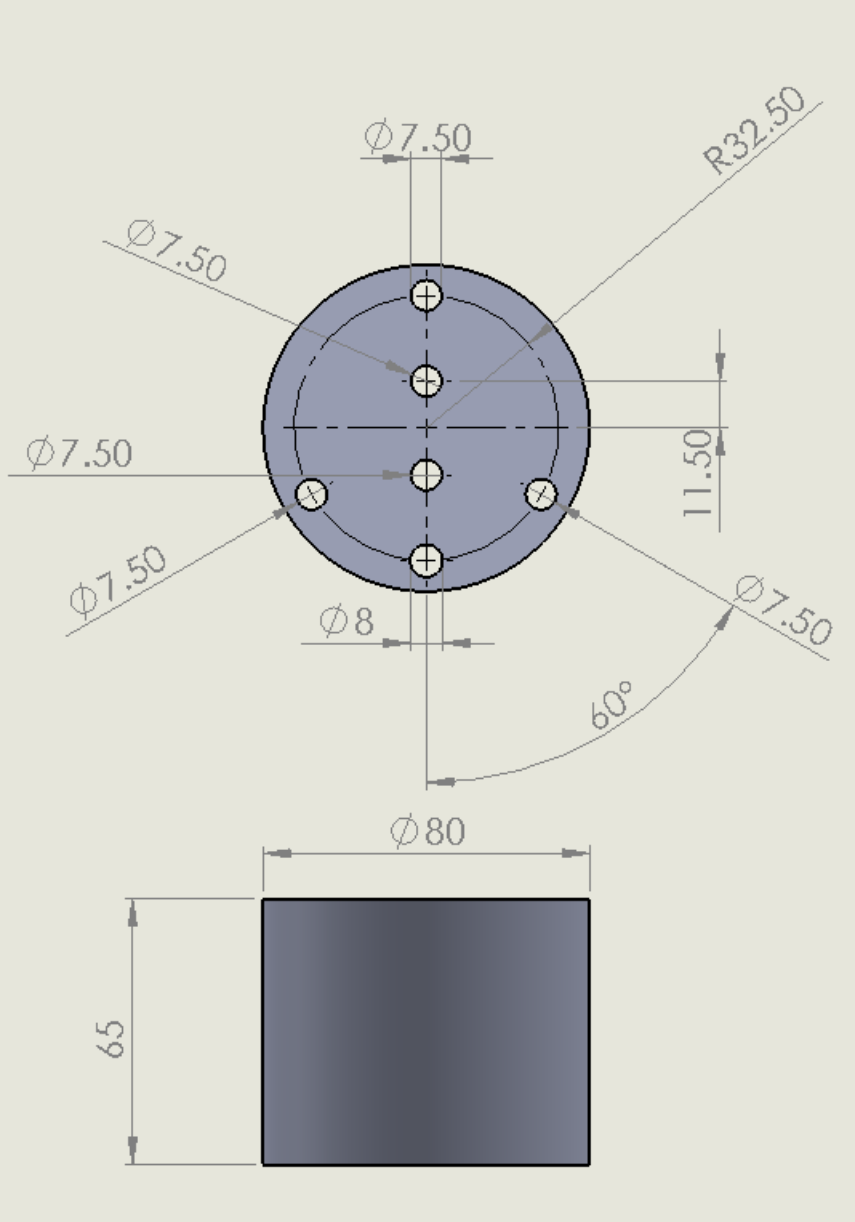

Figure I.3: Dimensioned drawing of the top cylindrical radiation shield.

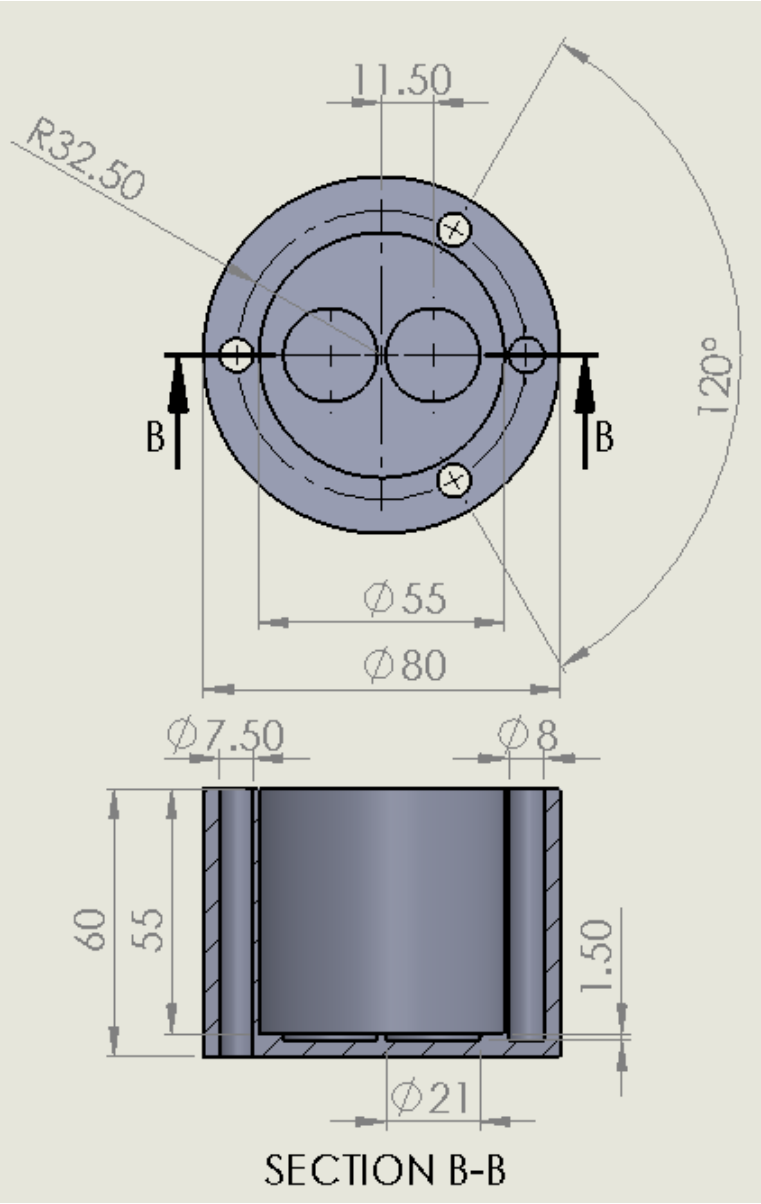

Figure I.4: Dimensioned drawing of the secondary container to house two 20 mm OD crucibles.

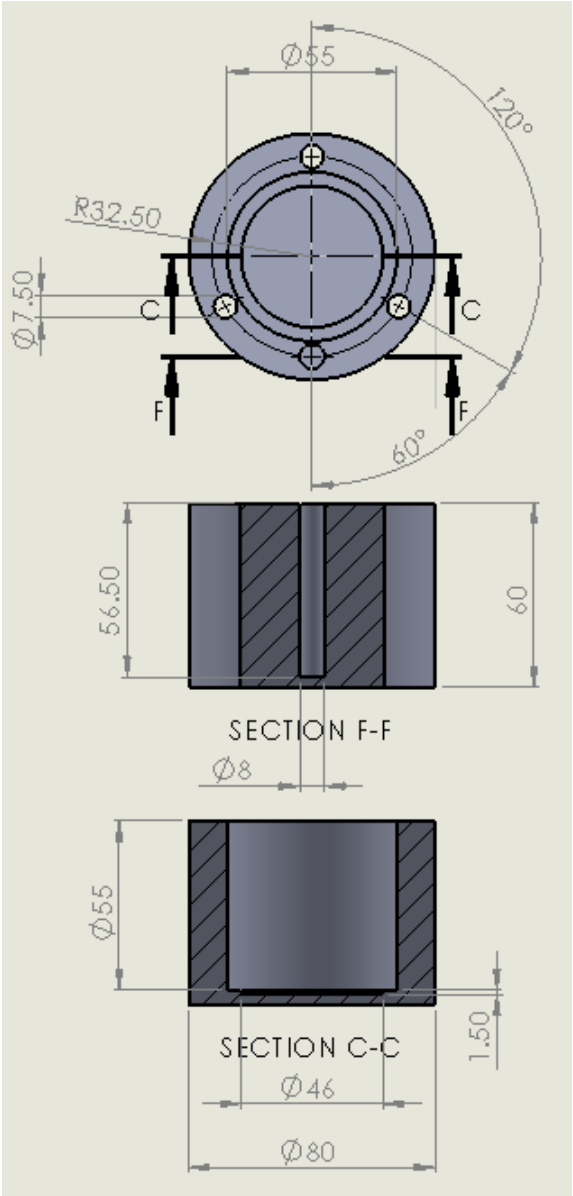

Figure I.5: Dimensioned drawing of the secondary container to house a single 45 mm OD crucible.

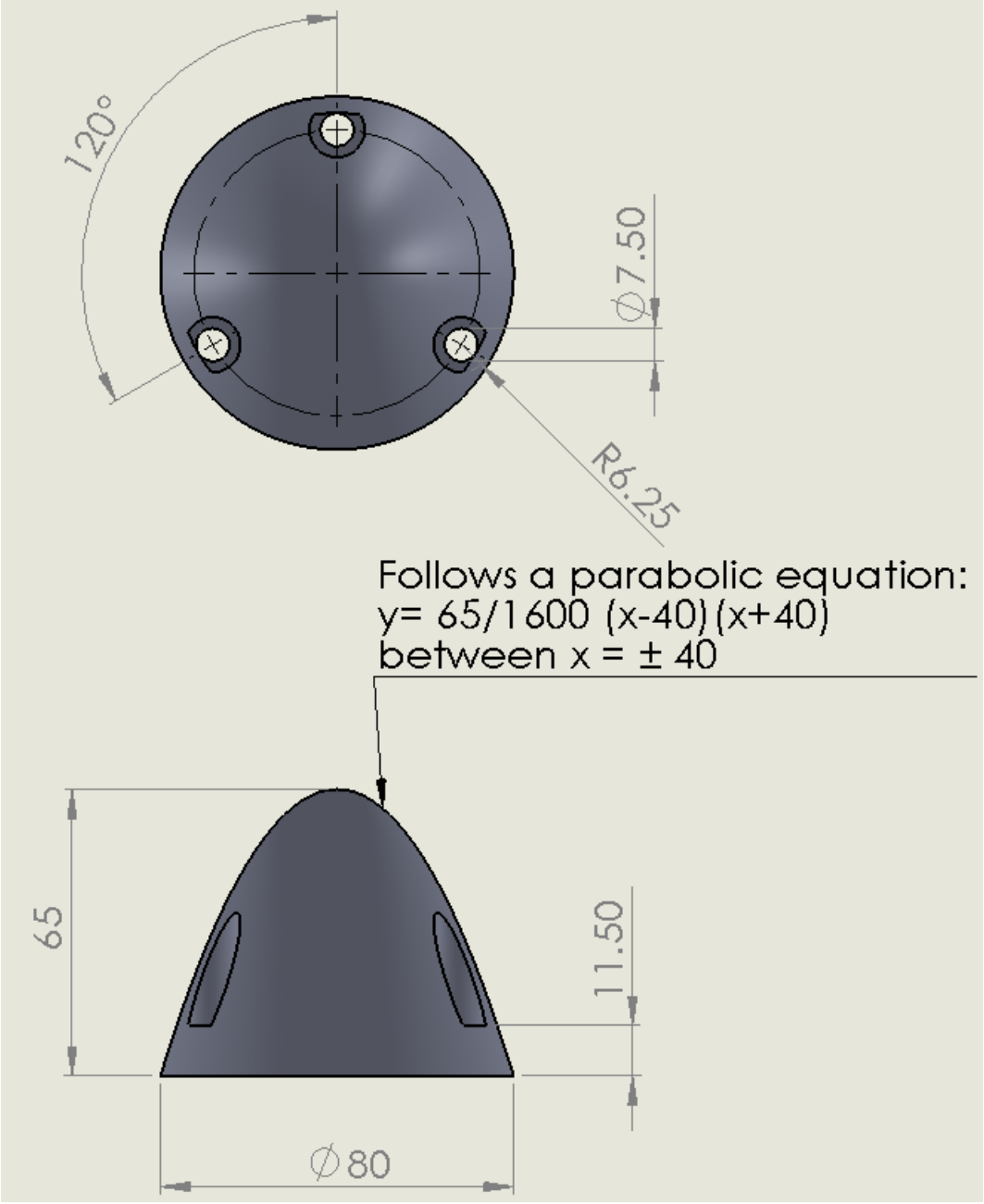

Figure I.6: Dimensioned drawing of the bottom parabolic radiation shield.

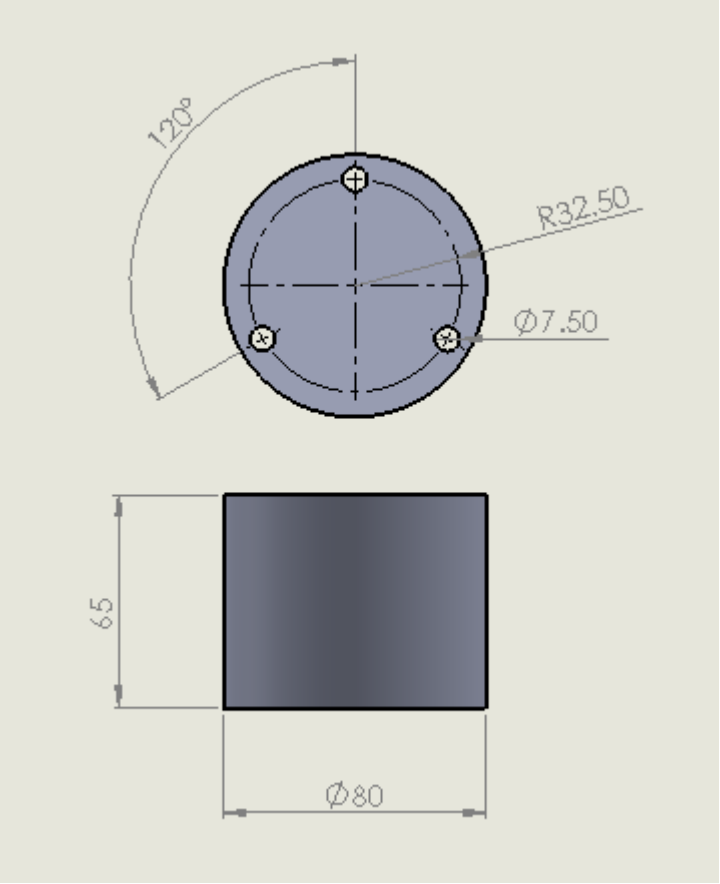

Figure I.7: Dimensioned drawing of the bottom cylindrical radiation shield.